CHARACTERIZING THE PRODUCTIVE LIMIT OF THE NORTHEAST PENNSYLVANIA MARCELLUS DRY GAS WINDOW: AN INVESTIGATION OF LOW RESISTIVITY ALONG THE LINE OF DEATH

A Thesis

by

NOAH MITCHELL MILLER

Submitted to the Office of Graduate and Professional Studies of
Texas A&M University
in partial fulfillment of the requirements for the degree of

MASTER OF SCIENCE

Chair of Committee,	Yuefeng Sun
Committee Members,	Julia Reece
	Berna Hascakir
Head of Department,	Michael Pope

December 2017

Major Subject: Geology

ABSTRACT

The Marcellus Shale is the single largest U.S. natural gas resource, both currently and for the foreseeable future. Whereas the Northeast Pennsylvania Marcellus Dry Gas Window produces a significant portion of total Marcellus production, it is burdened by a phenomenon known as the “Line of Death” (LOD), a coined term referring to an undefined line of demarcation that forms the southernmost limit of commercial production in the NE PA Dry Gas Window. The noncommercial wells to the south of the LOD have XRD values, TOC wt%, Ro%, and mineral composition comparable to commercial wells north of the LOD. However, for reasons not understood, noncommercial wells to the south of the LOD are characterized by very low resistivity values and lower total porosity values.

The hypothesis of this study is that the resistivity patterns and production trends observed in the NE PA Dry Gas Window suggest that some type of progressive, yet subtle, organic material (“OM”) transition at the nano-scale has occurred south of the LOD. This study characterizes portions of the NE PA Dry Gas Window on both sides of the LOD using 1) conventional electric logs and core analysis to prove bulk density similarity, 2) S/TEM, EDS and Raman Spectroscopy techniques to investigate the sources of conductivity in the OM, and 3) Large-scale, high-resolution SEM imaging and nitrogen adsorption to evaluate OM hosted pore size distributions and measure capacity to hold gas.

Regarding the low resistivity to the south of the LOD, the STEM and EDS discovered silver dispersed throughout the OM in both porous and non-porous samples

south of the LOD, while the OM Raman spectra provided evidence of increased carbon ordering (below graphite grade) south of the LOD. Regarding porosity, the large-scale SEM image segmentation and the nitrogen adsorption confirms that there is a quantifiable difference in the micro and meso pore size distributions between the north and south sides of the LOD, with samples south of LOD having significantly less pore area in the 1-2nm pore range. This study contends that the porosity deficiencies noted south of the LOD are linked to its increased carbon ordering.

ACKNOWLEDGEMENTS

I would like to thank all involved from Cabot Oil & Gas, Weatherford Laboratories, and Premier Oilfield Laboratories for making the last two years exciting and memorable. I must especially acknowledge Buddy Wylie (the Northeast Exploration Manager at Cabot Oil & Gas) whose incessant questions provided me the opportunity and the motivation to undertake and complete this thesis.

Special thanks are also due to Kultaransingh (Bobby) Hooghan (Lead SEM Technician at Weatherford Laboratories in Houston) who spent countless hours in his mad science station helping me plan, build and execute an operational workflow that produced the high quality, industry grade SEM images presented in this thesis. I would also like to thank Elizabeth Krukowski (Geoscientist at Premier Oilfield Laboratories) who hosted me for a week and helped acquire quality Raman and N_2 absorption data for this research.

Finally, I must recognize my beautiful wife Chelsea for all her support while I have been immersed in this project.

CONTRIBUTORS AND FUNDING SOURCES

Contributors

This work was supervised by a thesis committee consisting of my geology advisor, Dr. Yuefeng Sun, Dr. Julia Reece of the Department of Geology and Geophysics, and Dr. Berna Hascakir of the Department of Petroleum Engineering.

The raw well log and core data were supplied by Cabot Oil & Gas Corporation, Encana Corporation, and Chesapeake Energy Corporation. The SEM/STEM images and EDS spectra were facilitated by Kultaransingh (Bobby) Hooghan of Weatherford Laboratories, while the Raman and N_2 adsorption data were facilitated by Elizabeth Truskowski of Premier Oilfield Laboratories.

All other work conducted for the thesis was completed by the student independently.

Funding Sources

All third-party processing costs were paid by Cabot Oil & Gas.

NOMENCLATURE

BSE	Back Scattered Electrons
EIA	Energy Information Administration
FIB	Focused Ion Beams
He	Helium
LOD	Line of Death
LMARC	Lower Marcellus
NE PA	Northeast Pennsylvania
N_2	Nitrogen
OM	Organic Matter
PA	Pennsylvania
PCL	Purcell Limestone
PSD	Pore Size Distribution
Ro%	Vitrinite Reflectance
SE	Secondary Electrons
SEM	Scanning Electron Microscopy
SRP	Shale Rock Properties
S/TEM	Scanning/Transmission Electron Microscopy
TOC	Total Organic Content
USPR_Lm	Union Springs Lime
USPR	Union Springs

USPR_U	Union Springs Upper
USPR_L	Union Springs Lower
UMARC	Upper Marcellus
Vol%	Volume Percent
Wt%	Weight Percent
XRD	X-Ray Diffraction
FWHM	Full Width Half Max

TABLE OF CONTENTS

Page

ABSTRACT ii

ACKNOWLEDGMENTS iv

CONTRIBUTORS AND FUNDING SOURCES v

NOMENCLATURE vi

LIST OF FIGURES x

LIST OF TABLES xiii

1. INTRODUCTION 1
    1.1 Introduction 1
        1.1.1 Statement of Problem 2
    1.2 Importance 3
        1.2.1 Marcellus Production and Extent 5
    1.3 Literature Review 7
        1.3.1 The Line of Death 7
        1.3.2 Past Research 8
            1.3.2.1 Ethan Shula Work 9
            1.3.2.2 Weatherford Laboratories Work 11
        1.3.3 Geologic Background and Stratigraphy 12
    1.4 Hypothesis 16
    1.5 Research Objectives 18

2. METHODS 19
    2.1 Well and Sample Coverage 19
    2.2 Mudrock Composition 20
    2.3 Resistivity Assessment 21
        2.3.1 S/TEM 23
        2.3.2 EDS 25
        2.3.3 Raman Spectroscopy 29
    2.4 Reservoir Quality Assessment 37
        2.4.1 SEM 37
        2.4.2 N_2 Adsorption 45

3. RESULTS 50
    3.1 Mudrock Composition Comparison 50

3.2 Electrical Log Comparison 54
3.3 Resistivity Assessment 58
3.3.1 S/TEM EDS 58
3.3.1.1 Buda Porous OM and Non-Porous OM 58
3.3.1.2 Teel Porous OM and Non-Porous OM 62
3.3.2 Raman Spectroscopy 66
3.4 Reservoir Quality Assessment 75
3.4.1 Average SEM OM and Pore Segmentation Data 75
3.4.2 Local OM Hosted Pore Segmentation 77
3.4.2.1 Lower Marcellus 77
3.4.2.2 Union Springs 79
3.4.3 Global Pore Segmentation 80
3.4.3.1 Lower Marcellus 80
3.4.3.2 Union Springs 82
3.4.4 N_2 Adsorption 83
3.4.4.1 Lower Marcellus 83
3.4.4.2 Union Springs 85

4. DISCUSSION 87
4.1 Resistivity Assessment 87
4.1.1 Silver Discovery 87
4.1.2 Carbon Ordering Evidence 90
4.2 Reservoir Quality Assessment 91
4.3 Ramifications of This Study to Future Research 92
4.4 Ramifications of This Study to Operators in the NE PA Dry Gas Window 94

5. CONCLUSIONS 97
5.1 Conclusions 97

REFERENCE LIST 100

LIST OF FIGURES

Page

Figure 1: U.S. Dry Natural Gas Production by Source -1990 through 2040 4

Figure 2: U.S. Shale Natural Gas Production by Play - 2007 through 2017..... 4

Figure 3: Map of Pennsylvania Well Pads and Cumulative Production by County 6

Figure 4: The Shula Work..... 10

Figure 5: The Weatherford Laboratories Work..... 12

Figure 6: Idealized Stratigraphic Column for the Marcellus Shale..... 14

Figure 7: Marcellus Shale Deposition Model 16

Figure 8: A Typical NE PA Well Log South of the LOD..... 17

Figure 9: Map of This Study's Area of Interest Marked for Well Dataset 19

Figure 10: Petrophysical/Composition Rock Model for Organic Rich Mudrocks..... 22

Figure 11: Illustration of S/TEM Sample Preparations..... 25

Figure 12: Elements resolvable through interaction with L-line and K-line emissions... 27

Figure 13: Illustration of SEM EDS Output..... 28

Figure 14: Illustration of Carbonaceous Raman Spectra..... 30

Figure 15: Progressive Ordering of OM at Varying Temperatures 33

Figure 16: Summary of the Kouketsu Deconvolution Method..... 35

Figure 17: Picture of HORIBA LabRAM HR Raman Microscope 36

Figure 18: SEM Signal Comparison 39

Figure 19: SEM Image Voltage Comparison..... 40

Figure 20: Examples of This Study's SEM Imaging 42

Figure 21: This Study's SEM Segmentation Workflow 44

Figure 22: Images from Global Pore Segmentation 45

Figure 23: N_2 Absorption Apparatus and Output Example 46

Figure 24: Summary of N_2 Adsorption Process 47

Figure 25: Dataset Composition Comparison 51

Figure 26: Dataset TOC/Porosity Relationships 54

Figure 27: Dataset Log Curves 55

Figure 28: Dataset Log Attributes 57

Figure 29: STEM Cross Sectional View of Buda Porous OM at Multiple Magnification 58

Figure 30: STEM EDS Map of Buda Porous OM 59

Figure 31: STEM Buda Non-Porous OM at Different Magnifications 60

Figure 32: STEM EDS Map of Buda Non-Porous OM 61

Figure 33: STEM Cross Sectional View of Teel Porous OM at Different Magnification 62

Figure 34: STEM EDS Map of Teel Porous OM 63

Figure 35: STEM Cross Sectional View of Teel Non-Porous OM 64

Figure 36: STEM EDS Map of Teel Non-Porous OM 65

Figure 37: Raw Raman Spectra for Teel and Buda 66

Figure 38: Beyssac Deconvolution for Samples in the LMARC and USPR 68

Figure 39: Lahfid Deconvolution for Samples in the LMARC and USPR 69

Figure 40: Summary of the Kouketsu Deconvolution Method 72

Figure 41: Kouketsu Deconvolution for Samples in the LMARC and USPR 73

Figure 42: Large OM Porosity SEM Images of LMARC and USPR Mosaics 77

Figure 43: Porosity Distributions and Cumulative Pore Area for Samples in the LMARC 78

Figure 44: Porosity Distributions and Cumulative Pore Area for Samples in the USPR 80

Figure 45: Averaged Global Pore Segmentation Data for Samples in the LMARC 81

Figure 46: Averaged Global Pore Segmentation Data for Samples in the USPR 82

Figure 47: N_2 Adsorption Pore Surface Area and Volume for Samples in the LMARC 84

Figure 48: N_2 Adsorption Pore Surface Area and Volume for Samples in the USPR_U 85

Figure 49: N_2 Adsorption Pore Surface Area and Volume for Samples in the USPR_L 86

Figure 50: Buda Pore Area Comparison 94

LIST OF TABLES

Page

Table 1: Cumulative Production from the Counties Comprising the Area of Interest 7

Table 2: Dataset Description 20

Table 3: Dataset Average He Porosity% and TOC Vol% by Member 52

Table 4: Beyssac Deconvolution Ratios for Samples in the LMARC and USPR 69

Table 5: Lahfid Deconvolution Ratios for Samples in the LMARC and USPR 70

Table 6: Kouketsu Deconvolution Values for Samples in the LMARC and USPR 73

Table 7: Comparison of TOC Vol% to Average Mosaicked SEM TOC% 76

Table 8: Comparison of He Porosity % to SEM Derived Porosity Values 76

1. INTRODUCTION

1.1 Introduction

Since the inception of production from the Marcellus Shale in 2008 through the end of the 1st quarter of 2017, 20.69 Tcf of natural gas has been produced in Pennsylvania (Pennsylvania Department of Reporting Services, March 2017). Correspondingly, Pennsylvania became the second largest natural gas producing state in the U.S. starting in 2013 (EIA, 2016). The large majority (66%) of this Pennsylvania production comes from six counties in the northeast corner of the state (Pennsylvania Department of Reporting Services, March 2017). Development of the Marcellus Shale in Northeast Pennsylvania (NE PA) is handicapped by an unexplained phenomenon referred to as the "Line of Death" (LOD), which is a vaguely defined line of demarcation within the official boundaries of the NE PA Marcellus Shale that represents the southernmost limit of commercial production. The noncommercial wells to the south of the LOD have x-ray diffraction (XRD) values, total organic carbon weight percentage (TOC wt%), vitrinite reflectance (Ro%), and mineral composition comparable to commercial wells north of the LOD. However, for reasons not yet understood, the noncommercial wells drilled to the south of the LOD are characterized by very low resistivity values (i.e. deep resistivity log curve responses as low as 0.08 Ohmms compared to ranges of 50 to 150 Ohmms typically found in wells north of the LOD) and lower total porosity values (i.e. core helium porosity values of ~5% south of the LOD and ~7% north of LOD).

It was originally theorized that acreage south of the LOD is noncommercial because it was "overcooked", which caused the organic material to become graphite. This

theory was later abandoned because graphite or crystalline proto-graphite material has never been found by conventional XRD investigation. A new hypothesis about the lack of commercial production on the south side of the LOD examines if the patterns and trends observed in resistivity suggest that some type of subtle, yet progressive, atomic or molecular scale structural change may have occurred within the organic matrix at, and to the south of, the observed LOD. This new theory stems from work done by Walters (2014) regarding the possible effects of turbostratic carbon nanostructures on electrical conductivity in shales, and Beyssac (2002b) regarding the effect of carbon ordering on nanometer scale organic porosity. Their combined work suggests nanometer structural ordering of the organic matter (OM) could be responsible for the conductivity and the loss of nanometer size OM porosity observed south of the LOD. This study characterizes portions of the Marcellus Shale in NE PA on both sides of the LOD using 1) conventional electric logs and core analysis to prove bulk density similarity, 2) Transmission Electron Microscopy (TEM), Scanning Transmission Electron Microscopy (S/TEM), Energy Dispersive Spectroscopy (EDS) and Raman Spectroscopy techniques to investigate the sources of conductivity in the OM, and 3) Large-scale, high-resolution Scanning Electron Microscopy (SEM) imaging and low pressure nitrogen (N_2) adsorption to evaluate OM hosted pore size distributions and to measure the rock's capacity to hold gas.

1.1.1 Statement of Problem

Previous inquiries have failed to explain why extremely low resistivity values exist on the south side of the LOD in NE PA, or establish a comprehensible correlation between the low resistivity and noncommercial outcomes. As demonstrated by the wells in this

study's dataset, drilling activity in areas with proximity to the estimated location of the LOD have been measurably less successful than drilling activity north of the LOD. Whereas the Marcellus Shale is considered a "known" resource, and commercially is considered a "development play", drilling on acreage approaching the LOD effectively is characterized by a risk profile more akin to exploration than development. Accordingly, the lack of an operational theory to explain the cause of the LOD, along with a precise understanding of the LOD's location creates an operational risk premium that impedes the optimal development of the NE PA Marcellus Shale.

1.2 Importance

Natural gas production in the U.S. is increasingly dominated by shale and tight oil plays (EIA, 2016) (Figure 1). The Marcellus Shale is the largest natural gas producing shale play in the U.S. based upon both current production (19,967 Mmcf/day as of September 2017) (Figure 2) and estimated future production (proved reserves of 72.7 Tcf of natural gas as of December 2015) (EIA, 2016). Nano-scale characterization has become an important tool to help industry participants evaluate unconventional resources. Further study of the Marcellus Shale's reservoir characteristics in relation to resistivity and OM porosity on both sides of the LOD at the nano-scale could yield results that would help industry participants rationalize the capital spending required to develop acreage with proximity to the LOD.

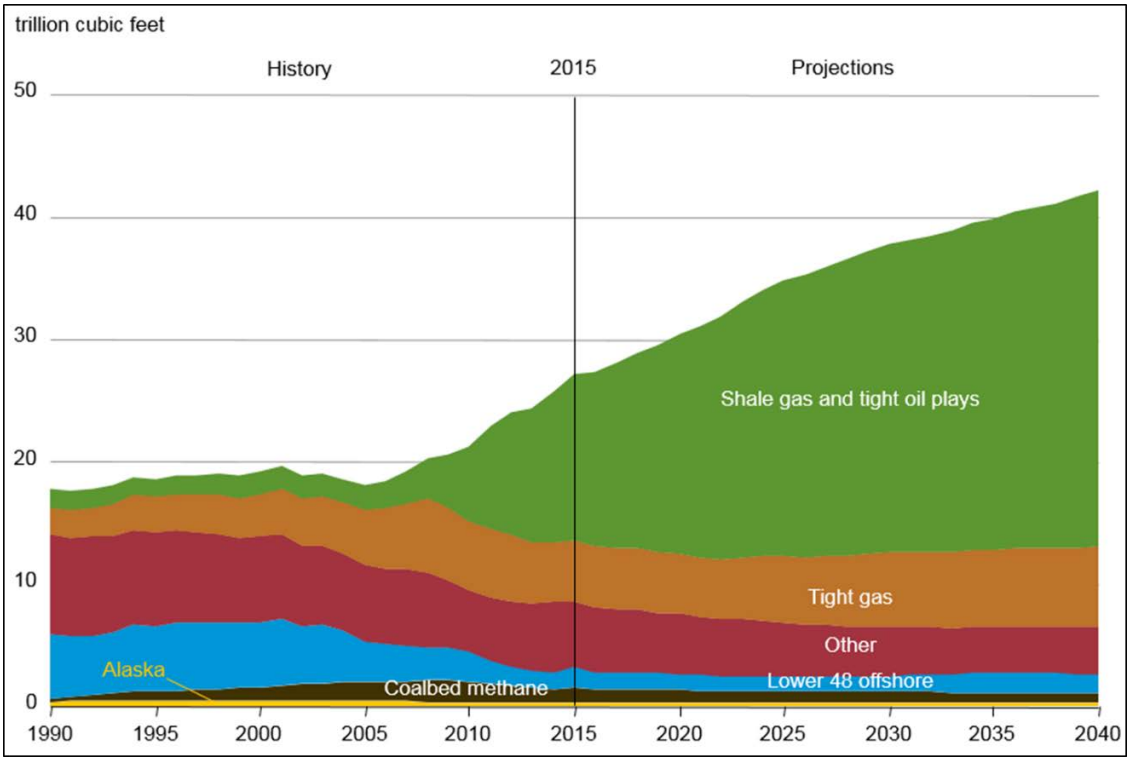

Figure 1: U.S. Dry Natural Gas Production by Source -1990 through 2040 (EIA, 2016).

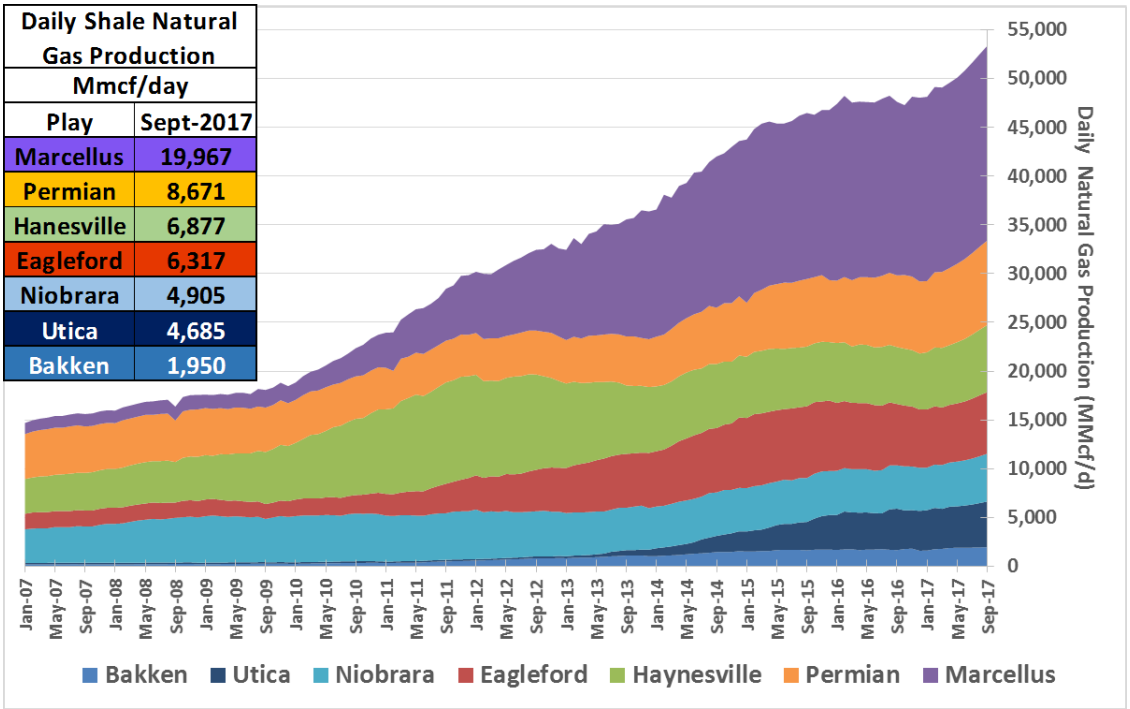

Figure 2: U.S. Shale Natural Gas Production by Play – 2007 through 2017. The graph and table illustrate the size of the Marcellus Shale vis-à-vis the other major U.S. shale plays (EIA, 2017).

1.2.1 Marcellus Production and Extent

According to the USGS assessment (USGS, 2011) the Marcellus Shale contains about 84 Tcf of undiscovered, technically recoverable natural gas and 3.4 billion barrels of undiscovered, technically recoverable natural gas liquids. Undiscovered, technically recoverable resources are those that are estimated to exist based on geologic knowledge and theory that can be produced using currently available technology and industry practices. USGS's Marcellus Shale assessment includes areas in Kentucky, Maryland, New York, Ohio, Pennsylvania, Tennessee, Virginia, and West Virginia (USGS, 2011), whereas EIA's estimates of proved reserves in the Marcellus Play of 72.7 Tcf at the end of 2015 only includes Pennsylvania and West Virginia (EIA, 2016). The EIA's definition of proved reserves are estimated volumes of hydrocarbon resources that analysis of geologic and engineering data demonstrates with reasonable certainty are recoverable under existing economic and operating conditions.

The state of Pennsylvania has been the second largest natural gas producing state in the U.S. since 2013, due primarily to the Marcellus Shale (EIA, 2016). As shown in Figure 3, production from the Marcellus Shale in Pennsylvania is mainly concentrated in the southwest and northeast portions of the state, with the southwest portion producing primarily wet gas (the "wet gas window") while the northeast portion producing primarily dry gas (the "dry gas window").

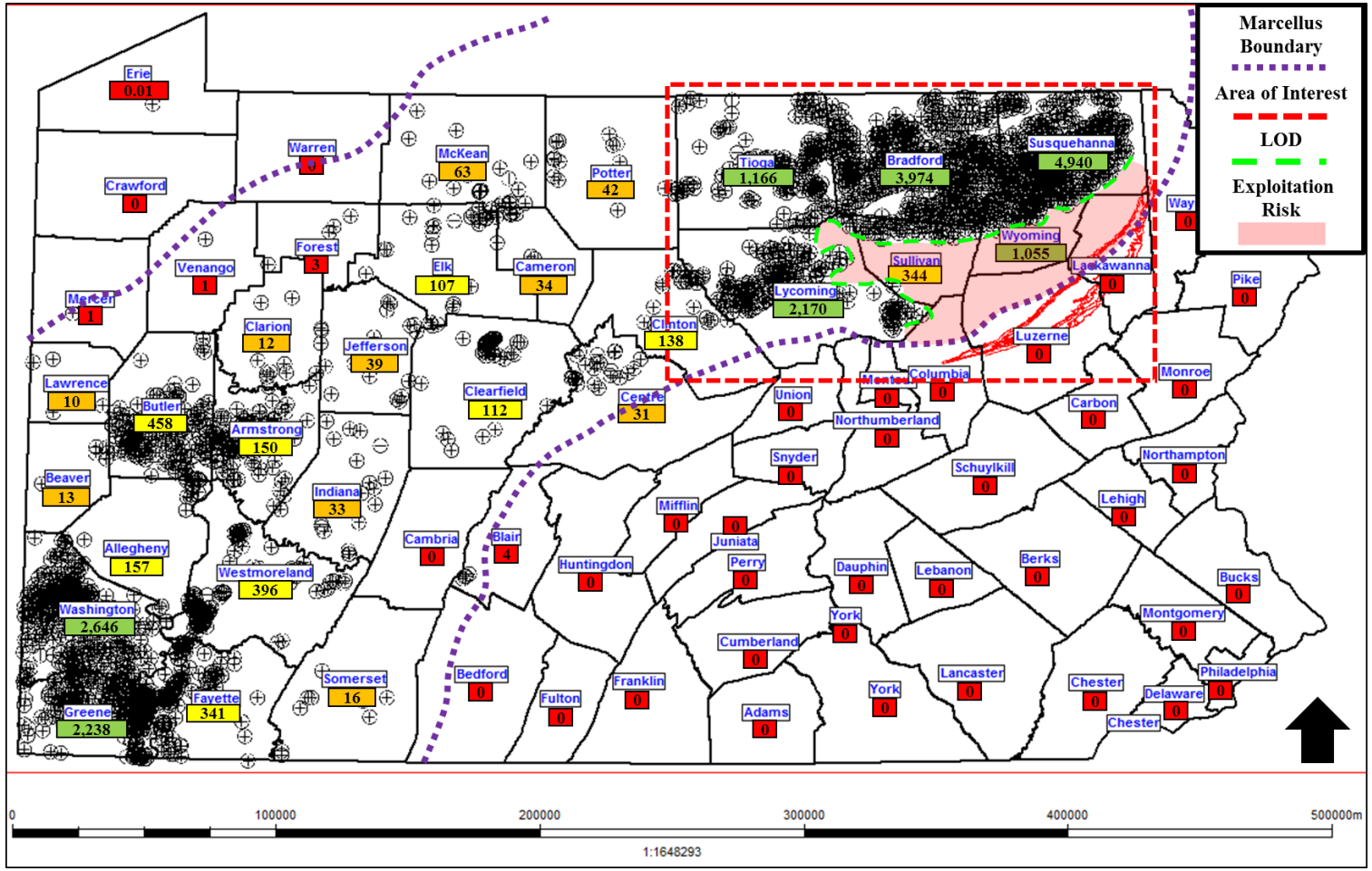

Figure 3: Map of Pennsylvania Well Pads and Cumulative Production by County. The black circles represent productive well pads, while the numbered boxes within each county represent cumulative production (inception to date) of natural gas in BCF (Data taken from PA Department of Reporting Services). The colors of these boxes denote the degree of productivity with green being the highest and red being the lowest. The purple dotted line represents the Marcellus Shale boundary as determined by the formation in the subsurface taken from EIA (2017) structure figure. The red dashed box represents the area of interest for this study. The large green dashed line is the generalized location of the LOD in NE PA. The elongated red feature south of the Marcellus Shale boundary is the Lackawanna Synclinorium.

Of the 20.69 Tcf of cumulative Pennsylvania Marcellus Shale production depicted in Figure 3, 66% has been produced from the six counties within the dry gas window listed in Table 1. The area of interest of this study is NE PA Marcellus dry gas window which is comprised primarily of these six counties.

County	Cumulative Gas Production (BCF)	Percentage of Total PA Cumulative Production
Susquhanna	4,940	24%
Bradford	3,974	19%
Lycoming	2,170	10%
Tioga	1,166	6%
Wyoming	1,055	5%
Sullivan	344	2%
Cumlative	**13,648**	**66%**

Table 1: Cumulative Production from the Counties Comprising the Area of Interest. Taken, or derived, from the PA Department of Reporting Services.

Before going further, it is best to elaborate about the nature of the LOD and its history, and review the stratigraphic nomenclature for the Marcellus Shale that will be used in this study.

1.3 Literature Review

1.3.1 The Line of Death

Based on our current understanding, the LOD is not a known stratigraphic attribute, nor is its location defined by precise surveying. Instead, the term 'Line of Death' is a nontechnical commercial catch phrase used by industry participants in the dry gas window of NE PA to efficiently articulate a technical anomaly. As seen in Figure 3, the general location of the LOD can be envisioned by plotting productive well spots. While

all producing areas have boundaries, usually the boundaries are defined by explainable variations in reservoir attributes. The conundrum in the dry gas window of NE PA is that the attributes of the rock south of the LOD are very comparable with the commercially productive rock to the north of the LOD, with the only large differences being the resistivity and the porosity measurements.

The oldest, and most common hypothesis to explain the LOD focuses on the NE PA's heightened thermal maturity, as correlated with the Lackawanna Synclinorium. As shown in Figure 3, the Lackawanna Synclinorium is a 63-mile-long anthracite basin located in portions of Columbia, Luzerne, Lackawanna, Wayne, and Susquehanna counties (Harrison, 2004). The theory related to this anthracite basin argues that natural gas development is threatened by the high thermal conditions necessary for the Lackawanna Synclinorium's development, and the corresponding degradation of the surrounding strata. Generally, anthracite is the highest rated coal with over 87% carbon content and is associated with increased metamorphism (Harrison, 2004). It is worth mentioning that when the thermal maturity theory was widely accepted it was also believed that a maturity Ro% of ~2.5% was the ceiling for dry gas production. This belief has since been vacated because of significant production in Susquehanna and Wyoming counties that routinely has maturity Ro% values exceeding 3.00% (Repetski, 2008).

1.3.2 Past Research

A recent example of academic research focusing on thermal impacts in the Marcellus Shale was conducted by Ethan Shula at Cedarville University (Shula, 2014). Shula attempted to establish a causal relationship between thermal maturity and the LOD

via the discovery of clay diagenesis. A competing high maturity based hypothesis was developed by Weatherford Laboratories, which claimed that organic matter at the proto-graphite metamorphic grade (below zeolite facies) could explain noncommercial outcomes and low resistivity to the south of the LOD (Laughrey, 2011).

1.3.2.1 Ethan Shula Work

Shula (2014) focused on identifying the composition of the Marcellus along the LOD using XRD analysis. Shula, like many others, hypothesized that the area along the LOD is very thermally mature and therefore would exhibit evidence of smectite diagenesis within the Marcellus clays that would retard natural gas production. The Shula Work included wellbore cuttings supplied by Chief Oil & Gas (three productive wells Noble Unit 1H, Squier Unit B-2H, Harvey Unit 6H from the north side of the LOD, and one noncommercial well Jerauld Unit 1H from the south side of the LOD) spanning from southern Susquehanna County to northern Wyoming County (Figure 4).

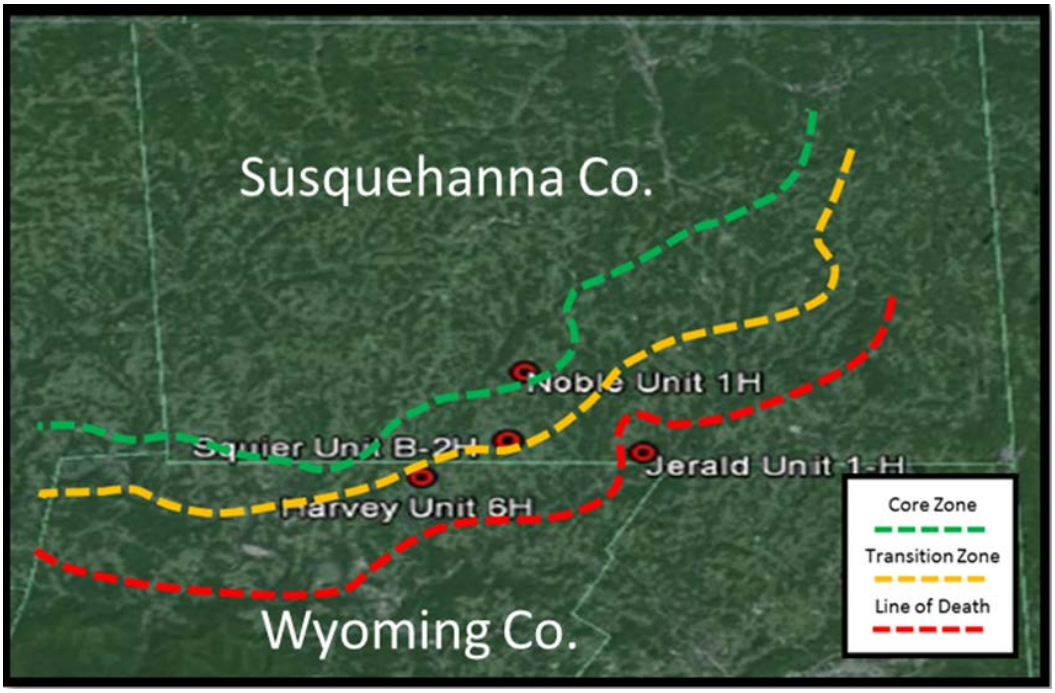

Figure 4: The Shula Work. This map illustrates Shula's well dataset and its estimated location of the LOD (Modified after Shula, 2014).

The idea of high thermal maturity destroying gas production in acreage approaching the LOD would be supported by the identification of significant quantities of layered illite/smectite that would drastically decrease rock brittleness, porosity and permeability (Jiang, 2012). The results of the Shula Work were unexpected as no distinguishable differences in the mineralogy were noted between the four wells. The Marcellus Shale minerology noted by Shula was characterized by quartz, plagioclase (albite), calcite, dolomite, pyrite, kaolinite, illite, chlorite, and insignificant/minor quantities of layered illite/smectite. The largest weight percentage and volume fraction of the samples were comprised of quartz and carbonate material (calcite/dolomite) and illite. The lack of smectite diagenesis within the Marcellus clays suggest that there must be another explanation for the existence of the LOD that is unrelated to clay diagenesis.

1.3.2.2 Weatherford Laboratories Work

Weatherford Laboratories' research focused on comparing low resistivity values from two unproductive wells (Salansky #1 and Bennett #1) on the south side of the LOD in NE PA to a productive well (Houser) in Clearfield county in central PA. The Weatherford team was looking for evidence of graphitization of organic pyrobitumen as a possible explanation for the low resistivity values. The XRD analyses of the Bennett #1 in Sullivan County and the Salansky #1 in Luzerne County were interpreted by a minority of the research team to represent graphite (Figure 5). However, others on the research team referred to the material as "graphic pyrobitumen" and interpreted the supposed graphite XRD peak as a continuum from asphalt through asphaltic pyrobitumen to graphitic pyrobitumen to graphite (Figure 5).

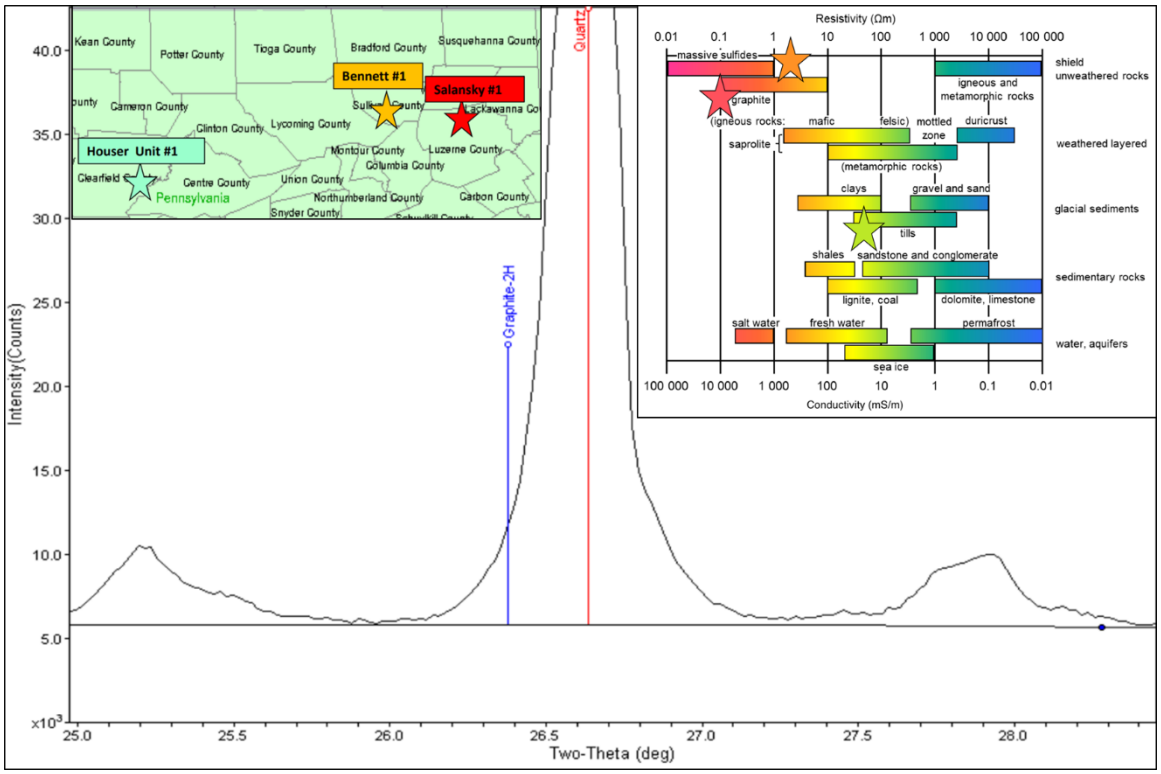

Figure 5: The Weatherford Laboratories Work. The upper left is a map showing the location of the wells in the dataset, while the upper right illustrates each well's average resistivity value (using corresponding star color from the upper right map). The large graph illustrates the XRD spectra peaks related to Bennett #1 that notes the questionable interpretation of graphite within the quartz peak (Laughrey, 2011).

If a true graphite peak had been discovered in the Bennett #1 and the Salansky #1, XRD analyses on cutting samples could be used to create a "graphite map" that would effectively identify the location of the LOD; not unlike how ash beds are mapped in other unconventional shale plays. Unfortunately, there has not been interpretable amounts of graphite documented from XRD analyses from wells in southern Susquehanna County and northern Wyoming County.

1.3.3 Geologic Background and Stratigraphy

The Appalachian Basin is a classic foreland basin that began its development with the initiation of the Taconic Orogeny around the time of the Early-Middle Ordovician

transition (~472 Ma) (Ettensohn, 2008). The Taconic Orogeny is responsible for the formation of the Taconic highlands that act as an eastern barrier for the maturing Appalachian Basin (Faill, 1997). By the Middle Devonian, the Acadian Orogeny, which followed the Taconic Orogeny, resulted in an oblique convergence along a strike-slip fault zone that once separated the Laurasian terrain from a microcontinent known as the Avalon Terrane (Williams and Hatcher, 1982). The sediments of the Middle Devonian Hamilton group of the Appalachian Basin are an eastward and southeastward thickening wedge of marine and non-marine shale, siltstone, and sandstone deposits described by Rast and Skehan (1993) as part of the Catskill Delta succession formed by the accumulation of eroded sediments from the uplifted and thrust-faulted margin of the elongated foreland basin that formed in the response to the Acadian Oblique collusion of the Avalonia microplate and Laurentia. (Ettensohn, 1985).

The Marcellus Shale is the basal unit of the Hamilton Group and consists primarily of two black shale intervals separated by thin limestone intervals, grey shale, and lesser sandstones of variable thickness (De Witt et al., 1993). James Hall (1839) was the first geologist who called the organic rich black and grey shale that outcropped near the town of Marcellus, Onondaga County New York the “Marcellus Shale”. The Marcellus Formation was initially subdivided into the Unions Springs Member and the overlying Oatka Creek Member by Cooper (1930). This elegant and simple nomenclate became muddled over the next 80 years until Lash and Engelder (1989) proposed a revised Marcellus stratigraphy that harkened back to the original identification.

This study will adopt the NE PA Marcellus Shale lithostratigraphy currently used by operators that is correlated to the NE PA outcrop, wireline logs and the New York Marcellus outcrop. This study will deviate from Lash and Engelder (2011) stratigraphy by designating the Oatka Creek Member as the Upper Marcellus Member (UMARC), the Cherry Valley Member as the Purcell Limestone Member (PCL), and the Union Springs Member will be subdivided from bottom to top as the Union Springs Lime Member (USPR_Lm), Union Springs Member (USPR), and Lower Marcellus Member (LMARC) (Figure 6).

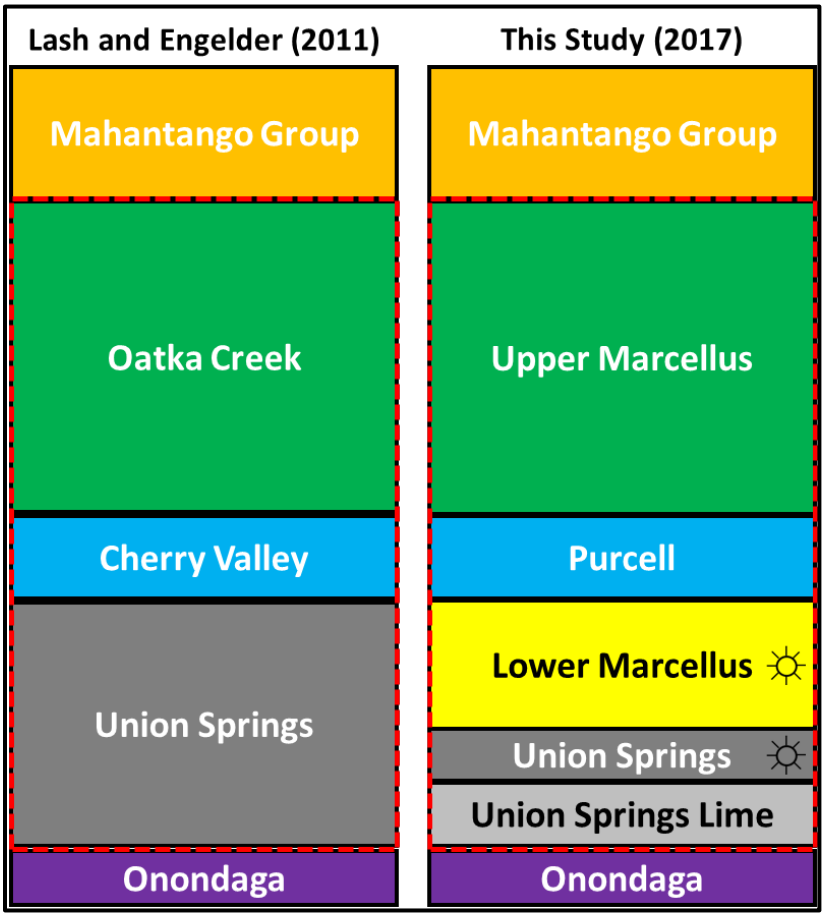

Figure 6: Idealized Stratigraphic Column for the Marcellus Shale. Gas symbols indicate members that are the common commercial targets for horizontal wellbore placement, and will therefore be the members focused upon in this study.

Most published Marcellus depositional models are based on conventional deep basin shale deposition, which implies that Marcellus sediments were deposited in deep, stratified basins and owe their organic richness to anoxic conditions and poor circulation existing at the deepest part of such basins (Johnson et al., 1985; Ettensohn 1992; Lash and Engelder, 2011). These models are patterned after the Black Sea and regard the Marcellus Shale successions as being mostly homogenous with only two broad shale lithofacies; black organic rich shale and grey organic lean shale facies. However, more recently a competing model has been put forth by Emmanuel (2013a) that states that the conventional Black Sea (driven by oxygen-budget and paleo bathymetry) depositional model may not necessarily be appropriate for the Marcellus Shale. Emmanuel (2013a) states that the key controls on the Marcellus Shale deposition in the foreland basin are a combination of local rapid subsidence/uplift events, seasonal variations in nutrient sourcing of algal blooms, changes in salinity and clastic influx rates. Thus, organic-rich laminated Marcellus Shale lithofacies would have been deposited during periods of algal bloom, reduced clastic influx, and increased organic preservation because of changes in bottom water chemistry that favor the deposition of organics and siliciclastics over carbonates. The less organic-rich Marcellus Shale lithofacies in turn were deposited during periods of episodic tectonic quiescence and increased dilution of organic matter as a result of increased clastic influx from the Acadian Mountains. In the same way, the interbedded limestone facies were deposited during times of reduced algal bloom, low sedimentation rates, and changes in bottom water chemistry that favor carbonate deposition over deposition of organics and

siliciclastics. This deposition model is illustrated in Figure 7, for further information regarding this work see Emmanuel (2013a, 2013b).

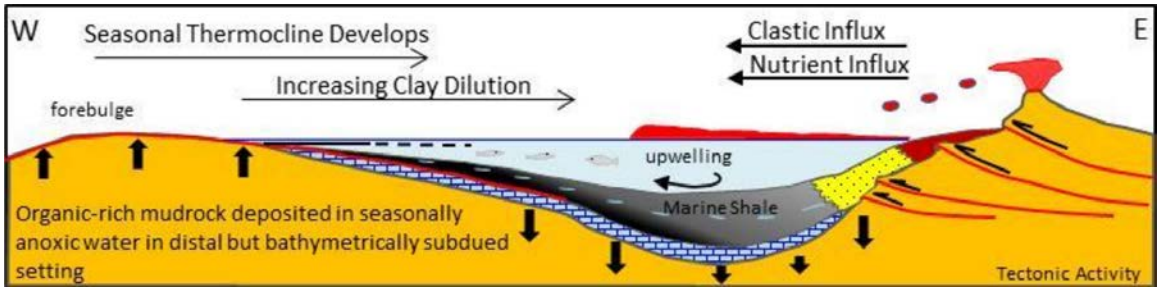

Figure 7: Marcellus Shale Deposition Model. Distal, but bathymetrically subdued depositional environment. Thrust-loading induced down warping of the foreland basin toward the east and uplift of a peripheral bulge in the west (Cincinnati Arch) during early stages of the Acadian tectophase II of Ettensohn (1985), creating an eastward-oriented wedge–shaped basin. Volcanic eruption in the Acadian Mountains provided nutrients which led to algal bloom and the development of thermocline thereby creating seasonally anoxic water, 10-50 m deep (after Tyson and Pearson, 1991; Smith and Leone, 2010). (Taken Emmanuel, 2013a).

1.4 Hypothesis

Based upon well logs like the one included in Figure 8, it appears logical that the low resistivity south of the LOD relates to OM content. Are the unusually low resistivity values measured by open hole logs to the south of the LOD caused by conductive organic turbostratic nano-structures, as suggested by Walters, 2014? If so, is there a connection between the high conductivity inherently associated with such nano-scale structures and the non-commercial outcomes experienced by operators as they approach the LOD? Perhaps the conductive OM is losing the lower end of OM pore ranges due to structural ordering of the carbon as suggested by Beyssac, 2002b.

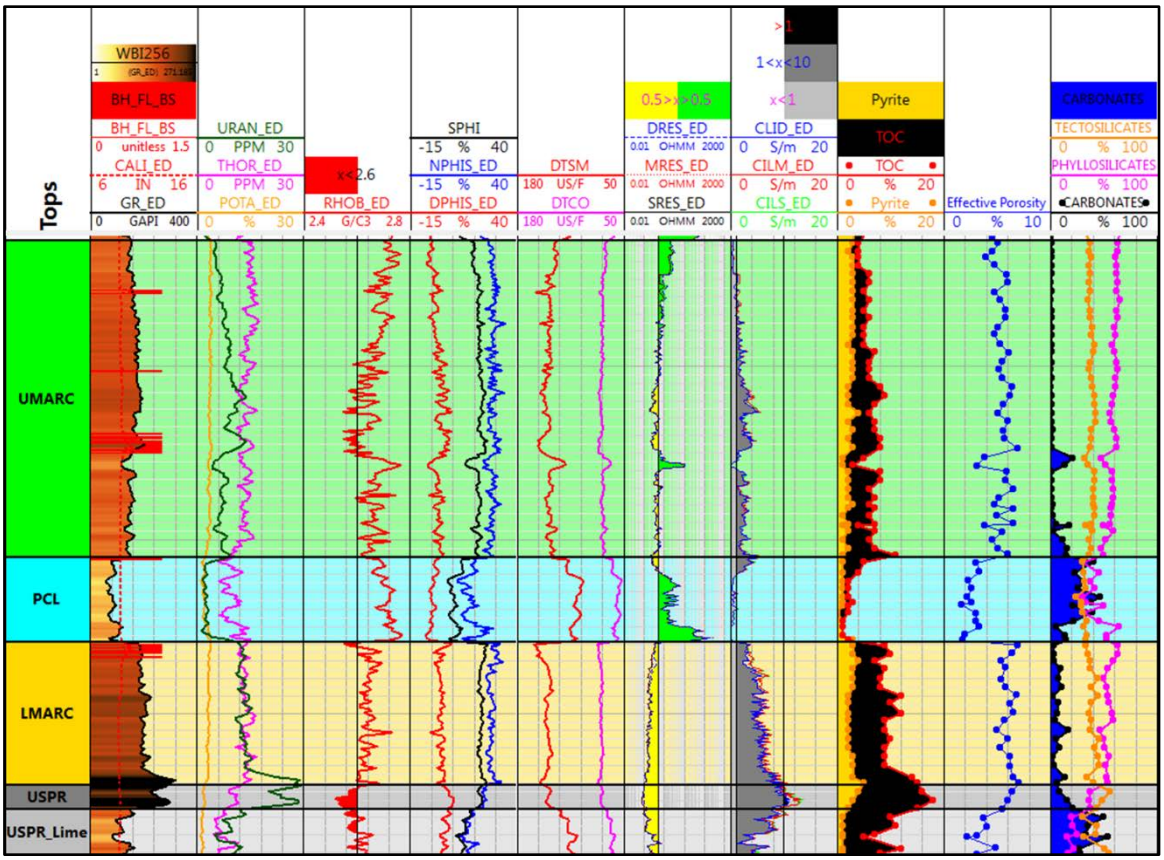

Figure 8: A Typical NE PA Well Log South of the LOD. The Skoronski well log illustrates why industry participants believe TOC is responsible for the low resistivity measurements south of the LOD. For example, the low resistivity in the upper PCL normalizes once TOC < 1.6 Vol%, whereas conductivity and TOC are positively correlated throughout the UMARC, LMARC and USPR.

The Weatherford Work, while inconclusive, opened the door to a new theory regarding the source of the LOD predicated upon "graphitic pyrobitumen" graphitization, a process fundamentally different from smectite diagenesis (the focus of the Shula work) in regard to the temperatures, pressure/stress and time required for its production. The discovery of graphic pyrobitumen in wells south of the LOD could be used to develop an operable explanation for the low resistivity values on, and south of, the LOD. Given that identifying graphic pyrobitumen with XRD is not viable because XRD struggles to illuminate slight structural changes in OM, such as structural carbon ordering, the search

for graphic pyrobitumen would involve techniques such as S/TEM and Raman Spectroscopy. To evaluate how the existence of ordered structures, such as graphic pyrobitumen, impacts the ability of the rock to hold gas, large-scale SEM mosaic segmenting and N_2 adsorption could be utilized to identify changes in pore size distributions (PSDs).The hypothesis of this study is that the resistivity patterns and trends observed in the NE PA Marcellus dry gas window suggest that some type of progressive, yet subtle, OM transition at the nano-scale has occurred south of the observed LOD which has impacted the rock's ability to hold gas.

The goals of this study are to understand the precise nature and cause of the OM transition that exists at the observed LOD in NE PA by comparing samples from conductive, noncommercial wells south of the LOD to samples from non-conductive, productive wells north of the LOD.

1.5 Research Objectives

The objective of this research is to answer the following questions:

1. How does the nano-scale carbon structure of LMARC OM and USPR OM differ between the productive, normal resistivity Marcellus north of the LOD and the noncommercial, extremely conductive Marcellus south of the LOD?
2. If the nano-scale carbon structure of OM differs between the north and south sides of the LOD, are there also quantifiable differences in the organic hosted pores that could explain the noncommercial outcomes experienced in the LMARC and USPR on the south side of the LOD?

2. METHODS

The following section describes the data acquired for this study and the methodology behind its acquisition and analysis.

2.1 Well and Sample Coverage

This study includes seven NE PA wells from Susquehanna, Wyoming and Luzerne counties (Figure 9).

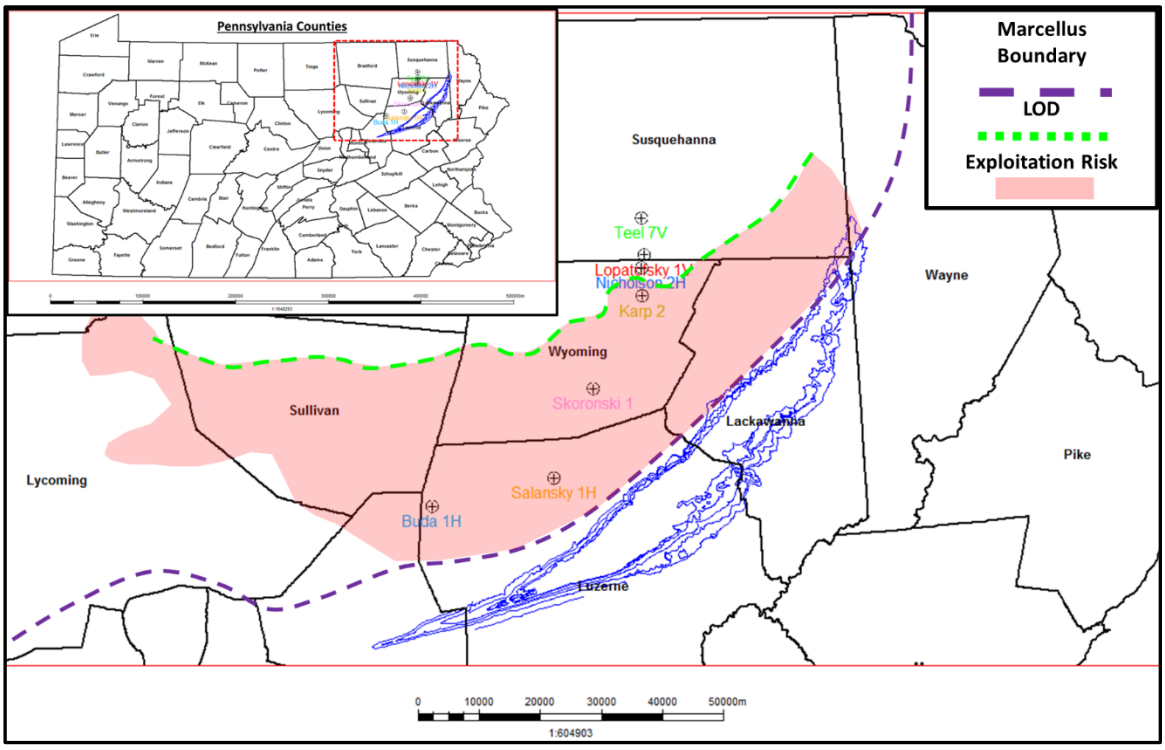

Figure 9: Map of This Study's Area of Interest Marked for Well Dataset. Lackawanna Synclinorium, seen here in blue, taken from Pennsylvania Department of Conservation and Natural Resources. LOD is drawn at the border of productive wells across Susquehanna, Wyoming and Sullivan County as depicted in Figure 3.

Three of the seven wells were successful commercial wells located north of the estimated location of the LOD, whereas the remaining four wells were noncommercial wells located south of the estimated location of the LOD (Table 2).

Data Contributor	Well Name	Logs	Core	Commercial	Conductive
Cabot Oil and Gas	Teel 7V	Yes	Yes	Yes	No
	Lopatofsky 1V	Yes	Yes	Yes	No
Chesapeake Energy	Nicholson 2H	Yes	No	Yes	No
	Karp 2	Yes	No	No	Yes
	Skoronski 1	Yes	Yes	No	Yes
Encana Energy	Salansky 1H	Yes	No	No	Yes
	Buda 1H	Yes	Yes	No	Yes

Table 2: Dataset Description.

The provided well logs generally consisted of Gamma Ray, Resistivity, Density, Sonic, and Porosity curves, while the provided core data consisted of XRD, shale rock properties, and LECO TOC wt%. For this research, new core samples were taken for all the S/TEM, EDS, Raman Spectra, SEM and N_2 Adsorption analyses, as well as for certain incremental XRD and LECO TOC analyses. Well data was visualized using Petrel and Techlog, SEM images were processed by JMicroVision, and Raman Spectra data was analyzed using PeakFit.

2.2 Mudrock Composition

The four wells with core included XRD data prepared prior to this study. The data provided by Cabot and Encana was processed at Weatherford Laboratories in Houston, while the Chesapeake data was processed in their laboratory in Oklahoma City. All preexisting XRD samples were milled to particle sizes <1.0 μm using McCrone micronizing mills. Bulk minerals were analyzed at 2-70 degrees with 0.04-degree increments with 1s per step spin, while clays were analyzed at 2-34 degrees with 0.04-degree increments with 1s per step spin. XRD technicians used the Fullpat method for quantification (Chipera and Bish 2002), which models whole patterns and includes

reference intensity ratios. All new samples were run using the same sample preparation and Fullpat quantification to maintain comparability between the new and legacy data. All XRD data seen in this study will be reported as volume percentages that have been normalized with geochemically derived TOC weight percent (wt%) values.

Preexisting LECO TOC wt% data were derived from standard LECO procedure that includes washing, drying, grinding, and acid digestion before the samples are combusted in an oxygen rich environment to produce carbon dioxide, which flows into a non-dispersive infrared detection cell that quantifies the sample CO_2 and converts the measurements into a dry sample weight of %TOC (Schumacher, 2002). All new samples were run using the same sample preparation and standards to maintain comparability between the new and legacy data.

2.3 Resistivity Assessment

Electrical resistivity logs are routinely used to estimate the type and abundance of fluids (hydrocarbons, formation water) in reservoir rocks. Generally, resistivity logs with low resistivity indicate zones that contain saline connate waters, whereas high resistivity indicates zones that contain potential hydrocarbons or low porosity (Passey, 2010).

The mineral matrix of most reservoir rocks is non-conductive, including hydrocarbons (natural gas and crude oil). Under most circumstances, the primary component of the reservoir that conducts electricity is saline connate water in the pore system that includes surface and interlayered waters. However, rock resistivity can also be influenced by mineral content, and low resistivity may arise from very mature organic matter or conductive minerals like pyrite. Figure 10 is a rock model that illustrates the

variables that affect the conductivity of a mature organic rich gas bearing mudrock like those from the NE PA Marcellus Shale. A large volume proportion of OM and pyrite is relatively rare in conventional clastic reservoirs, but are very prevalent in mature organic rich gas producing mudrocks. Whereas kerogen and solid bitumen are normally nonconductive and yield responses like migrated petroleum, some high maturity shales, including those associated with natural gas production, exhibit anomalously low resistivity (Walters 2014, Yang 2016). Generally, these low resistivity measurements are attributed to the presence of pyrite or the metamorphic conversion of kerogen to conductive graphite. Given that graphite is not seen in XRD analysis of shales exhibiting low resistivity, if graphite-like structures are present, they likely exist in nano-scale domains that are difficult to detect by conventional petrographic methods (Passey, 2010).

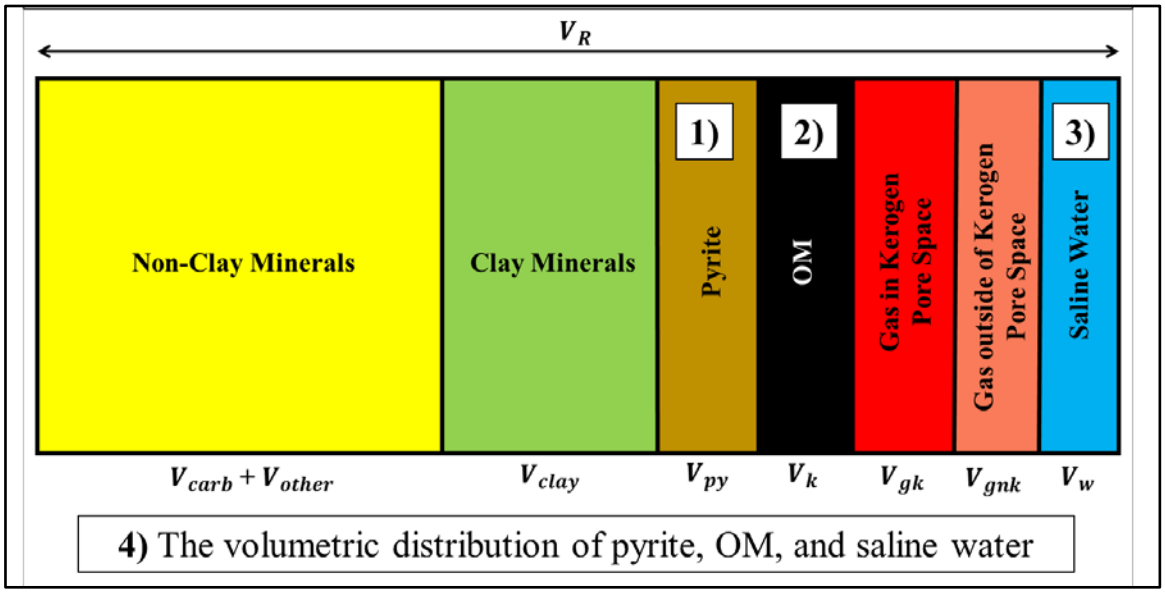

Figure 10: Petrophysical/Composition Rock Model for Organic Rich Mudrocks. This rock model illustrates the four variables that affect the conductivity of a mature organic rich natural gas bearing mudrock like the Marcellus Shale in NE PA.

The existence of nano-scale carbon ordered structures are not well documented in shale associated with natural gas reserves, and it is not clear that such material is responsible for the anomalous electrical conductivity in high maturity gas shales (Walters, 2014). To investigate the existence of nano-scale carbon ordering within the area of interest of this study, two wells from this study's well dataset (the Teel, a productive well north of the LOD, and the Buda, a noncommercial well south of the LOD) were subjected to S/TEM, EDS and Raman techniques. These analyses focused on the LMARC and USPR intervals because they are the common commercial targets for horizontal wellbore placement, and exhibit the highest conductivity south of the LOD.

2.3.1 S/TEM

TEM has a similar optical configuration to an optical microscope in that a flood beam of electrons illuminates a thin sample and the electrons transmitted through the sample are projected onto a viewing screen or camera for observation. Samples must be thin (around 100nm) and the beam energies must be high. Based upon the characteristics of the sample, electrons may either pass through the sample without being scattered or may be diffracted off axis by interaction with the sample. Electrons may also be backscattered in the sample to re-emerge from the top surface. The primary beam also interacts with the sample to produce characteristic X-rays. By choosing the position of the aperture, either the diffracted beam (dark field) or the unscattered electrons (bright field) can be used to form the image. In materials science, the combination of diffraction and imaging provides a unique capability for interpreting the properties of crystals and defects

in crystalline materials. TEM imaging is possible at the nanometer scale, and the spatial resolution can extend to approach the atomic level (Egerton, 2005).

STEM operates in a very similar way to a scanning electron microscope (SEM), which is discussed in Section 2.4.1. A fine, highly focused beam of electrons is scanned over a thin specimen. Electrons which pass through the sample can be collected to produce a variety of transmission images, but as with the TEM, backscattered electrons and X-rays are also produced. Secondary electrons (SE) are also produced, giving yet another imaging mode (Egerton, 2005).

To visualize the OM carbon structure, samples from the Teel and the Buda were imaged with S/TEM at 300 kV on Rice University's FEI Titan Themis S/TEM**.** Four S/TEM OM samples were prepared, one porous and one non-porous for each well. All the samples measured approximately 10 microns across, were prepped by the lift out method (L/O) instead of the trench method (Gianuzzi, 2012), and were located on the ion milled surface of an SEM mount (see section 2.4.1 for SEM sample preparation). The OM samples were protected by a platinum shield and trenched-out and thinned using focused ion beams (FIB) with a 65nA beam current, gradually reducing the bean current to get a smoother finish. Final preparation was done with a 10-100pA beam to polish and incur less damage to the surface. Once thinned to ~100 nm, the wafer thin cross section of OM was detached from the SEM mounted sample and placed on a grid using a glass probe (Gianuzzi, 2012). Figure 11 illustrates an SEM sample before and after executing the lift out method on a piece of OM.

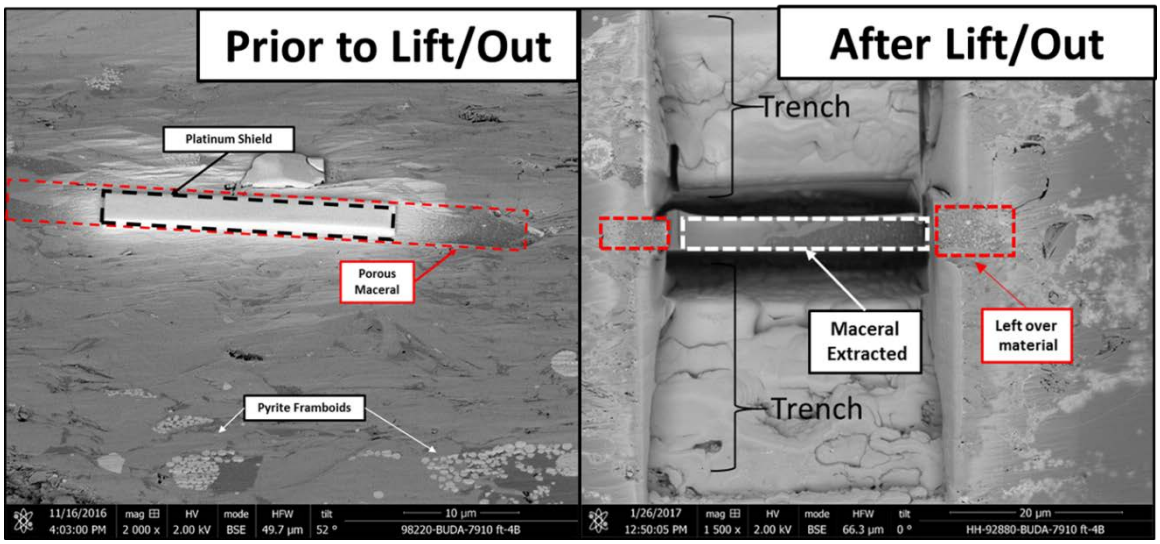

Figure 11: Illustration of S/TEM Sample Preparation. A view of the porous Buda sample, prior to and after performing the L/O extraction method.

2.3.2 EDS

Energy Dispersive X-ray Spectroscopy (EDS) is a qualitative and quantitative X-ray microanalytical technique that can provide information on the chemical composition of a sample. An electron beam is focused on the sample in either a scanning electron microscope (SEM) or a scanning/transmission electron microscope (S/TEM). The electrons from the primary beam penetrate the sample and interact with the sample's atoms. Two types of X-rays result from these interactions: background X-rays, and characteristic X-rays. Both kinds of X-rays are detected by an energy dispersive detector which displays the signal as a spectrum, or histogram, of intensity (number of X-rays or X-ray count rate) versus energy. The energies of the characteristic X-rays allow the elements making up the sample to be identified, while the intensities of the characteristic X-ray peaks allow the concentrations of the elements to be quantified. The underlying principles for generation of X-rays and detection by EDS are the same for SEM and

S/TEM. However, due to the differences between S/TEM and SEM microscopes, and the different accelerating voltages used in their operation, there are some differences in how EDS detectors perform based upon the two microscope types (AMMRF, 2017).

The spatial resolution of EDS analysis in the SEM depends on the size of the interaction volume, which in turn is controlled by the accelerating voltage and the mean atomic number of the sample, Z. For EDS in the SEM, spatial resolution and depth resolution is on the order of a few microns. Because an S/TEM sample is a thin foil, there is less spreading of the electron beam at higher accelerating voltages. Accordingly, higher accelerating voltages can be used which makes the spatial resolution of EDS analysis in the S/TEM on the order of nanometers, while the depth resolution is governed by the thickness of the sample (AMMRF, 2017).

The advantage of using EDS on the S/TEM OM wafers is that it eliminates the interference from the material beneath the OM, unlike the standard SEM EDS process. The higher accelerating voltages used in S/TEM analysis allows for identification of more elements due to the excitation of higher energy K and L lines which further differentiates overlapping peak signatures from visibility of both primary and secondary peaks of an element (Figure 12). The S/TEM EDS analysis has a superior detection limit compared to the SEM EDS analysis (~0.01-0.1 wt% compared to 0.1-0.5wt%, respectively). Accordingly, an S/TEM EDS analysis is better suited for trace element identification, whereas a SEM EDS analysis is appropriate for major and minor element identification. (AMMRF, 2017).

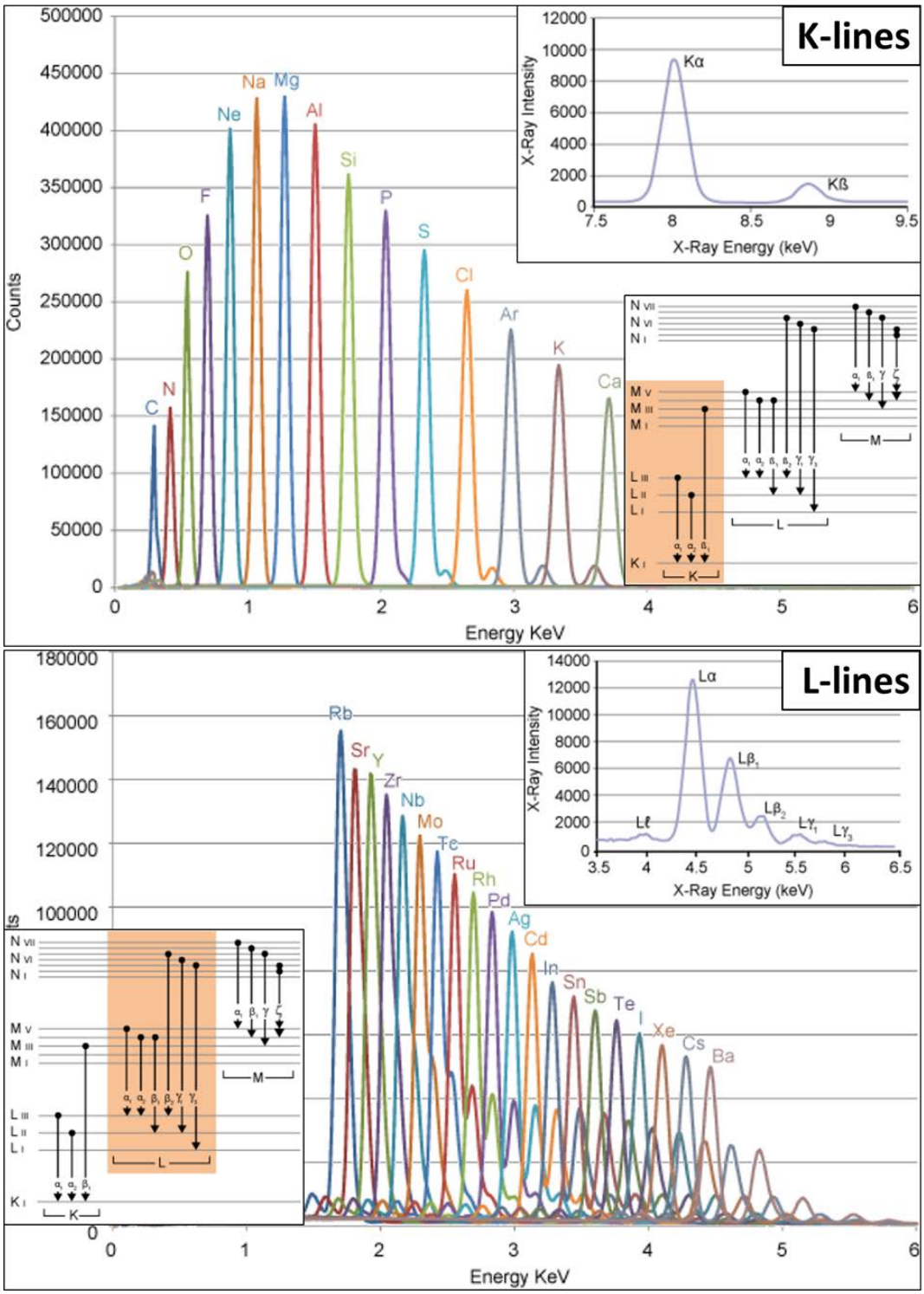

Figure 12: Elements resolvable through interaction with L-line and K-line emissions (AMMRF, 2017).

To indentify the composition of the mineral inclusions found in the porous OM samples of the Teel and the Buda, S/TEM EDS was performed at Rice University (using voltage of 300 kV and a scan time of ~5 minutes) and SEM EDS was performed at Weatherford Labortories in Houston (using a Helios NanoLab 650 to produce large elemental maps with 2500X magnicifaction at 25 kV with a 25 minute scan time and an average point count rate of 8,000 counts per second). After the large SEM EDS maps were completed, certain OM and other material of interest had spot spectrums collected (at 25kV with a 15 second scan time and an average point count of 8,000 counts per second). An EDS OM spot scan can be seen in Figure 13.

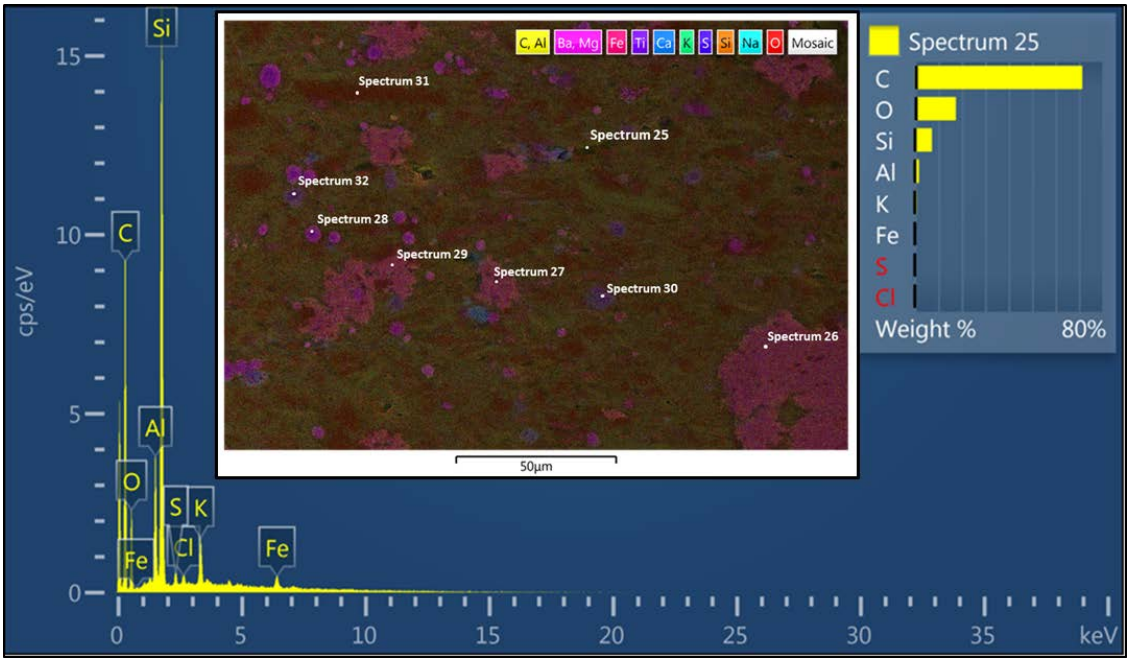

Figure 13: Illustration of SEM EDS Output. The large graph is a EDS Spot Histogram taken from a piece of OM (Spectrum 25). The EDS Map, in the middle, indicates the spot spectrum locations. The upper right is a wt% graph of OM (Spectrum 25), which contains mainly carbon with quartz and clay inclusions.

2.3.3 Raman Spectroscopy

OM graphitization is characterized by a multi-scale organization, including structure (organization at the atomic scale within aromatic layers) and the microtexture (mutual organization in space of the aromatic layers). Raman spectroscopy provides indirect information on a sample's structure through its vibrational properties, which are used to determine the degree of graphic ordering in OM samples. Raman spectroscopy of carbonaceous material occurs at two wavelength bands. The first, known as 'first order bands' occur between 1100 and 1800 cm^{-1} (Tuinstra and Koenig, 1970). The spectra of organic material in this order is characterized by two main bands; the disordered (D) band, which occurs ~1350 cm^{-1}; and the ordered graphitic (G) band, which occurs at ~1600 cm^{-1}. However, less mature (lower grade) poorly organized OM can have additional bands appear in the first order region around ~1245 (D4), ~1510 (D3) and ~1620 (D2) (Figure 14) (Lunsdorf, 2014a).

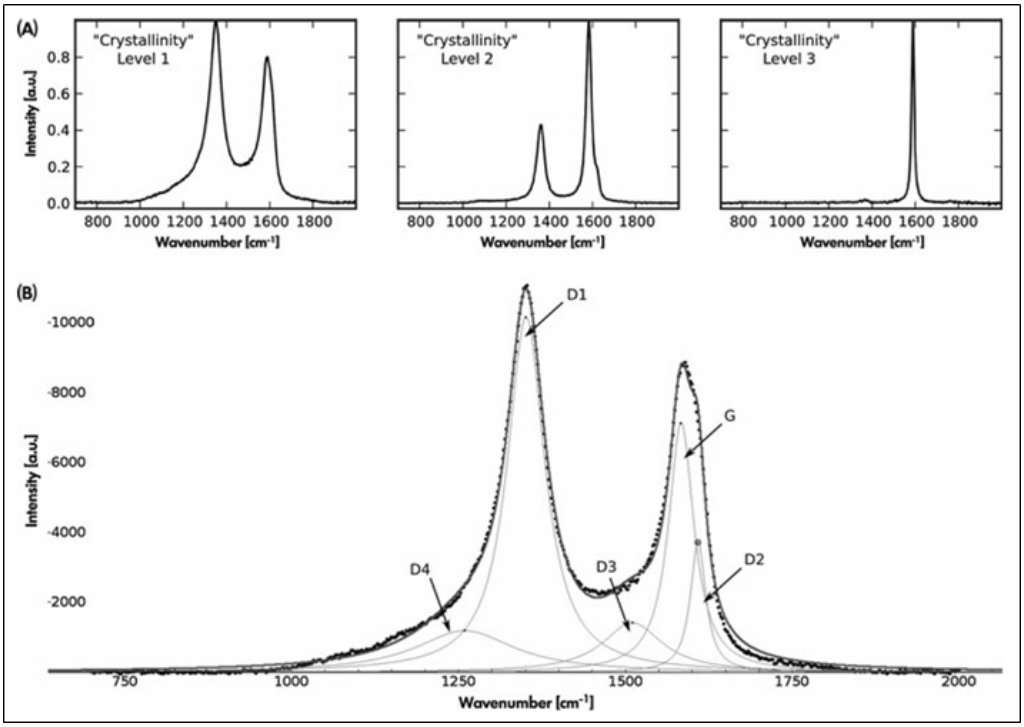

Figure 14: Illustration of Carbonaceous Raman Spectra. **(A)** Representative Raman spectra of three 'crystallinity levels'. **(B)** An example of the decomposition of a 'Crystallinity Level 1' Raman spectrum by five components according to Lahfid et al. (2010). The first order region is described by D1, D2, D3, D4 and G bands. D4 widens the low wavenumber side of the D1 band, while D2 appears only as a weak shoulder on the high wavenumber side of the G band (Taken from Lunsdorf, 2013).

The D1 band, between 1350 and 1380 cm^{-1}, corresponds to the breathing mode of the sp^2 aromatic ring within a graphitic cluster (Beyssac, 2002a) (i.e. it is the vibrational mode of a disordered graphitic lattice). D1 is thought to arise from heteroatoms containing units or other defects in graphene-layered carbon atoms that are near lattice disturbances (Katagiri, 1988). The D1 band in poorly ordered carbon can be broader due to the contribution of the D4 band centered at ~1245 cm^{-1}. The D4 band normally appears as a broad shoulder of the D1 band in poorly ordered OM and is related to vibrations originating from aliphatic (open chain) hydrocarbon chains and are not associated with aromatic or graphitic systems (Ferralis, 2016). In more ordered carbon, the D4 band is absent and the D1 band area

reduces with stiffening of the aromatic planes (Beyssac, 2002a). To learn more about these disordered bands, see the work done by Tuinstra & Koenig (1970), Robertson (1986), Wang et al. (1990), Cuesta et al. (1994), Jawhari et al. (1995), Dippel et al. (1999), Escribano et al. (2001), Mathews et al. (1999), and Sato et al. (2006).

The G band, between 1580 and 1615 cm^{-1}, is related to an in-plane sp^2 bond stretching shear vibration within the aromatic ring of a large, graphene-like cluster (Beyssac, 2002a) (i.e. the in-plane vibration of aromatic carbons in carbonaceous materials that at some level have a graphitic structure). As disordered OM matures and becomes more ordered the G band shifts down to 1580 cm^{-1}, and displays the additional peak at 1620 cm^{-1}, called the disordered two peak (D2) (Beyssac 2002a).

The significance of a D2 band is not well understood, but it is always present when the D1 band is present, and the intensity of D2 decreases with increasing degrees of maturity and organization. In lower grade disordered OM, G and D2 occur as a broad band at 1600 cm^{-1} in which the D2 shoulder cannot be resolved (Beyssac, 2002a), and a D3 band can also be seen at ~1510 cm^{-1}. The D3 band, a very wide band situated between the D1 and G bands, and is attributed to out-plane defects of non-aromatic rings such as tetrahedral carbons suggesting that this kind of defect is released early in the graphitization process (Sadezky, 2005; Beny-Bassez and Rouzaud 1985).

The second order bands of Raman spectroscopy of carbonaceous material, which occur from 2700 to 3100 cm^{-1}, include several bands which relate overtone and combination scattering (Wopenka and Pasteris, 1993), but are not yet clearly understood. Work done by Lespade et al. (1984) showed that the 2700 cm^{-1} band (S1 band) splits into

two components during the final stage of the graphitization process. This splitting was interpreted to be the result of the transition from a two-dimensional structure to a tridimensional structure. The 2900 cm^{-1} band (S2), which appears only in poorly ordered carbon, has been interpreted by Tsu et al. (1978) to be a consequence of C-H bonding, but this interpretation is still being debated (Beyssac, 2002a). The second order bands from 2700 to 3100 cm^{-1} were recorded for the initial samples processed in this study. Given that no discernable second order bands were identified in the initial samples, and because these bands require much longer scan times, recording for the higher order spectra was eliminated from the workflow.

Different phases of ordering occur as carbonaceous material evolve from very low-grade, highly disordered material (i.e. 150-250 degrees Celsius) to very high-grade, near perfect crystalized graphite (i.e. 500-600 degrees Celsius). This evolution of carbonaceous Raman spectra in relation to metamorphic grade is illustrated in Figure 15.

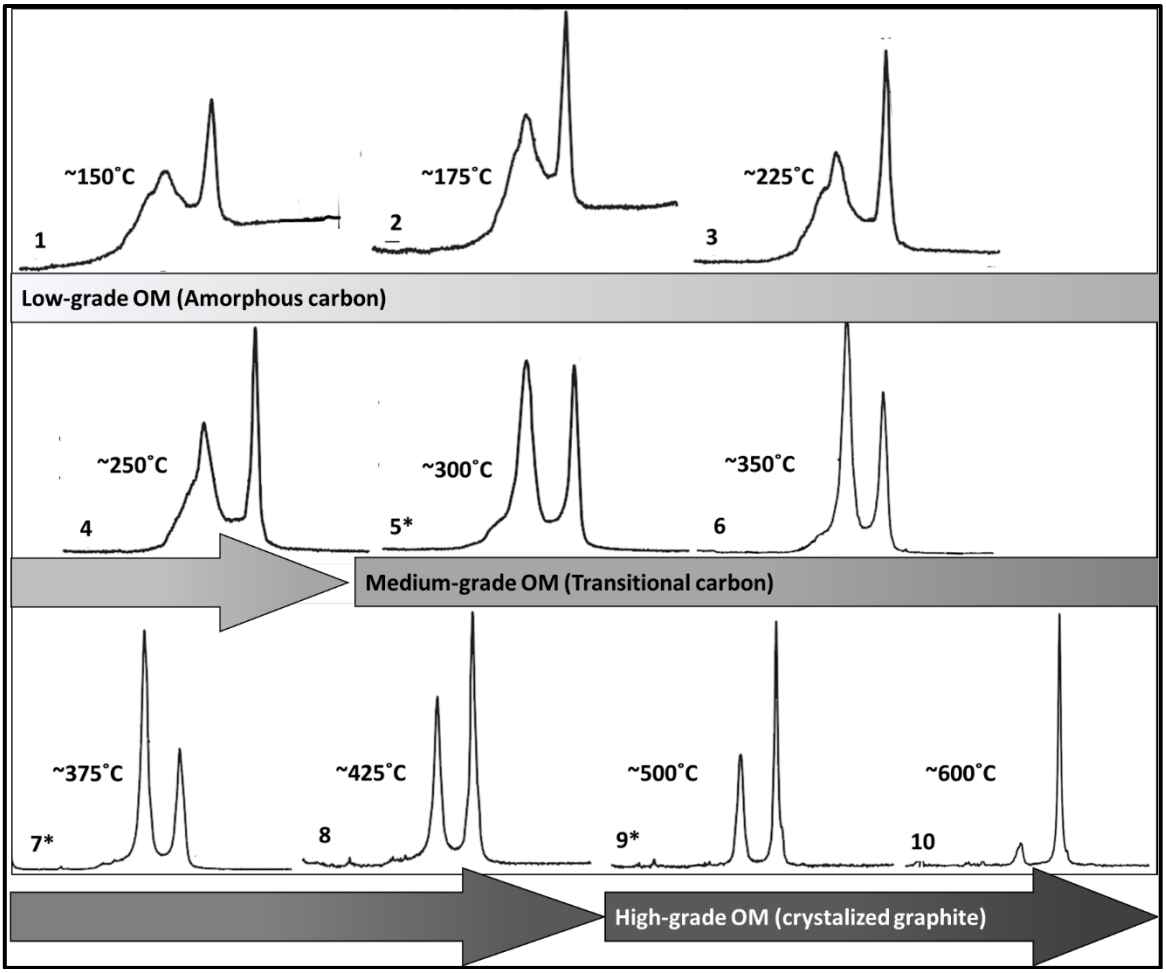

Figure 15: Progressive Ordering of OM at Varying Temperatures. * denotes major spectrum deviation signifying a significant ordering event within the OM structure. Spectra #5 marks the first major structural ordering shift while still maintaining the D4 shoulder but with a much more intense D band. Spectra #7 marks the loss of D4 and D3 bands as well as the beginning of the decrease in D band intensity relative to the G band. Spectra #9 marks the separation of the G and D2 band as the G shifts down to 1580 cm-1 and D2 to 1620 -1 Lunsdorf (2014b).

Conventional metamorphic rock studies quantify the maturity of sp2 carbonaceous material using the Raman parameters of R1 (the intensity ratio) and R2 (the area ratio) as outlined by Beyssac et al. (2002a, 2003a). Generally, R1 ($D_{intensity}$/ $G_{intensity)}$ and R2 ($D1_{area}$/(G_{area}+$D1_{area}$+$D2_{area}$) decrease with increased maturity and carbon ordering. However, in low-grade (<300 degrees Celsius) rock with poorly ordered spectra (broad D4, D1, D3 bands), the traditional Beyssac 5 Voigt function method does not provide

unique results as the method's parameters do not appropriately consider these variables. To fine-tune the application of Raman Spectroscopy to low-grade rock, like those examined in this study, the Lahfid (2010) method and the Kouketsu (2016) method were developed. Lahfid (2010) applies a 5-peak deconvolution method that uses Lorenz functions and two area ratio parameters; RA1=(D1+D2)/(D1+D2+D3+D4+G) and RA2=(D1+D4)/(D2+D3+G). Generally, both ratio's increase with increased carbon ordering. To learn more about this method see Lahfid (2010). To solve the common issue of how best to fit the G and D2 bands within low-grade rock spectra, Kouketsu derived a deconvolution method that uses a combination of fixed and unfixed pseudo-Voigt (Gaussian Lorentzian Sum)/Lorentzian functions depending on the G/D intensity ratio of the raw spectra. If G/D >1.5 then the spectrum is fit with 4 bands with a fixed D3 and D4 band at 1510 cm^{-1} and 1245 cm^{-1} and no G band. If G/D < 1.5 the spectrum is fit with 5 bands with a fixed G band at 1593 cm^{-1} and fixed D4 band at 1245cm^{-1} (Figure 16). To learn more about this method see Kouketsu (2016).

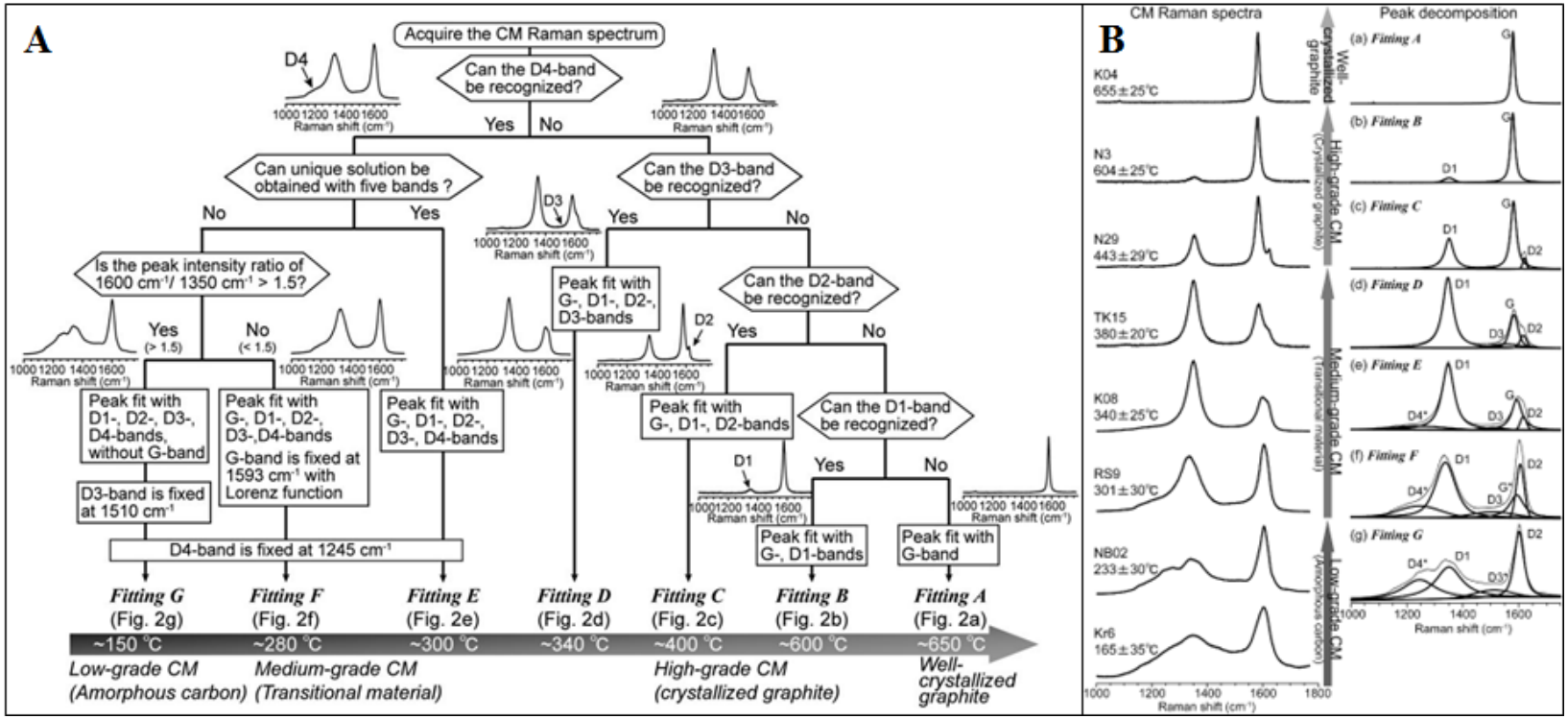

Figure 16: Summary of the Kouketsu Deconvolution Method. (A) Flowchart of the seven peak fitting procedures used by Kouketsu (B) OM Raman spectra for several representative samples and their corresponding Kouketsu Method peak fittings. Asterisks in the band name in (e) to (g) signify that the center position of that band was fixed by a Kouketsu Method parameter.

Raman spectroscopy was performed at Premier Oilfield Services on their HORIBA LabRAM HR Raman Microscope (Figure 17) using SEM mounts. Samples were ion milled and were not coated. A laser excitation wavelength of 532 nm, numeric aperture (NA) of 0.90, 100x objective, grating size of 600 $mm^{-1,}$ 1-2 um focal volume were used for all Raman samples. The goal of this investigation was to record a clear OM Raman signal from the samples to investigate differences in carbon ordering between the north side and the south side of the LOD.

Figure 17: Picture of HORIBA LabRAM HR Raman Microscope.

At the USPR and LMARC members of Teel and Buda, five separate OM spot Raman spectra were produced and averaged into one OM spectra. In total, six OM spectrums were produced; one LMARC and two USPR from the Teel, and one LMARC and two USPR from the Buda. All raw spectra were fit with a standard linear baseline using LabSpec6 with 2 degrees and 4 max points.

2.4 Reservoir Quality Assessment

As the Marcellus Shale is comprised of organic rich mudrock, the porosity is composed mainly of organic hosted porosity (Milliken et al., 2013). Porosity was analyzed to determine if OM from the south side of the LOD has less capacity to hold gas than OM from the north side of the LOD. To better characterize these organic hosted pores, large SEM mosaicked images were used to capture a representative sample of the rock that would allow for OM and OM hosted pore segmentation. Given that the resolvable limit of the visual SEM images is 20nm, N_2 adsorption was also performed to indirectly non-visually characterize the area and volume contribution of pores, including those beyond the resolvable limit of SEM.

2.4.1 SEM

A scanning electron microscope (SEM) is a type of electron microscope that produces images of a sample by scanning the surface with a focused beam of electrons. The electrons interact with atoms in the sample, producing various signals that contain information about the sample's surface topography and composition (Egerton, 2005). The signals used by a SEM to produce an image result from interactions between the electron beam and the sample’s atoms, at various depths, within the sample with the most common

signals used being secondary electrons (SE) and back-scattered electrons (BSE) (Egerton, 2005).

In secondary electron imaging, the secondary electrons are produced from the surface of the sample or topmost part of the interaction volume from inelastic scattering. Back-scattered electrons (BSE) are beam electrons that come from the top half of the interaction volume and are reflected from the sample by elastic scattering (Goldstein, 1981). Because BSE emerge from deeper locations within the specimen, the resolution of BSE images is less than SE images. However, BSE are often used in analytical SEM because the intensity of the BSE signal is strongly related to the atomic number (Z) of the specimen, and BSE images can provide information about the distribution of different elements in the sample (Clarke, 2002). For this same reason, BSE imaging can view OM within mudrock with definitive contrasts, which is difficult to detect in secondary electron (SE) images of geologic samples (Figure 18).

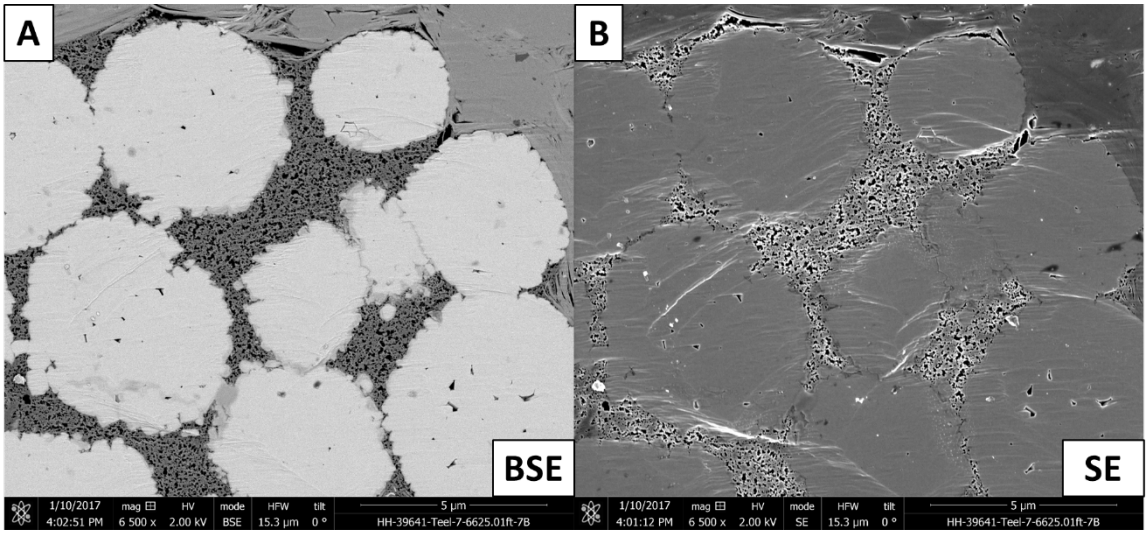

Figure 18: SEM Imaging Mode Comparison. **(A)** Pyrite framboids filled with very porous OM imaged with BSE, **(B)** The same pyrite framboids filled with very porous OM imaged with SE. These images demonstrate BSE's superior contrasting of key features (i.e. OM, pores, pyrite and matrix), as well as SE's white halo effect around OM pores which can hinder accurate pore segmentation.

Most published SEM work relating to organic rich mudrock are imaged at higher acceration voltages (10-20kV). Higher acceleration voltage can be produced faster than SEM imaging prepared with lower acceleration voltage because higher voltage produces fewer lens aberrations, thus reducing the need for frequent tool aligment. Lens aberrations result in a diffuse ring of scattered electrons around the probe, which degrade image contrast and broaden the probe size (Asahina, 2012). The disadvantages however of using 10-20kV is that it results in deeper sample penetration and surface feature fuzziness that can limit the capability of accurate 2D surface image segmentation. A skilled SEM technician can image at lower acceleration voltages and reduce the occurances of lens aberations by actively managing hardware alignment, but at the expense of longer image aquistion times. Given that edge clarity and greyscale contrast are critical to the image

segmentation required for this study, a voltage of 2kV was utilized for imaging (Figure 19).

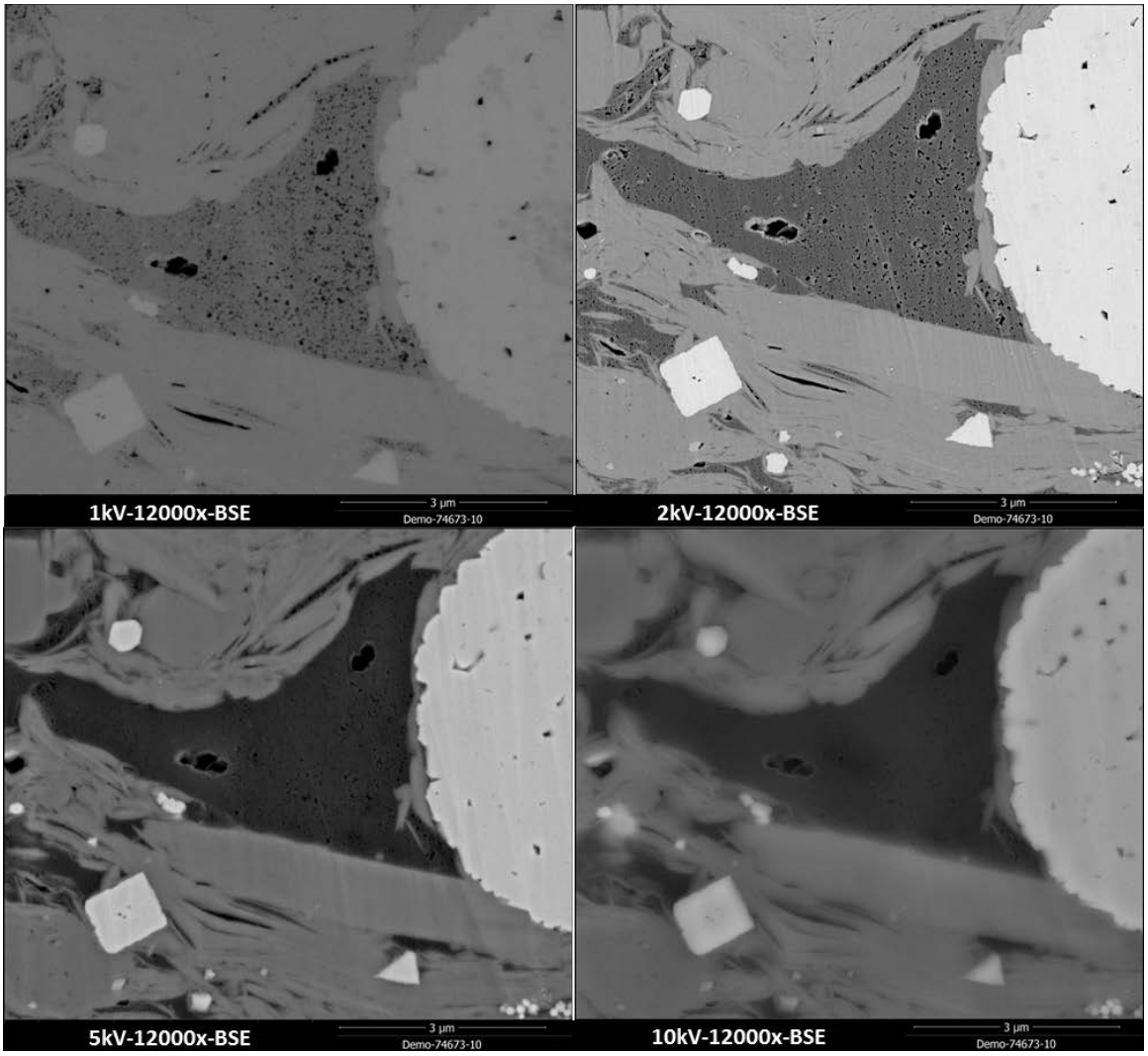

Figure 19: SEM Image Voltage Comparison. These SEM images of a OM sample with pyrite were processed at multiple voltages to illustrate the resulting differences in greyscale and edge sharpness. 1kv lacks the greyscale contrast necessary to accurately distinguish OM from other grains, but produces superior edge sharpness. Both the 5 kV and the 10 kV exhibit the appropriate grey scale contrast, but lack edge sharpness. 2 kV is a happy medium, having both grey scale contrast and edge sharpness.

SEM sample surfaces were prepared by argon-ion cross section milling at Weatherford Laboratories in Houston by using an accelerating voltage of 4kV, a sample

current of 20µA per beam (two beams), and a milling time of 8 Hrs. A conductive coating of iridium is applied to the sample surface to assist in the control of charging during high resolution imaging on the SEM, which was a Helios NanoLab 650.

SEM imaging was performed on the LMARC and USPR intervals of the Teel (a productive well on the north side of the LOD) and Buda (a noncommercial well on the south side of the LOD). At each interval, five separate mosaics, each covering approximately 24,032 μm^2, were prepared from twenty-five 39.8 µm wide BSE images (each taken at a magnification of 2500X at 2kV). For each interval, the five separate mosaics cover approximately 120,160 μm^2 (0.12 mm^2) of the sample surface area, which offers a representative sample of the Teel and the Buda at these intervals (Figure 20).

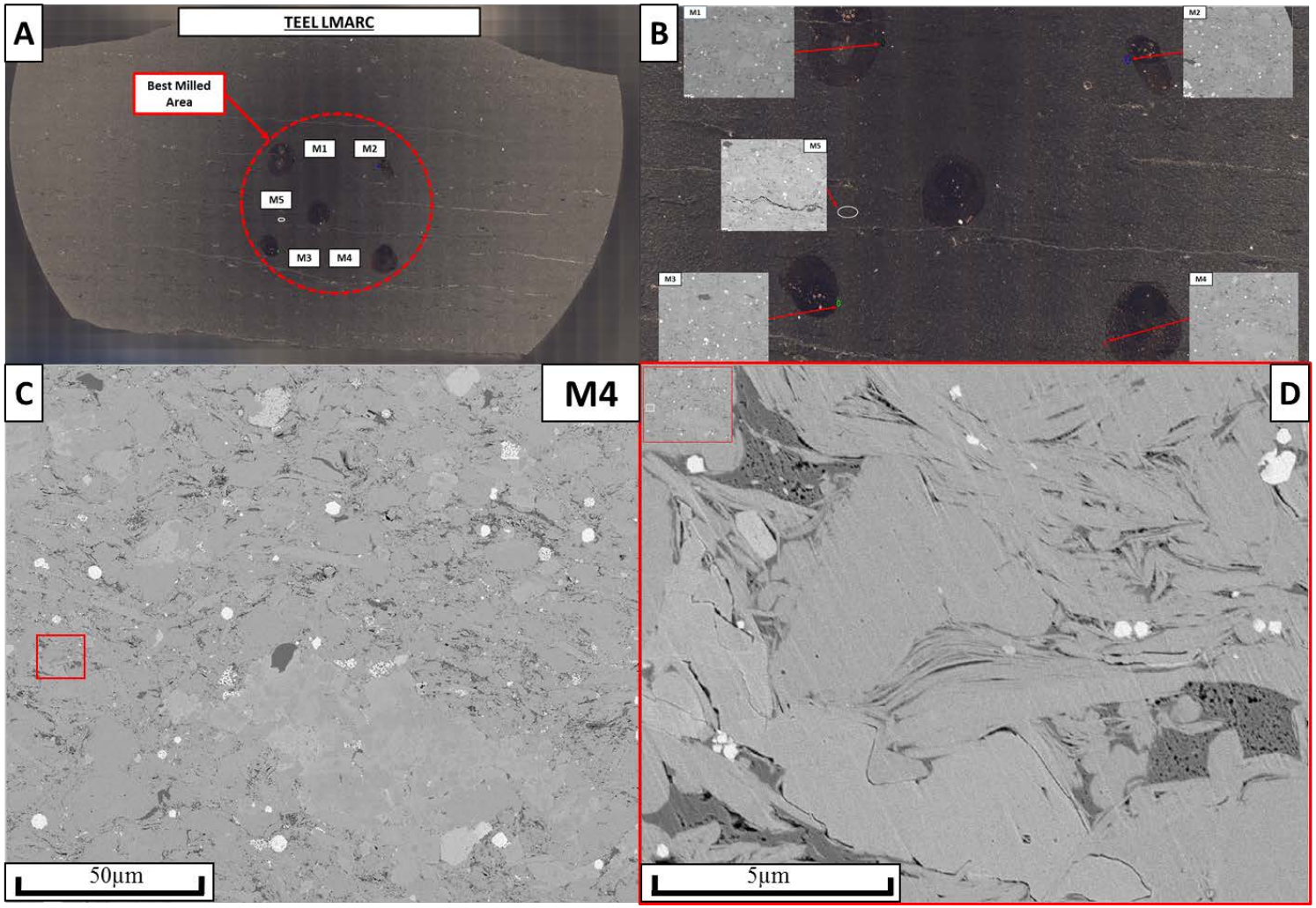

Figure 20: Examples of this Study's SEM Imaging. **(A)** Reflected light image of a SEM sample. **(B)** Magnified image of slide (A) with mosaic images for each landmark dot. **(C)** View of the coverage provided by Mosaic M4. **(D)** 1-micron view of M4, which demonstrates how the crisp edges, distinct grey-scale, and high pixel density of SEM imaging facilitates OM segmentation.

Mosaics from the Teel and Buda were imported into JMicroVision for global and local segmentation. Before segmentation, the mosaics are spatially calibrated using the known mosaic width. The OM and pores are then globally segmented using the object extraction tool with their defined grey scale ranges. The OM objects extracted are then manually examined to illuminate any non-OM objects that have grey scale similar to OM, such as plucked pieces of the surfaces and interparticle porosity. Once OM has been globally segmented and manually verified as OM, the data is sorted and all large OM ranging from 1 um^2 to the largest resolved OM are locally segmented to quantify their organic hosted pores. To segment only organic hosted pores, each OM object requires a new 2D boundary polygon to run the automatic object extraction tool on the single OM object itself. All 20 mosaics (five from Teel LMARC, five from TEEL USPR, five from Buda LMARC, and five from Buda USPR) were subjected to global segmentation of all OM and all pores at their set grey scale ranges. Additionally, one mosaic from LMARC and USPR for each well was subjected to local pore segmentation of all large ($\geq 1 \mu m^2$) OM (Figure 21).

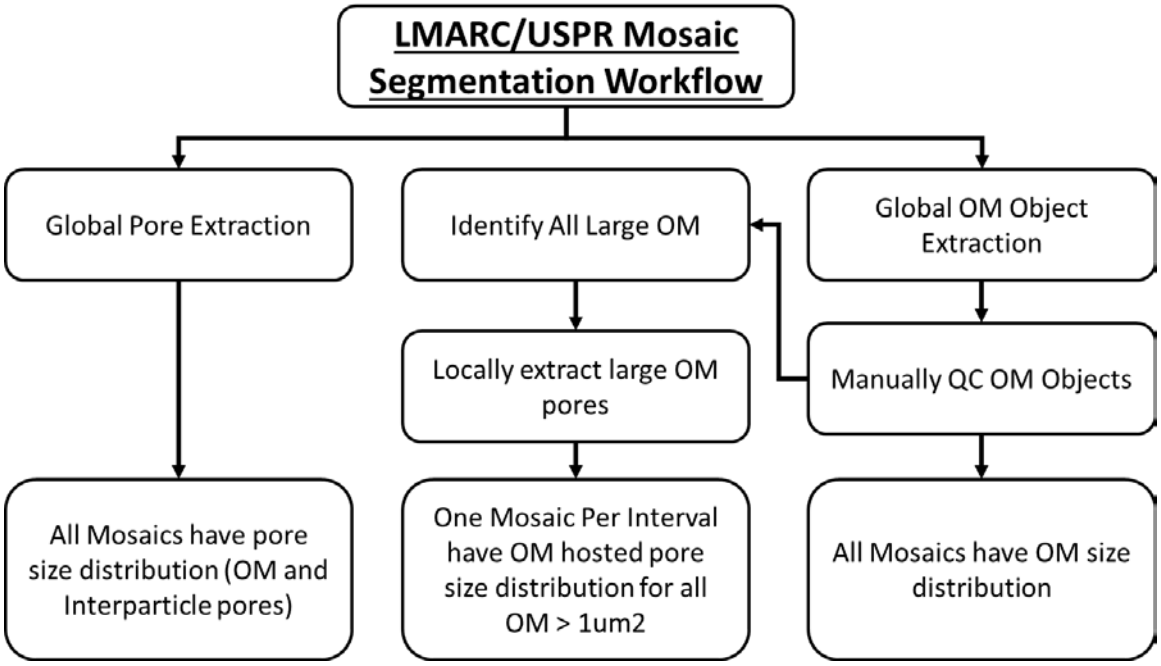

Figure 21: This Study's SEM Segmentation Workflow.

As seen in Figure 22 the mosaics can be automatically segmented using the JMicroVision object extraction tool with a great deal of accuracy. To image a large field of view that provides a representative sample while still maintaining high pixel density, the mosaics were made up of 2500X images, which allows for confident resolvable pore size down to 20nm. To mitigate the 20nm resolvable limit of the SEM imaging, N_2 adsorption was performed at the same sampled intervals to quantify volume/area contributions of pore sizes below 20 nm.

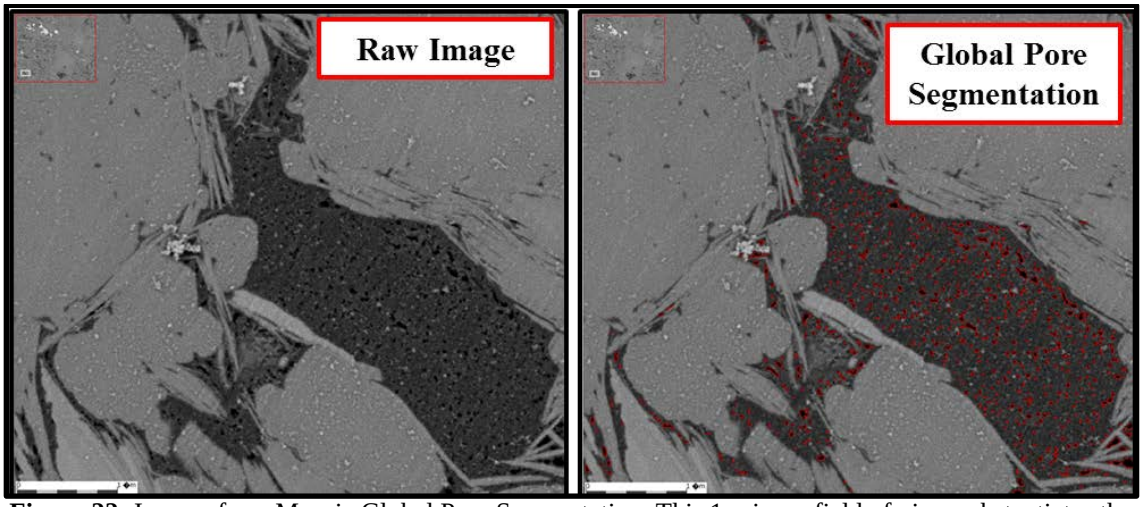

Figure 22: Images from Mosaic Global Pore Segmentation. This 1-micron field of view substantiates the claim that the 2kV 2500X mosaic has adequate grey scale contrast and edge crispness needed to facilitate the automatic extraction of pores by the JMicroVision using the object extraction tool.

2.4.2 N_2 Adsorption

To quantify the volumes and areas of the upper end of micro pores (<2nm), mesopores (2-50 nm in diameter) and macropores (>50nm in diameter), low pressure N_2 adsorption was performed at Premier Oilfield Laboratories. Samples from Teel and Buda were crushed to 32-90 microns and de-watered in a vacuum dry oven at 125C overnight and data was taken with a Micrometrics ASAP 2020 Surface Area and Porosity analyzer.

The analysis, which is run at the temperature of liquid nitrogen (77.2 K), slowly increases the partial pressure of the adsorbate and nitrogen gas. The nitrogen condenses or adsorbs on the surface at different partial pressures as a function of pore size. Figure 23 shows an example of adsorption/desorption isotherms analysis optimized to return high pore-size resolution on shales.

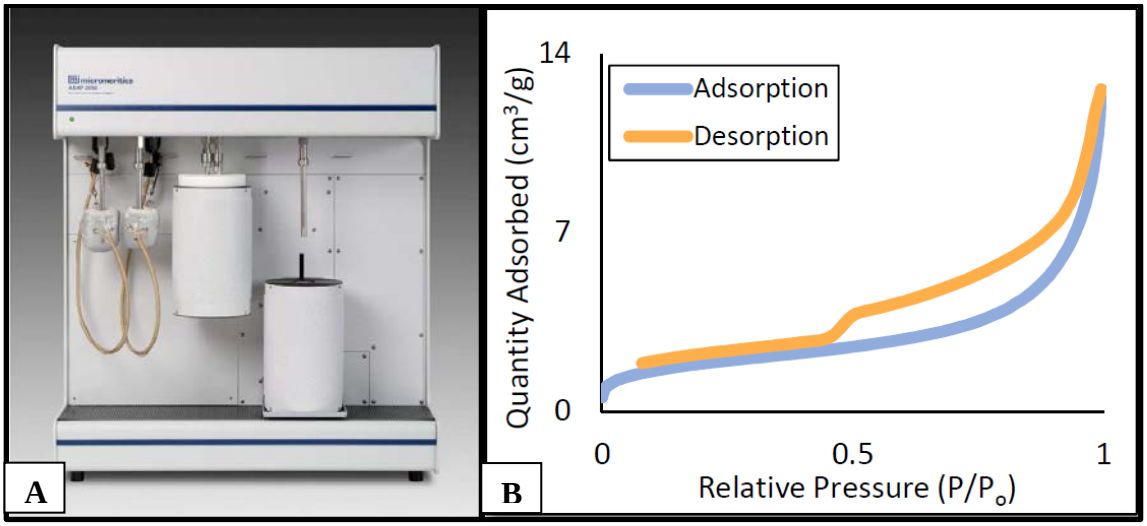

Figure 23: N_2 Absorption Apparatus and Output Example. **(A)** Micrometrics ASAP 2020 Surface Area and Porosity Analyzer **(B)** Output from an optimized Adsorption/Desorption isotherm analysis which provides information on pore volume, surface area, and pore size distribution.

N_2 attraction and adsorption of gas molecules on the surface of a sample occurs in four distinct stages due to the three pore modal domains present in the rocks (micro, meso, and macro) (Figure 24). At low pressures, single molecules begin to adsorb on the sample, then as the pressure is increased monolayer molecules begin to form on the surface which is an indication of the presence of micro pores. At relative pressures greater than 0.9, capillary and condensation of N_2 occurs in larger mesopores and macropores leading to remarkable adsorption with multi-layer coverage. Finally, gas saturation is reached with complete surface coverage. However, there is no observable plateau of adsorption even at the maxima of the experimental relative pressure (0.995), indicating that some larger macropores are still not fully filled by N_2 at the maximum relative pressure (Sing, 1985).

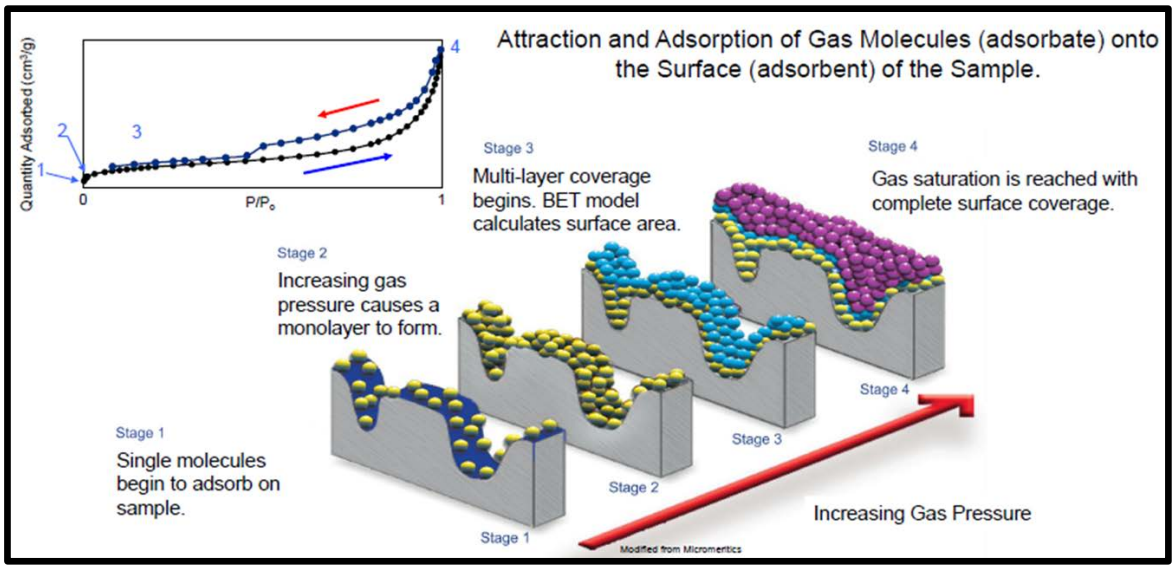

Figure 24: Summary of N_2 Adsorption Process. The four distinct stages of N_2 attraction and adsorption of gas molecules onto sample surface **(**Micrometrics modified by Premier).

Nitrogen adsorption isotherms have historically been modeled using the BET (Brunauer-Emmett-Teller) model which determines surface area on a model of adsorption that incorporates multilayer coverage. While the BET model is reliable for materials with a Type II or Type IV isotherm that have sufficient levels of interaction between the adsorbate gas and the surface (Sing, 2001), for materials with other types of isotherms the BET model may not apply for various reasons and therefore should be treated with caution (Sing, 2001). Because most shales have a wide PSDs that extend down into the microporous range, when subjected to low pressure N_2 adsorption testing they exhibit Type I (micropores) and Type IV (mesopores/macropores) isotherms. Accordingly, the BET model was not considered appropriate for this study. Another model for modeling nitrogen adsorption named the BJH (Barrett-Joyner-Halenda) model calculates pore size distributions from experimental isotherms using the Kelvin model of pore filling.

However, the BJH model is also a poor fit for mudrock samples, like those in this study, because the BJH model also does not account for micropores (Mroczkowska, 2015).

Given that neither the BET model nor the BJH model were appropriate for the Marcellus mudrock samples in this study, the N_2 adsorption isotherms were processed using Non-Local Density Function Theory (NLDFT), which is a form of the Density Function Theory (DFT) model. In general, the DFT model is based on the molecular statistical thermodynamics equation that calculates the specific adsorption amount in an individual pore range at a given experimental temperature and pressure by solving the function of grand thermodynamic potential in terms of the distribution of gas density in a specific pore space (Seaton, 1989). The NLDFT was applied to obtain pore size distributions, pore surface areas and pore volumes. The adsorption isotherms were predicted by NLDFT for individual slit pores and were correlated as a function of pressure and pore width. The pore size distribution was then calculated by fitting this correlation to the experimental adsorption isotherm of the sorbent (Seaton 1989).

A drawback of the NLDFT method is that it does not consider chemical and geometrical heterogeneity of the pore walls, but instead assumes a structureless, chemically and geometrically smooth surface model. The consequence of this mismatch between the theoretical assumption of smooth and homogeneous surfaces and the inherent molecular scale heterogeneity of real adsorbents is that the theoretical NLDFT adsorption isotherms exhibit multiple steps, with a step for each layering transition (i.e. a step for the formation of the initial monolayer, a step for the second adsorbed layer, and so on). In microporous carbon materials exhibiting broad PSDs, these artificial layering steps cause

artificial gaps in the calculated PSDs around 1nm and 2nm (Ravikovitch, 2000; Olivier, 1998). For more details about DFT methods, read Landers (2013).

Recently, the NLDFT method was advanced to consider the molecular level surface roughness that is typical to most carbonaceous and siliceous materials as well as other materials including hybrid organic–inorganic hierarchical structures (Ravikovitch, 2006a). This technique, named the quenched solid density functional theory (QSDFT), was shown to be more practical then NLDFT for the analysis of microporous and mesoporous carbons (Neimark, 2009; Gor, 2012) due to the lack of artificial gaps at 1 and 2nm. Unfortunately, this technique could not be implemented for this study. For more details about DFT methods, read Landers (2013).

3. RESULTS

This study confirmed that many of the attributes which characterize noncommercial wells on the south side of the LOD are similar to the attributes of productive wells on the north side of the LOD. However, this study's investigation and testing of the nanometer domain of the Marcellus identified several remarkable differences, and noted other findings that require further research.

3.1 Mudrock Composition Comparison

Most petrophysical methods applied to organic rich mudrock reservoirs seek to understand their organic richness and geomechanic behaviors to optimize hydraulic fracturing. The presence of clay minerals within mudrocks result in plasticity and ductility, which are not conducive to fracking. Alternatively, mudrocks with high silica and carbonate content result in zones of brittleness and high elastic moduli which are optimal targets for fracking and horizontal well bores.

The Marcellus Shale in NE PA does not suffer from swelling clays or high clay content zones except for a few very thin ash beds at the base of the USPR at the top of the Onondaga limestone (Klapper, 1971). Figure 25, which is based upon the four wells in the dataset with core samples, illustrates the overall siliceous nature of the NE PA Marcellus with high carbonate content only seen in the PCL and USPR* (USPR and USPR_Lm). Figure 25 also illustrates that the UMARC tends to have more clays relative to the LMARC and the USPR*.

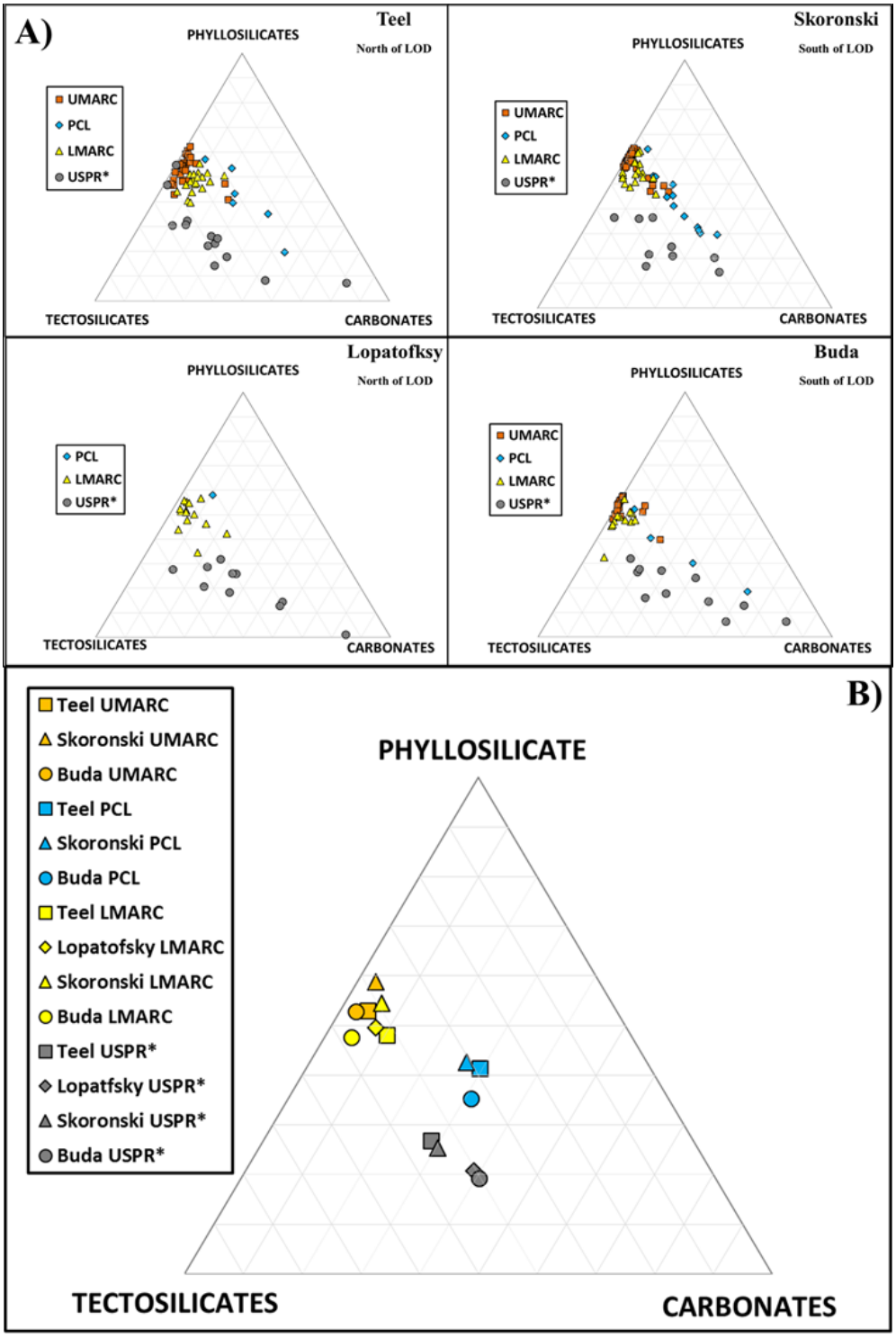

Figure 25: Dataset Composition Comparison. **(A)** XRD Vol% for each member across all four wells with USPR and USPR_Lm combined into USPR*. **(B)** Averaged XRD Vol% for each member across all four wells. All four wells appear comparable, with no massive disparity in composition between the north and south sides of the LOD.

As seen in Table 3, TOC content generally increases in the NE PA Marcellus as you move down section. Table 3 also illustrates that the TOC content within the three members of the NE PA Marcellus does not significantly vary between the north side and south side of the LOD.

Well	Variable	UMARC	LMARC	USPR*
Teel (North of LOD)	Porosity %	7	7	6
	TOC %	6	10	14
Lopatofsky (North of LOD)	Porosity%	N/A	7	7
	TOC %	N/A	10	13
Skoronski (South of LOD)	Porosity %	5	6	4
	TOC %	6	10	11
BUDA (South of LOD)	Porosity %	4	5	3
	TOC %	6	10	12

Table 3: Dataset Average He Porosity% and TOC Vol% by Member. Porosity values are from core He porosity values and TOC Vol% is from LECO TOC normalized with XRD data. The USPR and the USPR_Lm have been combined into USPR*. Lopatofsky did not have a cored UMARC member.

Whereas Table 3 illustrates that TOC content does not materially vary on either side of the LOD, the He Porosity% is notably different between the two sides. For example, an average of all the He Porosity% data in Table 3 bifurcated between north and south (which ignores the inherent differences in the different members) results in a 6.70% for the north and a 4.60% for the south. Thus, on a relative basis, the two wells on the south of the LOD have a 31% lower porosity value than the two wells on the north of the LOD. Or said differently, the two wells on the north of the LOD have a 45% higher porosity value than the two wells on the south of the LOD. Regardless of the calculation methodology, the porosity attributes of wells on the south side of the LOD are markedly

different than those on the north side. This finding is a conundrum because generally there is a correlation between TOC and porosity in unconventional resources (i.e. the higher the TOC the higher the porosity) (Milliken et al., 2013). The TOC/Porosity data used to create Table 3 is graphically demonstrated in Figure 26, which clearly depicts the porosity advantage the north side of the LOD enjoys over the south of the LOD. Is the inferior porosity in wells on the south side of the LOD due to a decrease in interparticle porosity or degradation of organic hosted porosity? Given the similarity in XRD values on either side of the LOD it is unlikely that interparticle porosity is varying significantly, which then logically infers that the organic hosted porosity must be different between the two sides of the LOD. Could the difference in conductivity observed between the north side and the south side of the LOD be connected to the difference in OM porosity? The first step in this thought process is to perform an electric log assessment to better characterize the rock seen across the LOD.

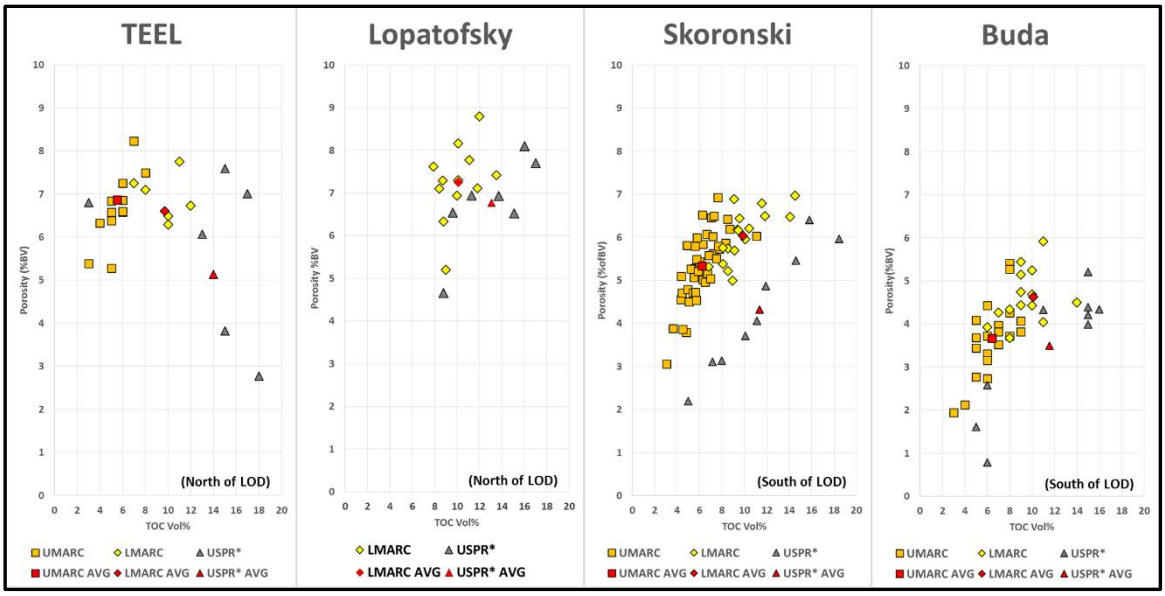

Figure 26: Dataset TOC/Porosity Relationships.

3.2 Electric Log Comparison

The electric logs from the seven wells in the dataset, as depicted in Figure 27, identify the various Marcellus Shale members. Generally, the NE PA Marcellus maintains its thickness as you move south of the LOD. The LMARC and USPR have the highest Gamma Ray (GR) signatures, with the difference between them being attributed to an increase in carbonate content in the USPR. The USPR_Lm also contains carbonate, but is identified by a much lower GR signature.

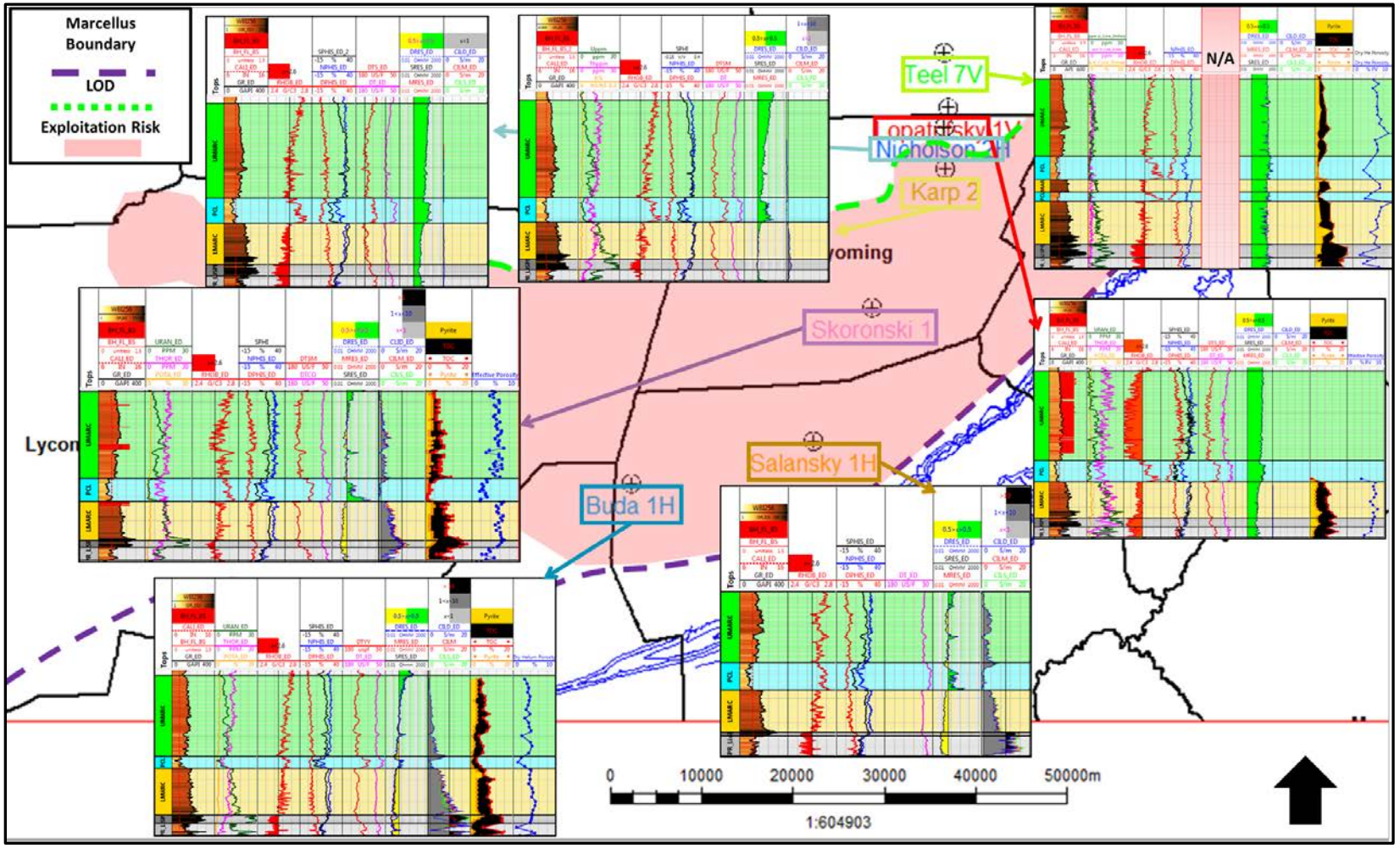

Figure 27: Dataset Log Curves. The tracks, from left to right, are GR, RHOB, Porosity, Sonic, Resistivity, Conductivity, TOC/Pyrite Vol%, and Helium Porosity. Resistivity (Track 6) decreases as you move south, but drops drastically south of Karp 2. Conductivity (Track 7) increases inversely to the resistivity. Only wells with core have TOC/pyrite Vol% and He Porosity%. The Teel exhibits a repeated faulted in LMARC /PCL section.

Figure 28, which was derived from the seven electric well logs, illustrates average Bulk Density, Compressional Slowness, Deep Resistivity and Deep Conductivity for the LMARC and the USPR. A slight increase in average bulk density (RHOB, g/cc3) values in the LMARC can be seen moving south across the LOD with values increasing from 2.57 to 2.64, whereas RHOB in the USPR remains consistently around ~2.50. Average compression slowness values (DTC, us/ft) for both the LMARC and USPR decrease (i.e. the rock is faster) as you move to the south with a decrease of ~13 us/ft for the LMARC and ~7 us/ft for the USPR. Deep resistivity (Ohmm) decreases drastically from 62 to 0.13 in the LMARC and 101.1 to .06 in the USPR as you move south. Deep conductivity (S/m) values increase from 0.02 to 8.19 in the LMARC and from 0.01 to 17.05 in the USPR as you move south.

Given the increases in bulk density and the decreases in compressional slowness that are noted as you move south, it is not surprising that the He Porosity% measurements (see Table 3) are lower south of the LOD in both the LMARC and the USPR. However, the cause of these changes (i.e. bulk density, compressional slowness, and He Porosity %), and the drastic decrease in resistivity seen in the LMARC and USPR as you move south cannot be easily explained. The remainder of this chapter will cover the results related to the investigation of the low resistivity and the porosity degradation seen south of the LOD.

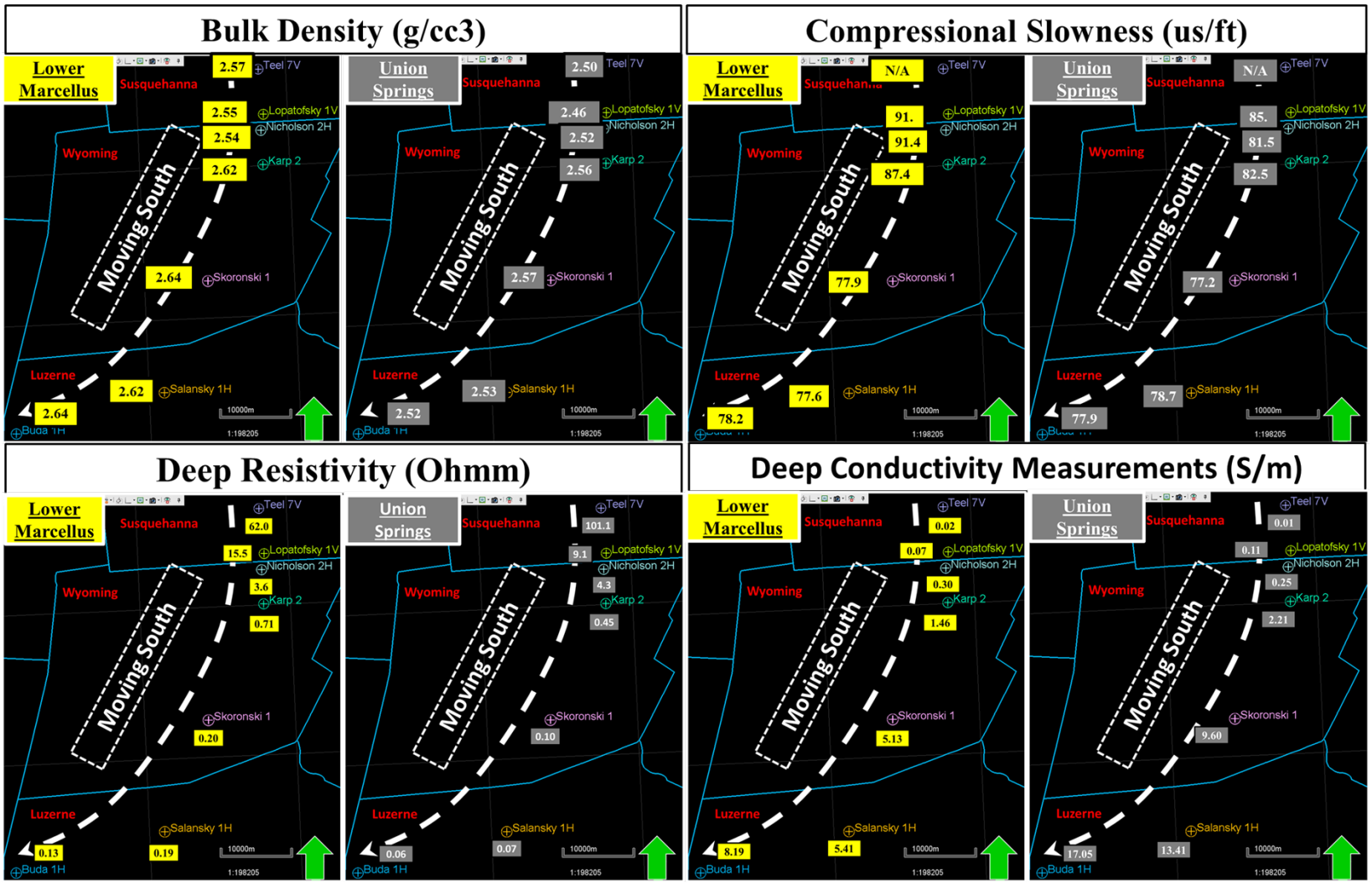

Figure 28: Dataset Log Attributes. Average values of Bulk density (g/cc3), Compressional Slowness (us/ft), Deep Resistivity (Ohmm), and Deep Conductivity (S/m).

3.3 Resistivity Assessment

This section will report the results of the S/TEM EDS imaging, the S/TEM nanometer scale investigation, and the Raman spectra analysis performed on samples from the Teel and the Buda, which act as the book ends of the dataset used in this study.

3.3.1 S/TEM EDS

In mature organic mudrock like that found in NE PA Marcellus there are two distinct populations; OM with pores and normal inclusions, and OM without SEM scale pores with few to no visible inclusions. Accordingly, S/TEM samples from both populations are represented in the samples used in this study.

3.3.1.1 Buda Porous OM and Non-Porous OM

Figure 29 is a 2-micro field of view STEM image of the cross-section of the Buda porous OM sample.

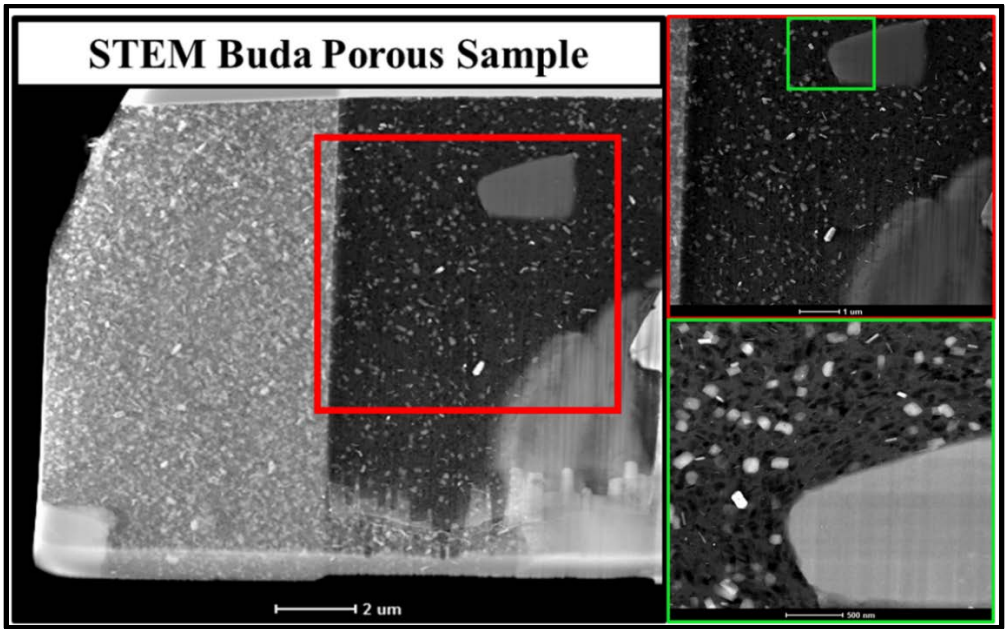

Figure 29: STEM Cross Sectional View of Buda Porous OM at Multiple Magnifications. Inclusions, including one large clast, can be seen throughout the sample.

Inclusions appear evenly spaced throughout the entire Buda porous OM sample. To identify the composition of the OM inclusions, the OM was analyzed with EDS (Figure 30).

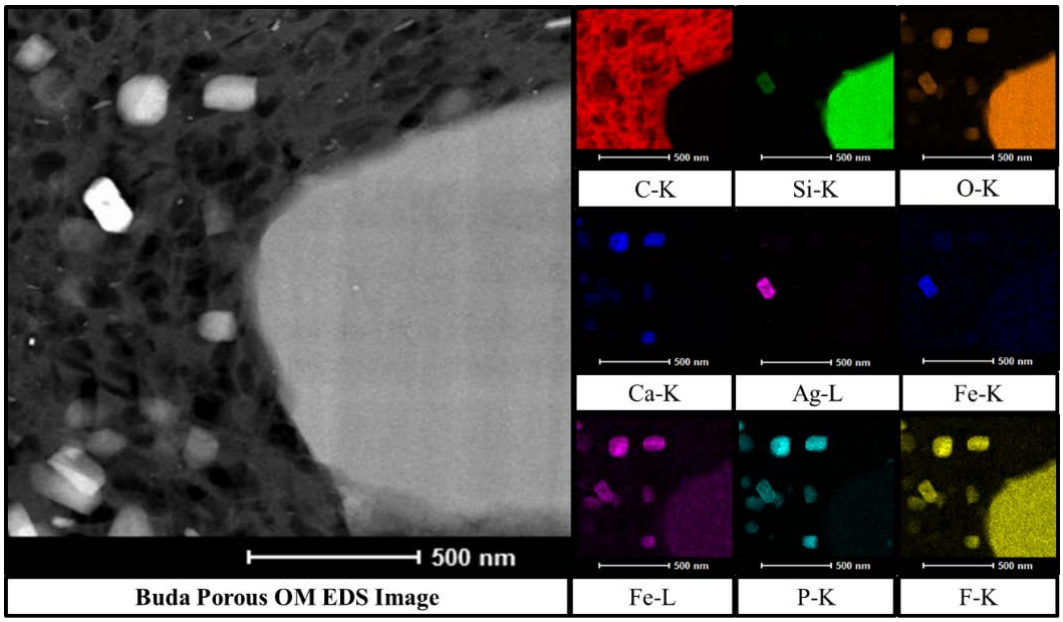

Figure 30: STEM EDS Map of Buda Porous OM.

As expected, carbon, seen in red, represents most of the OM matrix. The large inclusion in the lower right sector of the image is composed of a silicate (SiO_4), as seen by its silica (green) and oxygen (orange) signature and some carbonate material in blue can also be seen to the left of the large silicate inclusion. The most interesting elemental spectra analyzed however is silver (Ag), seen in purple and strongly associated with Fe-K (blue). Silver is the most conductive metal found on earth (Hammond, 2004), and is an interesting discovery given the high conductivity observed in Buda and all areas south of the LOD. Prior to this study, silver had not been documented in Marcellus Shale OM and therefore

had not been considered a possible source of high conductivity south of the LOD. After this discovery, further scouting of the Buda sample was performed and amorphous silver was confirmed to be present evenly throughout the entire sample. Silver was not used in any of the sample preparation, and all possible sources of silver contamination have been eliminated. While the actual minerology cannot be deduced from EDS spectra, it appears that some type of mineral that includes silver is present within the porous Buda OM sample.

Figure 31 shows the STEM cross sectional view of the Buda non-porous OM sample. At 2um field of view inclusions cannot be seen. However, at the nanometer field of view some very small nano-inclusions can be visualized that could not be seen in the initial SEM investigation.

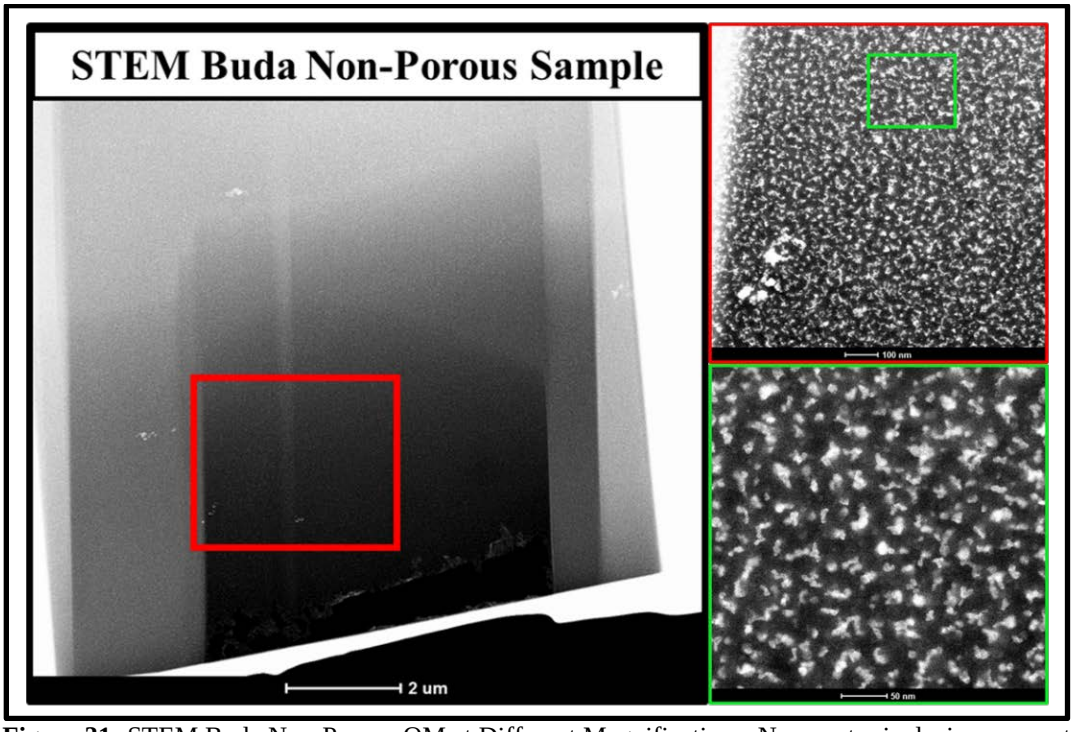

Figure 31: STEM Buda Non-Porous OM at Different Magnifications. Nanometer inclusions are not readily seen at the 2um field of view but become visible at the nanometer field of view.

Figure 32 is the same Buda non-porous OM seen in Figure 31 above, but analyzed with EDS. This procedure was performed to visualize the existence of silver as seen in the porous OM sample.

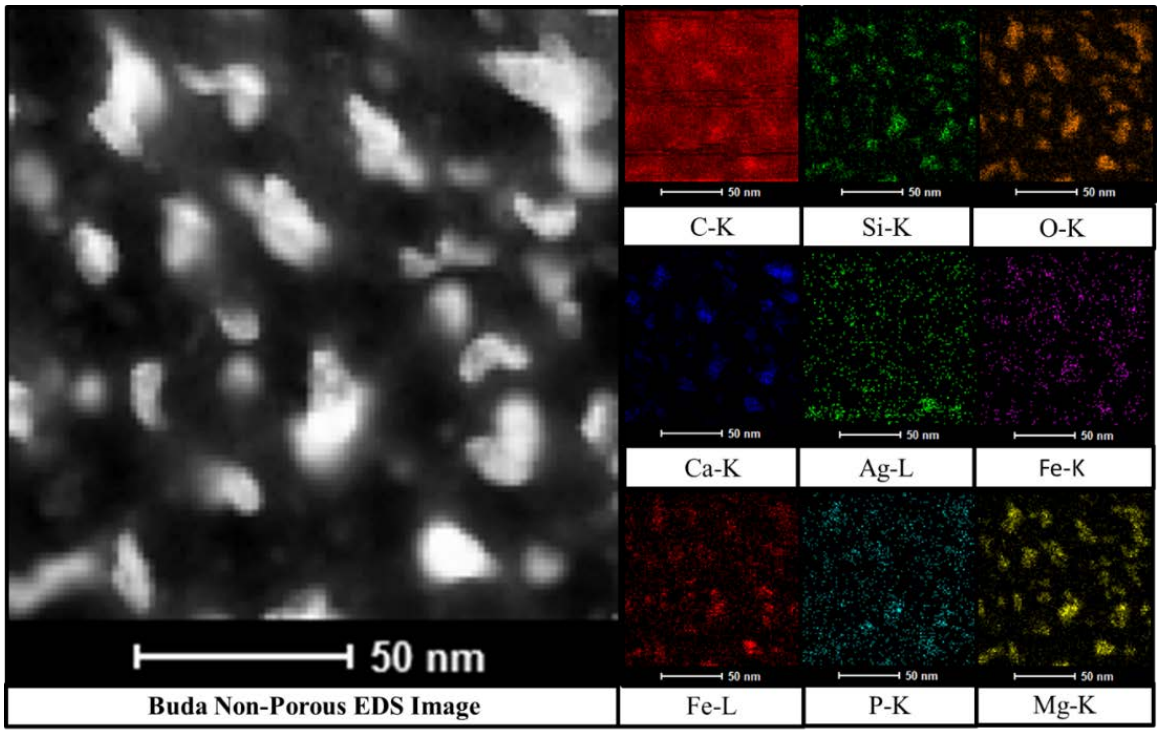

Figure 32: STEM EDS Map of Buda Non-Porous OM.

Carbon, seen in red, comprises most of the OM matrix. Nanometer sized silicate material, represented by silica (green) and oxygen (orange) is peppered throughout the OM along with some carbonate material seen in blue. Consistent with the porous OM sample, silver, this time seen in green, can be seen throughout the non-porous sample with slight association with Fe-L (red). Further scouting was performed on Buda non-porous sample and nano-silver was confirmed to be present evenly throughout the entire sample.

3.3.1.2 Teel Porous OM and Non-Porous OM

Figure 33 shows the STEM cross sectional view of the Teel porous OM sample. Inclusions are evenly spaced throughout the porous OM with a few larger pieces consistent with the Buda porous OM sample.

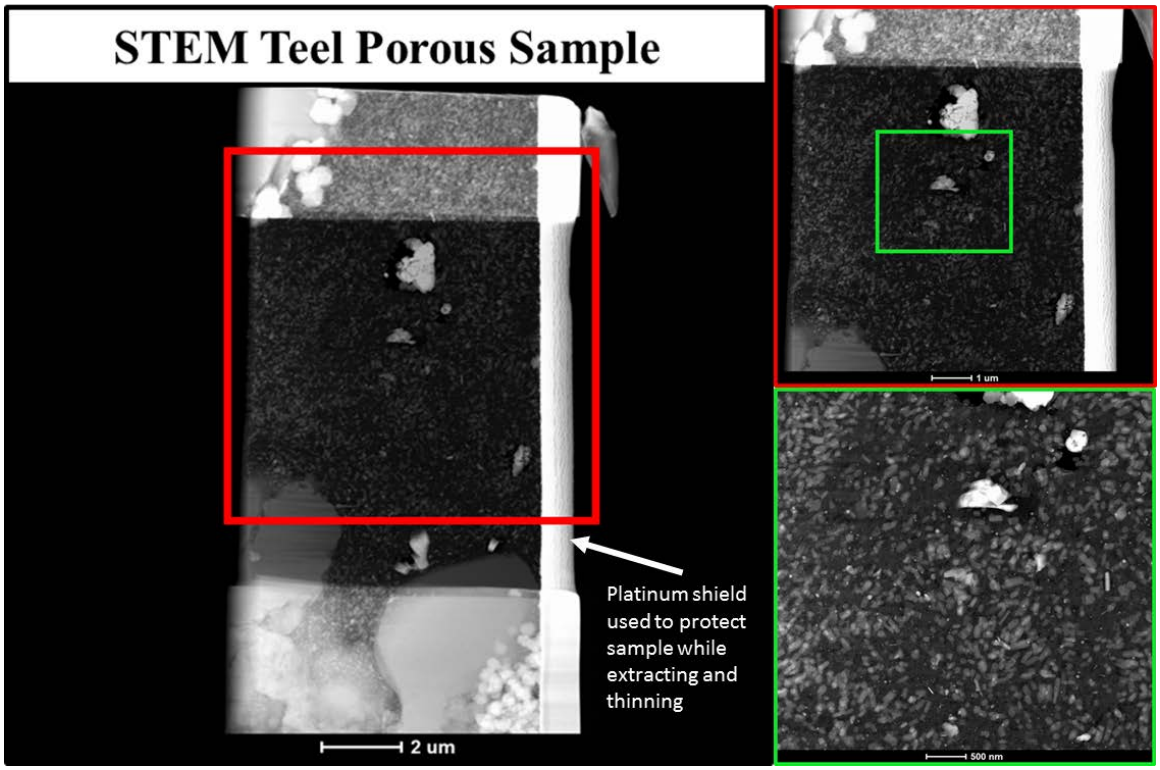

Figure 33: STEM Cross Sectional View of Teel Porous OM at Different Magnifications. Inclusions can be seen throughout the samples with a few larger clasts.

Figure 34 is the same Teel porous OM seen in Figure 33, but analyzed with EDS. Carbon, as seen in red, comprises most of the matrix of the OM, which is also peppered with Silicate material, represented in green and orange, and carbonate material represented in blue. The aluminosilicates, seen in yellow, are likely composed of illite. While silver was

not seen anywhere within the Teel porous sample a good amount of Titanium can be seen, which may be attributed to alteration mineral titanite.

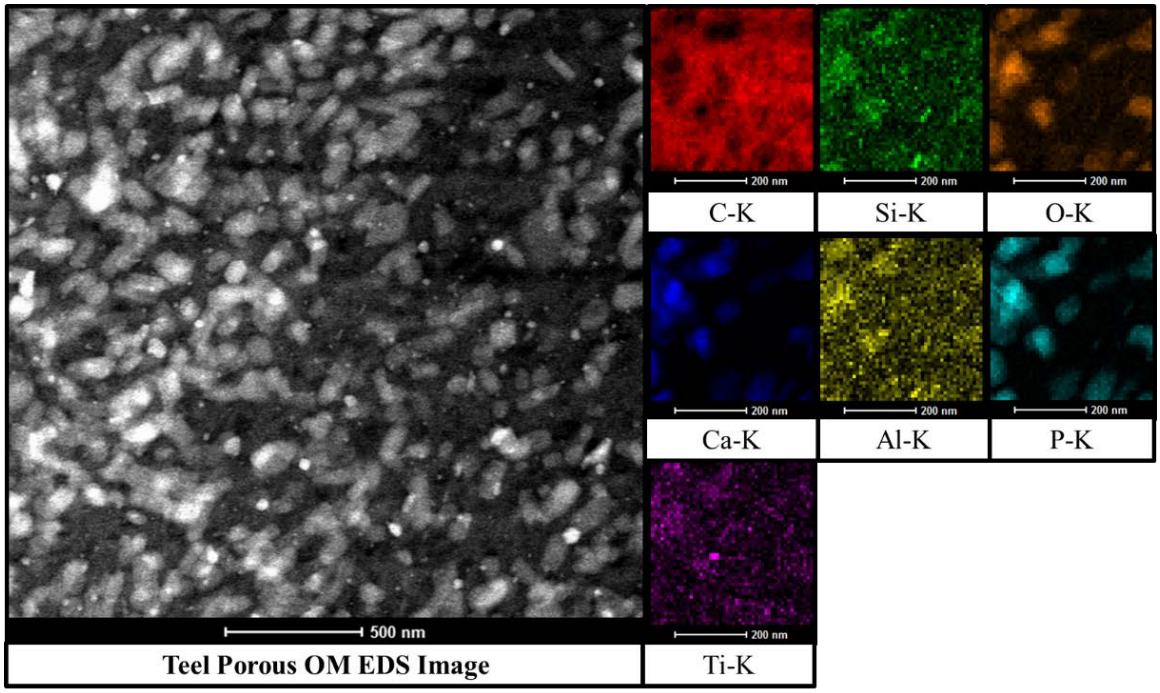

Figure 34: STEM EDS Map of Teel Porous OM.

Figure 35 shows the STEM cross sectional view of the Teel non-porous OM sample. Inclusions are not seen in micron or nanometer field of view.

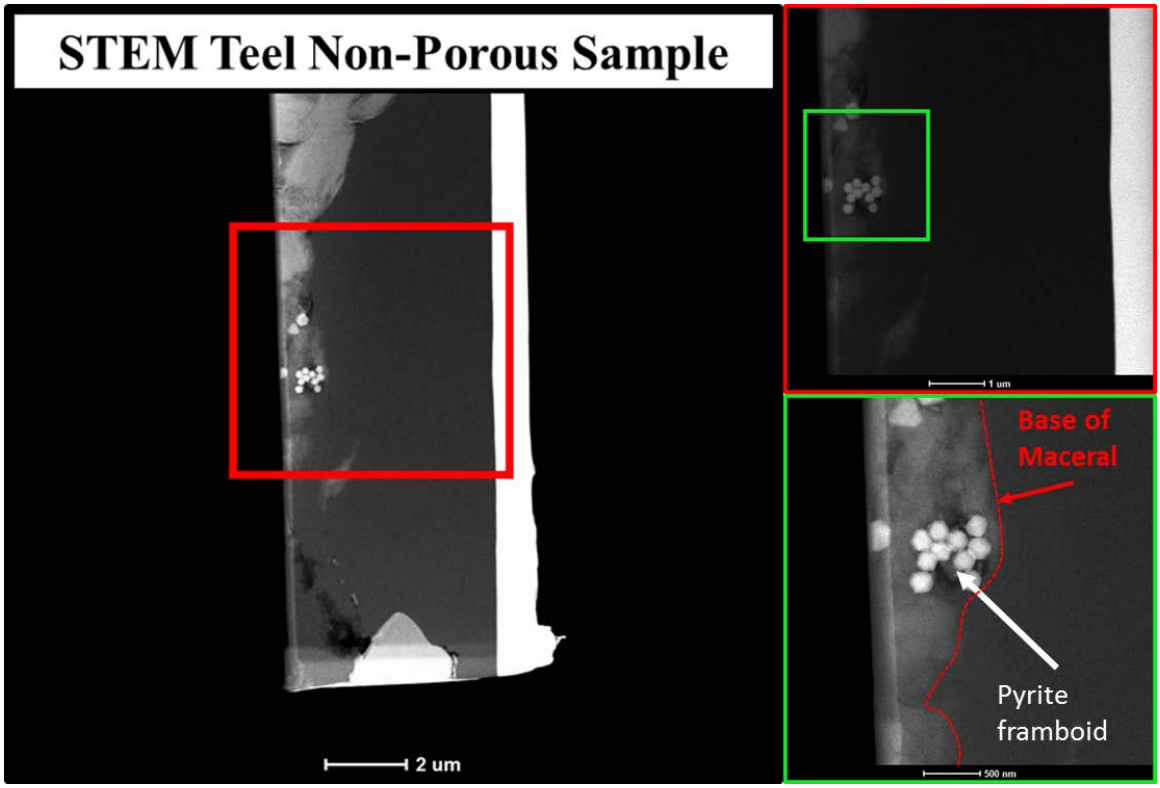

Figure 35: STEM Cross Sectional View of Teel Non-Porous OM. Inclusions cannot be seen in any of the magnifications. The pyrite and other material at the base of the sample are not part of the OM. The platinum shield strip can be seen to the right.

Figure 36 is the same Teel non-porous OM seen previously in Figure 35, but analyzed with EDS. At this scale, no nanometer size inclusions can be seen to the right of the pyrite framboid. Carbon, seen in red, comprises the entire OM matrix to the right of the framboid with no evidence of nanometer inclusions. Pyrite is seen clearly from the iron (orange/red) and sulfur (turquoise) signature and framboidal texture. Aluminosilicate can be seen between the OM and pyrite represented by silica (green), aluminum (yellow) and oxygen (orange). A few pieces of carbonate material can be seen, in purple around the pyrite and clay. Consistent with the EDS of the Teel porous sample, no silver was found in the EDS analysis of the Teel non-porous sample.

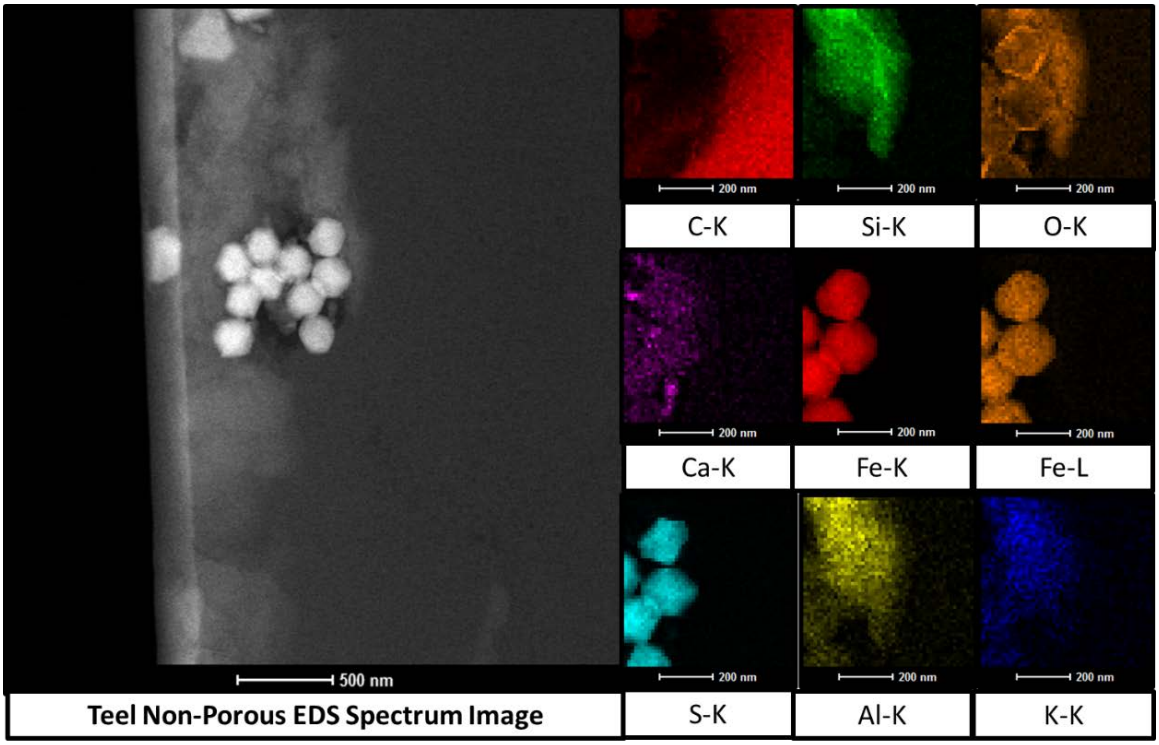

Figure 36: STEM EDS Map of Teel Non-Porous OM.

The original work flow included imaging the S/TEM OM samples with TEM to visualize ordered carbon stacking at the sub nanometer level. Multiple attempts using all samples were made to view atomic carbon ordered stacking with TEM at 300 kV, but the resulting images were inconclusive because carbon alignments, aromatic rings or stacking could not be confirmed. Accordingly, it was determined that sub nanometer investigation using TEM imaging performed at 300 kV was not a viable method to identify increased aromatic carbon structure in this study's OM samples as their highly heterogeneous nature precludes the ability to produce reliable, repeatable imaging.

While the sub nanometer TEM imaging did not successfully identify higher carbon ordered stacking, the discovery of silver in the Buda sample, and the lack of silver in the Teel sample, is a very interesting discovery. While the mere existence of silver alone

cannot explain the high conductivity phenomenon, if the OM hosting this silver is somehow ordered and conductive, the combination of silver within ordered OM needs to be pursued as a potential explanation of the conductivity seen at, and to the south of, the LOD. Raman Spectroscopy was also implemented to build a dataset that would indirectly visualize the atomic structure of the OM to compare carbon ordering on both sides of the LOD.

3.3.2 Raman Spectroscopy

There are distinguishable differences between the Raman spectra of the Teel and Buda at both the LMARC and USPR intervals. The raw spectra can be seen in Figure 37.

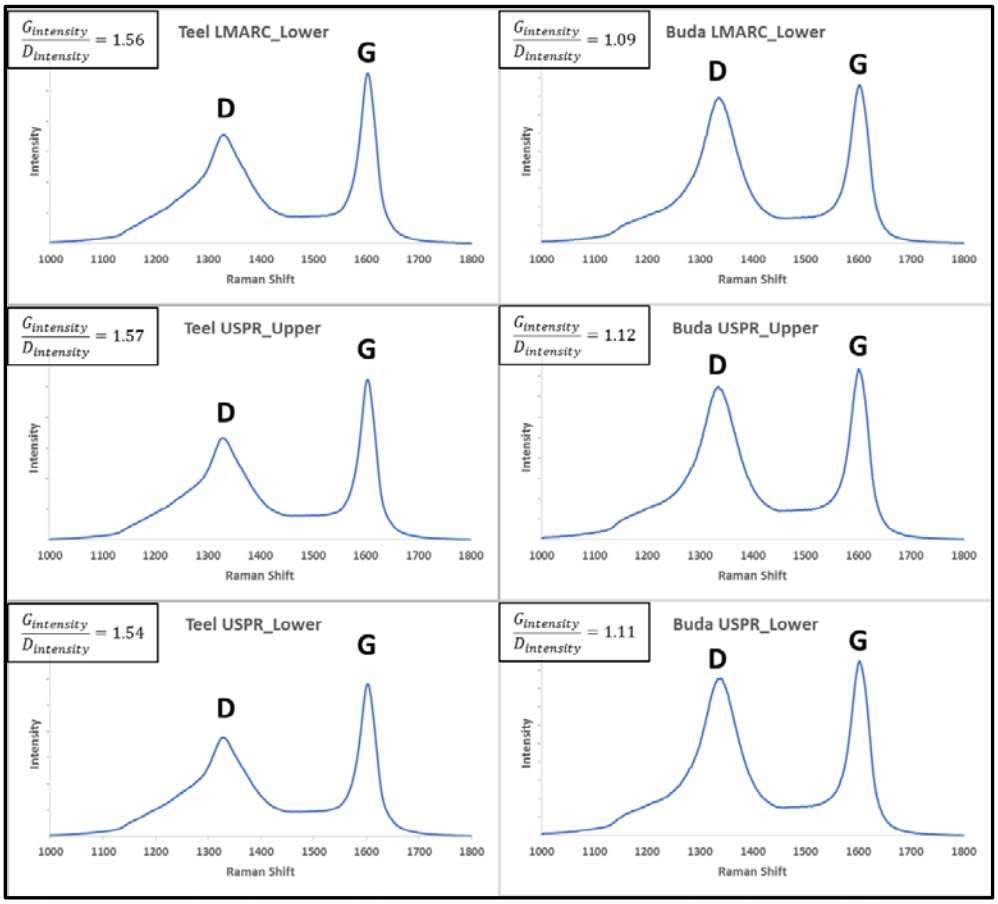

Figure 37: Raw Raman Spectra for Teel and Buda.

While both wells exhibit broad D bands, the Buda's D band intensity is comparable to its G band intensity for all three intervals, whereas the Teel's D band intensity is much lower than its G band intensity for all three intervals (i.e. a G/D intensity ratio greater than 1.5). A high G/D intensity ratio associated with a broad D band is indicative of immature disordered material (Temperatures <300 degrees Celsius), whereas a low G/D intensity ratio associated with a broad D band is indicative of more mature higher ordered material (Temperatures 300-350 degrees Celsius) (Lunsdorf, 2014b) (Figure 15). Based solely on the raw Raman spectra, it appears that the Buda OM is more ordered than the Teel OM. To further compare Raman signatures between the two wells, Raman spectra peak deconvolution was performed.

Raman spectra peak deconvolution, or curve fitting, of high-grade metamorphosed OM is well documented and understood in academia. However, peak deconvolution of low grade and transitional OM material (like that found in the Marcellus Shale) is not as well understood. As a result, several methods of deconvolution and interpretation were considered. The most well-known method of deconvolution was derived by Beyssac (2002) for high-grade sediment. Given that the Marcellus Shale mudrock is not a high-grade sediment, the Beyssac method would appear not to be the best method to use in this study. Regardless, the Beyssac method was applied to samples from the LMARC and USPR members of Teel and Buda to document why the Beyssac method is not suited for these samples. As expected, the Beyssac method did not yield meaningful results in this study's low-grade OM samples. Figure 38 shows the fitted spectra for Teel and Buda using the Beyssac 5 free floating Voigt function peaks, while Table 4 depicts the Beyssac

method R1 and R2 ratios for the Teel and Buda. Per the Beyssac method, R1 and R2 ratios should decrease as OM becomes more ordered. Thus, based on the Beyssac method R1 and R2 ratios it appears that Teel is more ordered than Buda; which is opposite of what is suggested by the raw spectra. Given that the inferences provided from the Beyssac method R1 and R2 ratios are inconsistent with the inferences provided by the broad D band and G/D intensity ratio, it was concluded that the standard Beyssac method should not be used for the samples in this study.

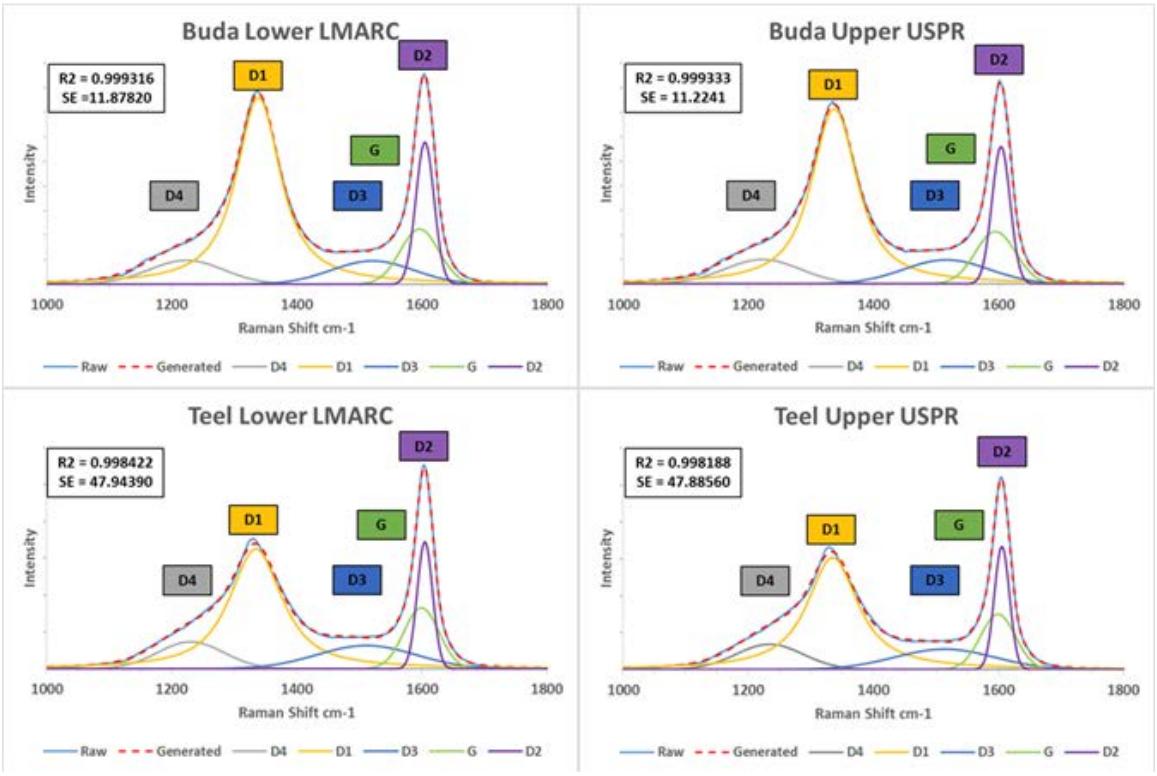

Figure 38: Beyssac Deconvolution for Samples in the LMARC and USPR. The dashed red line represents a summation of the 5 derived fitting bands.

Sample	R1	R2
Teel LMARC_Lower	1.94	0.68
TEEL USPR_Lower	1.99	0.67
BUDA LMARC_Lower	3.38	0.70
BUDA USPR_Lower	3.34	0.70
R1 = (D1/G) R2 = (D1/D1+G+D2) As OM becomes more ordered, R1&R2 decrease		

Table 4: Beyssac Deconvolution Ratios for Samples in the LMARC and USPR.

Because the Beyssac method was determined to be inapplicable, the Lahfid method, which uses five free floating Lorentzian function curves, was used to fit the raw data from Teel and Buda for the LMARC and the USPR members (Lahfid, 2010). The fitted peaks can be seen in Figure 39 and the RA1 and RA2 values are displayed in Table 5.

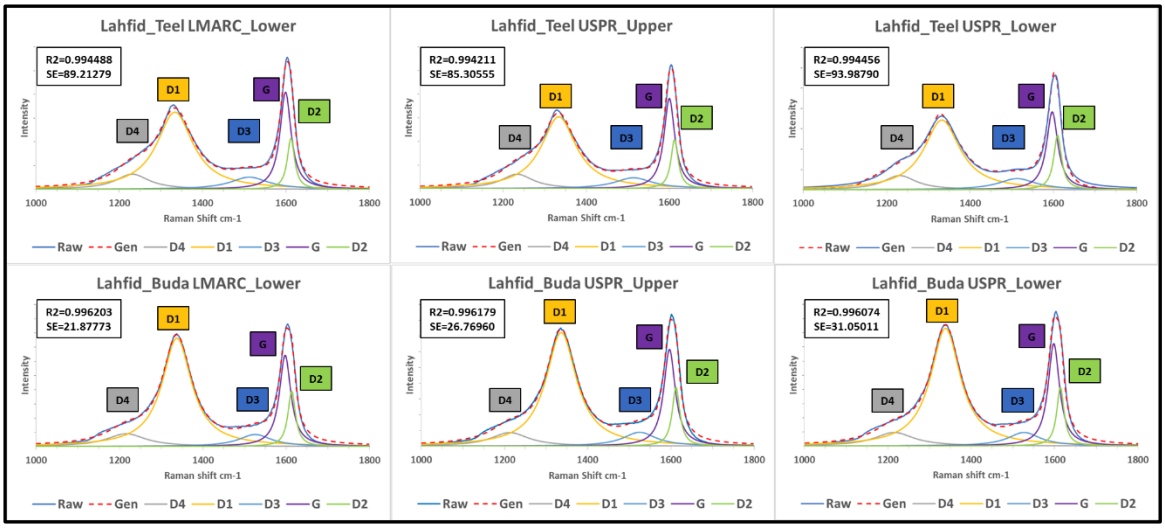

Figure 39: Lahfid Deconvolution for Samples in the LMARC and USPR.

Sample	RA1	RA2	TRA1	TRA2
Teel LMARC_Lower	0.60	1.65	285	307
Teel USPR_Upper	0.60	1.64	284	305
Teel USPR_Lower	0.62	1.64	306	305
Buda LMARC_Lower	0.65	1.91	343	365
Buda USPR_Upper	0.65	1.90	344	362
Buda USPR_Lower	0.65	1.92	340	366
RA1 = (D1+D2)/(D1+D2+D3+D4+G)				
RA2 = (D1+D4)/(D2+D3+G)				
TRA1 = (RA1 - 0.3758)/.0008				
TRA2 = (RA2 -0.27)/.0045				
As OM becomes more ordered, RA1&RA2 increase				

Table 5: Lahfid Deconvolution Ratios for Samples in the LMARC and USPR.

Applying the Lahfid's deconvolution method to the Raman data indicates that Buda is more ordered than Teel across all three intervals. This conclusion is consistent with the fact that the Teel is further north of the coal basin to the south, and has a higher raw spectra G/D intensity ratio. A further comparison between the two wells can be made in terms of temperature. TRA1 and TRA2 were derived from Lahfid's linear regression equations of temperature (derived from vitrinite reflectance, illite crystallinity, or fluid inclusions from his samples in the Helvetic zone of the Glarus Alps) cross plotted against RA1 and RA2 Raman parameters. Using Lahfid's equations, the Buda temperature range is ~340 to 366 Celsius and the Teel temperature range is ~284 to 307 Celsius, which places the Buda within the transitional carbon phase and the Teel within a lower-grade amorphous phase. While Lahfid's method of deconvolution concludes that the Buda is more ordered than the Teel, which is consistent with the raw spectra G/D ratio interpretation, the Lahfid method still contains ambiguity in regard to the fitting of the G and D2 peaks (Figure 39) in that the size and position of these peaks infer attributes to the rock that appear contrary to physical reality. For example, the fitted peaks for the Teel under the Lahfid method include

a substantial G peak (representing graphic structure) that is already more intense than the D2 peak (representing non-graphic structure) even though the Lahfid method assigns a temperature range to the Teel that is consistent with lower-grade amorphous material. Given that it is very unlikely that such low-grade material would have such an intense G band so early in its graphitization evolution, there is still something askew with the fitting method of these low-grade rocks. To improve the interpretation of low-grade OM, the Kouketsu method was also implemented.

To address the problem noted by Beyssac regarding unresolvable D2 bands in poorly ordered OM (see Section 2.3.3), which is illustrated in the results of applying the Lahfid method described in the preceding paragraph, Kouketsu (2013) introduced a fixed parameter that eliminates the G peak in any spectra with a raw $G_{intensity}/D_{intensity} > 1.5$. Kouketsu reasoned that any spectra with such a high $G_{intensity}/D_{intensity}$ should not have interpretable amounts of graphic structure and the inclusion of a G band would hinder meaningful deconvolution of this lower-grade disordered OM spectra. For more explanation, see the appendix to Kouketsu (2013). The summary of the Kouketsu method previously provided in Figure 15 is repeated here as Figure 40. Note that the existence of a D4 band in both the Teel and Buda forces these samples to the left side of the Kouketsu work flow. Also note that the raw spectra for Teel and Buda from Figure 37 resemble the low to medium grade spectra from the Kouketsu method in Figure 40, with the Teel corresponding to Kouketsu's samples Kr6 and NB02 and with the Buda corresponding to Kouketsu's sample RS9.

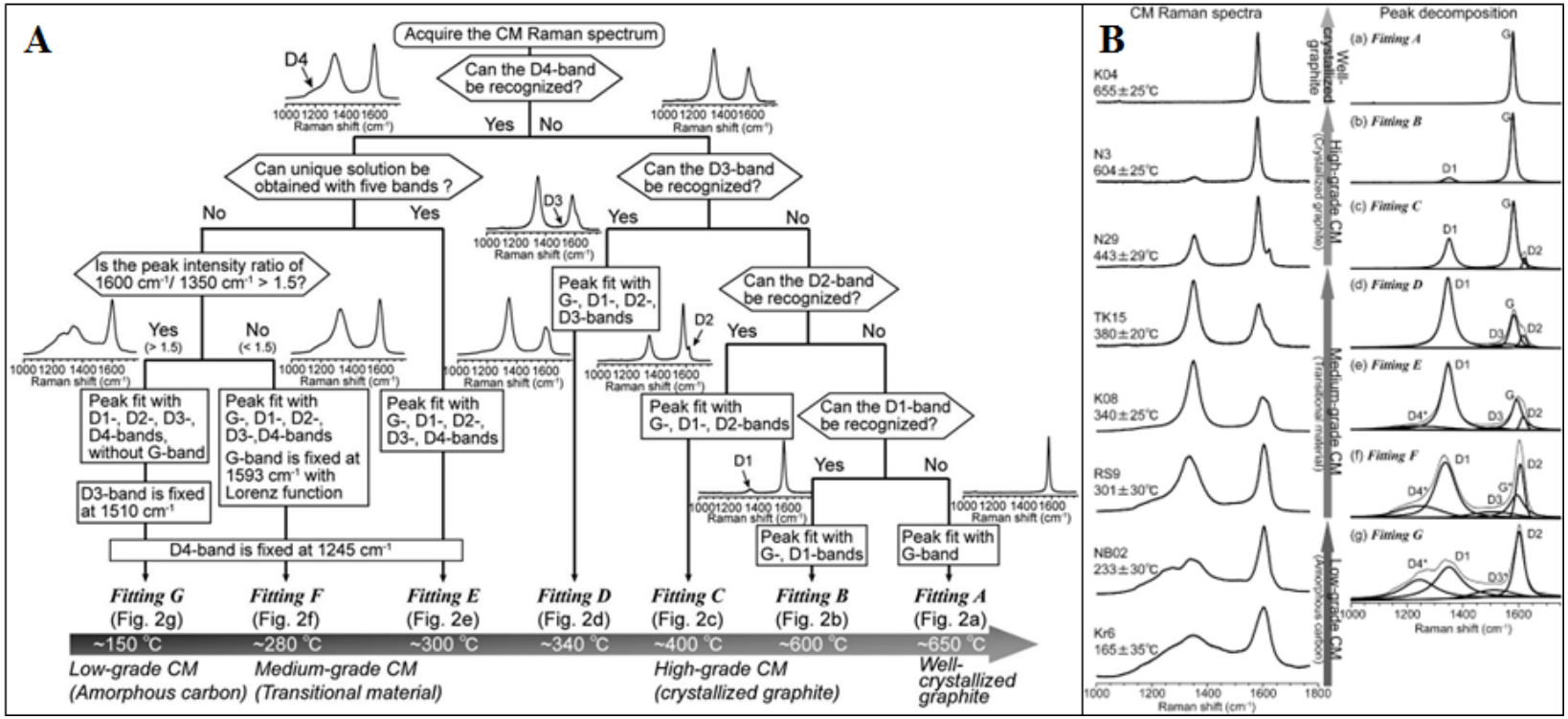

Figure 40: Summary of the Kouketsu Deconvolution Method. **(A)** Flowchart of the seven peak fitting procedures used by Kouketsu **(B)** OM Raman spectra for several representative samples and their corresponding Kouketsu Method peak fittings. Asterisks in the band name in (e) to (g) signify that the center position of that band was fixed by a Kouketsu Method parameter.

Figure 41 displays the fitted peaks that result from the Kouketsu (2013) methodalogy, with the Teel deconvultion lacking the G band and Buda deconvulution including the G band based upon their respective raw $G_{intensity}/D_{intensity}$ ratios. The various values associated with the Kouketsu method are displayed in Table 6.

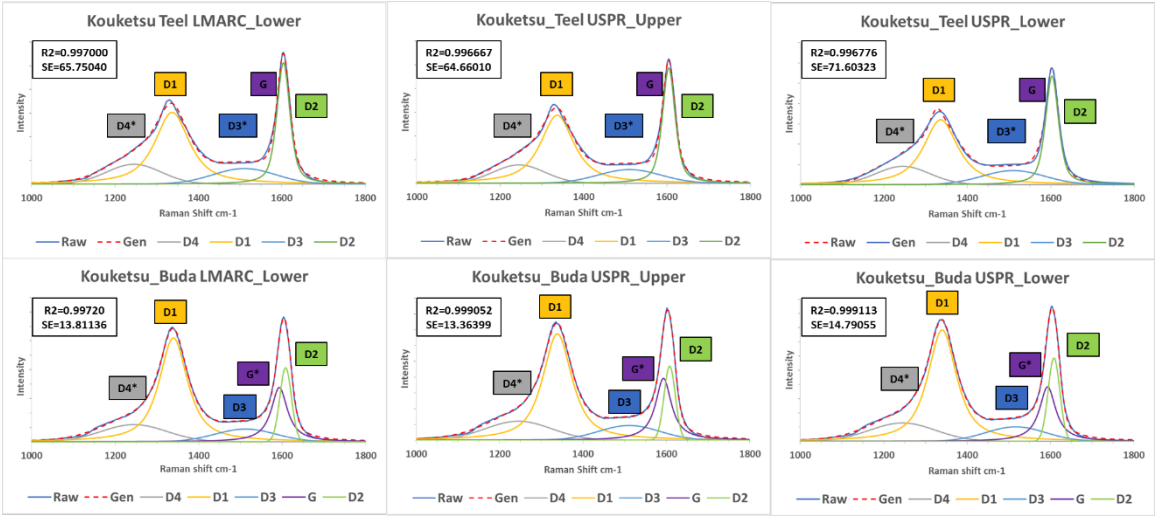

Figure 41: Kouketsu Deconvolution for Samples in the LMARC and USPR. Bands marked with * are those that are fixed by a Kouketsu method parameter.

Sample	D1 Center	D1 FWHM	D2 Center	D2 FWHM	D2/D1 Intensity	Temperature (D1 FWHM)	Temperature (D2 FWHM)
Teel LMARC_Lower	1336.8	98.3	1603.6	36.8	1.69	267	285
Teel USPR_Upper	1336.7	95.4	1604.3	35.9	1.69	273	292
Teel USPR_Lower	1335.8	97.3	1602.8	37.1	1.67	269	283
Buda LMARC_Lower	1339.2	80.5	1608.0	32.7	0.71	305	313
Buda USPR_Upper	1338.4	83.1	1607.8	31.9	0.70	299	319
Buda USPR_Lower	1340.1	82.1	1608.2	33.1	0.75	302	310
As the OM becomes more ordered D1 FWHM decreaes , D2 center shifts right, D2 FWHM decreases, D2/1 intensity decreases TD1 = -2.15*(D1 FWHM) + 478; (R2 = 0.970) TD2 = -6.78*(D2 FWHM) + 535; (R2 = 0.968)							

Table 6: Kouketsu Deconvolution Values for Samples in the LMARC and USPR. T_{D1} is the temperature derived from D1 FWHM Temperature regression equation. T_{D2} is the temperature derived from the D2 FWHM temperature regression equation

The results of the Kouketsu method indicate an increase in OM ordering from the Teel to the Buda within all key parameters (D1 FWHM, D2 Center, D2 FWHM, and D2/D1). D1 FWHM decreases, D2 center shifts right, D2 FWHM decreases, D2/D1 intensity decreases. There are some important differences between the Lahfid method and the Kouketsu method. Under the Kouketsu method the Teel does not have an interpretable G band and its D2 band is more intense, while the Buda has a smaller interpretable G band and a less intense D2 band. As OM matures and begins to become more ordered the G band should intensify and shift left while the D2 band continues to decrease and shift right. Thus, the parameters within the Kouketsu method aimed at low-grade material allow the Kouketsu method to avoid the ambiguity created by the Lahfid method, and results in an interpretation of these lower maturity OM samples that is more consistent with the overall evolution of the OM spectra demonstrated in Figure 15.

A further comparison between the two wells can be made in terms of temperature. TD1 and TD2 were derived from Kouketsu's linear regression equations of temperature (derived from vitrinite reflectance, illite crystallinity, mineral assemblage, or thermal modeling from his samples in southwest Japan) cross plotted against D1 FWHM and D2 FWHM parameters. Using Kouketsu’s equations, the Buda temperature range is ~299-319 degrees Celsius and the Teel temperature range is ~267-292 degrees Celsius. An application of the temperature scale included in Figure 39 puts the Buda squarely within the medium-grade transitional category while the mid-point of the Teel range puts it at the top of the low-grade amorphous category, but very close to the medium-grade transitional category.

In Summary, both the Lahfid method and the Kouketsu method indicate that Buda is higher ordered than the Teel, and that Buda's OM spectra is consistent with medium-grade transitional material while Teel's OM is more consistent with lower-grade amorphous material. Given that conductivity is positively correlated with carbon ordering (Chung, 2002), this Raman analysis creates a reputable presumption that the resistivity on the south side of the LOD should be lower than the north side of the LOD. Further, given that the Teel is considered an amorphous material and the Buda is considered only a transitional material, it is not surprising that graphite was not confirmed by the samples in this study (or in the Weatherford work) because the OM has not entered crystalline graphitic phase. The next step is to correlate this higher level of ordering seen across the LOD with a possible decrease in OM hosted porosity across the LOD.

3.4 Reservoir Quality Assessment

This section will present the results from large scale SEM mosaic segmentation and N_2 Adsorption of the LMARC and UPRS members of the Teel and Buda, which act as the end members of the dataset used in this study.

3.4.1 Average SEM OM and Pore Segmentation Data

The SEM segmentation analysis in this study sought to take a non-biased sample of the rock and measure a broad range of OM sizes so that the derived distributions and geometric values would be scalable to other analyses, such as nitrogen adsorption. One method to assure that the samples properly represent the underlying rock is to compare the AVG SEM TOC % values to the TOC Vol% values derived from traditional LECO TOC wt% integrated with XRD wt%. As illustrated in Table 7, the samples used in this research

have very comparable values, except for the Teel 7005' which is likely due to OM distribution anisotropy in that sample.

Sample	Formation	TOC Data	
		TOC Vol%	AVG SEM TOC%
Teel 6973'	LMARC_L	12%	10.10%
Buda 7910'		11%	10.39%
Teel 7005'	USPR	16%	22.05%
Buda 7933'		13%	13.75%

Table 7: Comparison of TOC Vol% to Average Mosaicked SEM TOC%.

Table 8 shows He Porosity% and porosity values derived from SEM pore segmentation. While the AVG SEM Porosity% values are not comparable to the He Porosity% values, the SEM Large OM Porosity% values (taken from mosaic of locally segmented OM) demonstrate porosity values much closer to He Porosity%. Figure (42) includes images of the four mosaics whose large OM were locally segmented.

Sample	Formation	Porosity Data		
		He Porosity%	AVG SEM Porosity%	SEM Large OM Porosity%
Teel 6973'	LMARC_L	6.70%	0.90%	6.22%
Buda 7910'		5.90%	1.13%	3.71%
Teel 7005'	USPR	2.80%	0.56%	1.28%
Buda 7933'		6.00%	0.81%	3.77%

Table 8: Comparison of He Porosity % to SEM Derived Porosity Values.

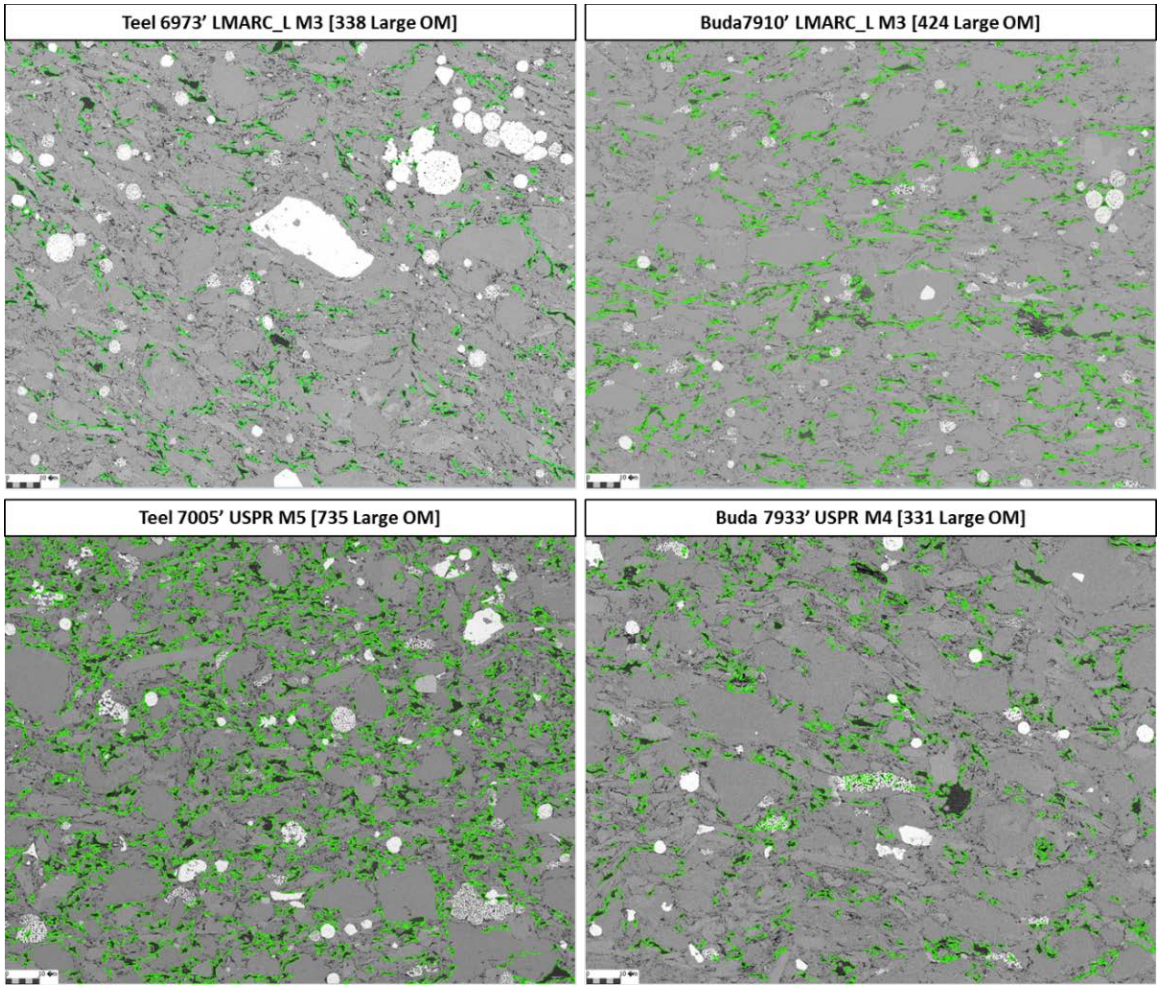

Figure 42: Large OM Porosity SEM Images of LMARC and USPR Mosaics.

3.4.2 Local OM Hosted Pore Segmentation

As mentioned in Section 3.1, to understand why the normal correlation between TOC and porosity is not seen south of the LOD it is important to analyze PSDs. The following section will display the results of the local large OM segmentation in the LMARC and USPR in both the Teel and Buda.

3.4.2.1 Lower Marcellus

The large OM local segmentation data from the Lower Marcellus for both Teel and Buda can be seen in Figure 43. Each graph in this figure clearly confirms the 20nm

resolvable limit. Regardless of the resolvable limit issue, the pore frequency graphs of the two wells are nearly identical, while the pore surface area trends are similar. The Buda has 25% more large OM objects locally segmented than the Teel, while Buda's SEM TOC% is 19% higher than the Teel. Whereas the Teel's He Porosity is 13% higher than the Buda, the Teel's cumulative pore area of 59 um2 is 31% higher than the Buda's cumulative pore area of 45 um2. The comparison of the two well's pore size contributions within the sampled interval (20-400nm), indicates the Buda has a higher meso pore contribution and a lower macro pore contribution. This data does not provide enough evidence to evaluate a PSD shift to larger pore values because the resolvable limit issue precludes the recognition of all the micropores and the smaller portion of the mesopores.

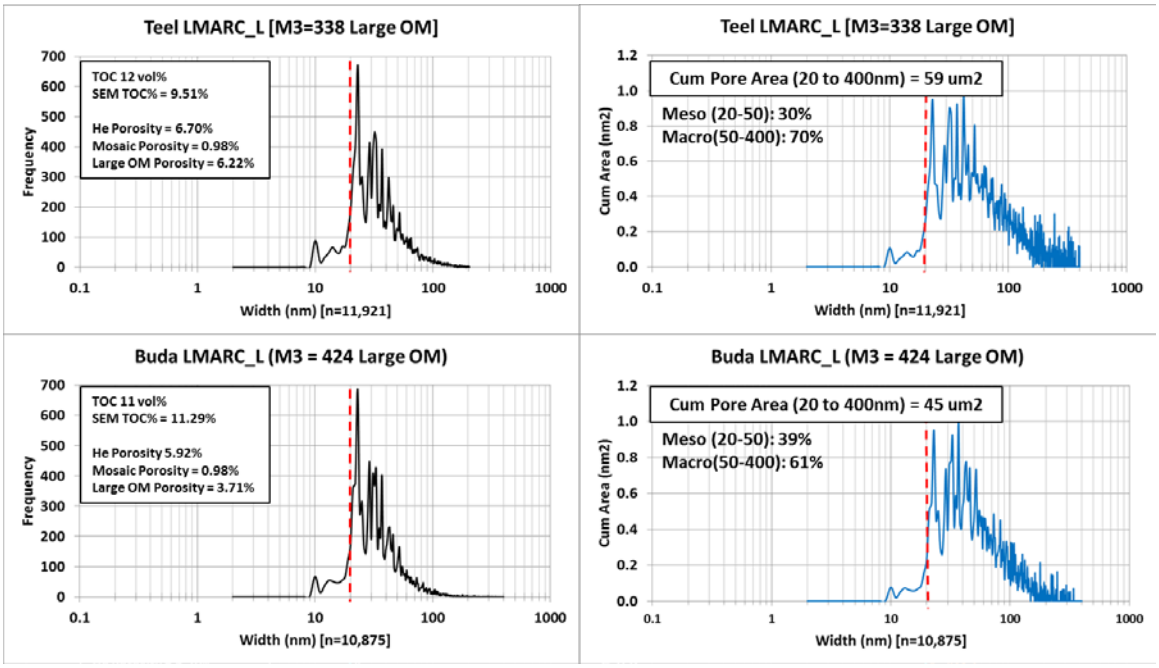

Figure 43: Porosity Distributions and Cumulative Pore Area for Samples in the Lower LMARC. Red line indicates resolvable limit of the SEM technique implemented.

3.4.2.2 Union Springs

The large OM local segmentation data from the USPR for both Teel and Buda can be seen in Figure 44. Each graph in this figure clearly confirms the 20nm resolvable limit. Regardless of the resolvable limit issue, the pore frequency graphs of the two wells are nearly identical, while the pore surface area trends are similar. There is a material difference between the number of large OM objects between Teel and Buda, with the Teel having 122% more large OM objects locally segmented. Correspondingly, the SEM TOC% value for the Teel is 57% higher than the Buda. Despite having much fewer large OM objects, the Buda has a slightly higher cumulative pore surface area than the Teel, even though Buda's He Porosity% value is 113% higher than the Teel. Within the sampled interval (20-400nm), the Buda has a lower meso pore contribution and a higher macro contribution than the Teel. The sampled pore intervals are not wide enough to conclude whether this clear evidence that the PSD is shifting to larger pore sizes.

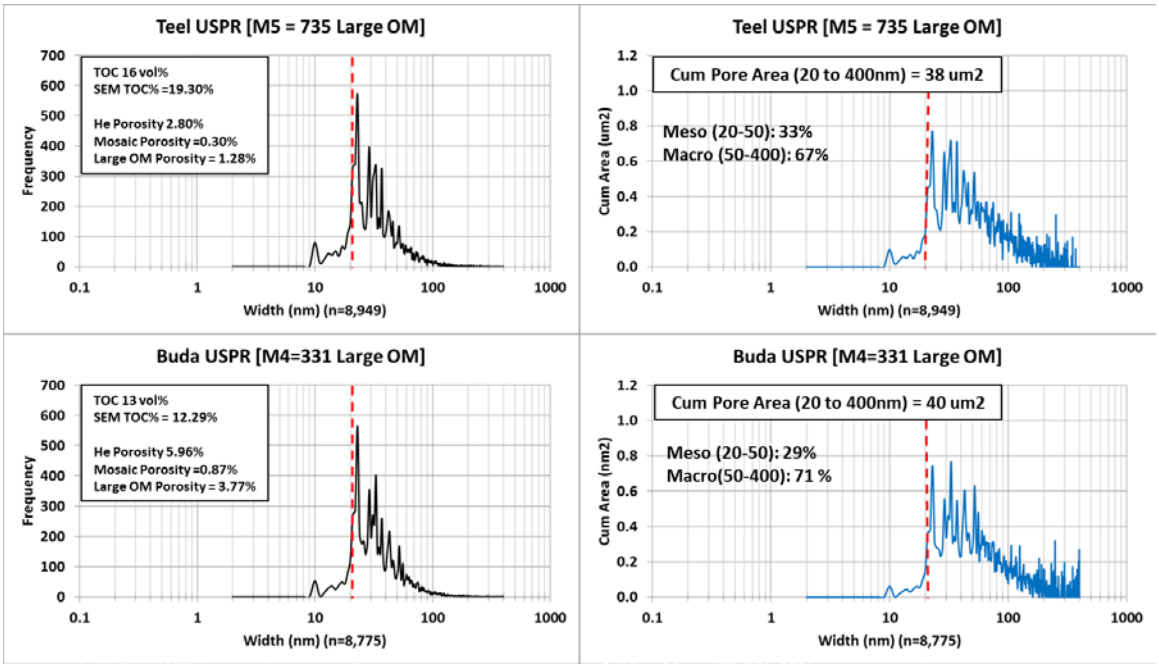

Figure 44: Porosity Distributions and Cumulative Pore Area for Samples in the USPR. Red line indicates resolvable limit of the SEM technique implemented.

3.4.3 Global Pore Segmentation

The large local OM segmentation does not have a consistent basis to compare the two wells because of the small sample size (i.e. one mosaic per interval) and the fact that only large OM pores where extracted. Below are the results of the global pore segmentation from all 20 mosaics (five per well at both the LMARC and USPR). This larger sample size should create a better basis from which the two wells can be compared.

3.4.3.1 Lower Marcellus

Figure 45 depicts all pores segmented across all five LMARC mosaics from the Teel and Buda. The pie charts depict the distribution of each well's OM object size by three categories; large (> 1um2) medium (1-0.20 um2), and small (0.20-0.02 um2). The OM size distribution is very similar between the two wells.

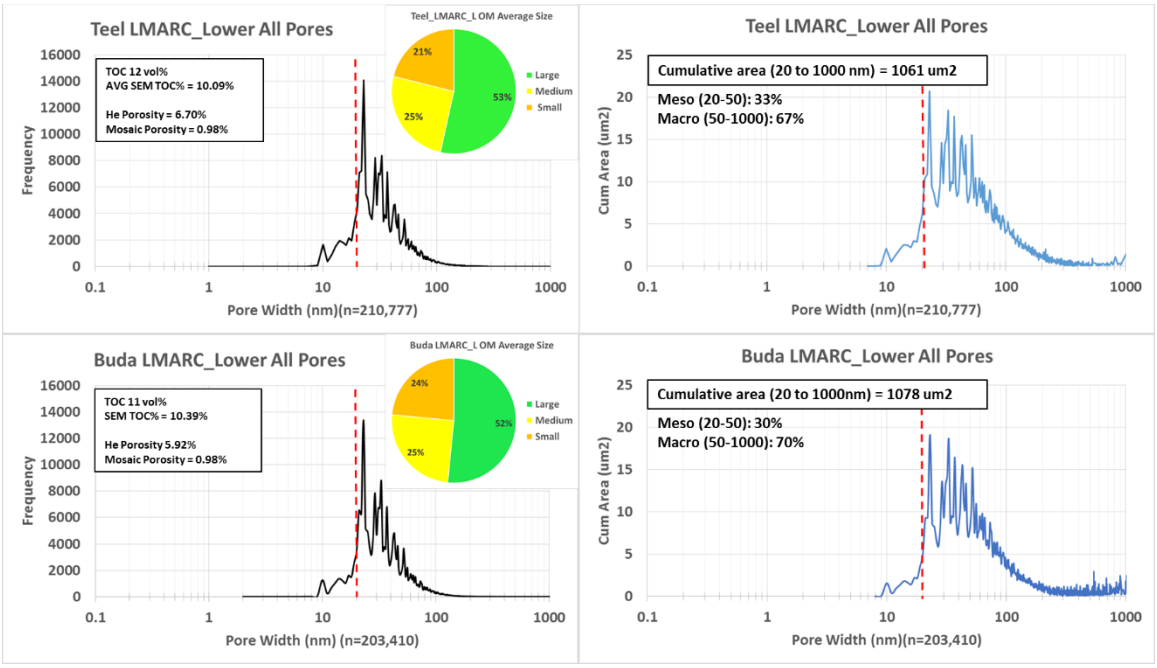

Figure 45: Averaged Global Pore Segmentation Data for Samples in the LMARC.

There are several notable differences between the local large OM segmentation data reported in Section 3.4.2 and this global pore segmentation data. For example, whereas the Teel had the higher cumulative pore surface area in the large OM segmentation data, the global segmentation data indicates that Buda has the higher cumulative pore surface area despite maintaining lower He Porosity% measurements, which infers that the Teel's higher He Porosity% must be contributed by pore sizes outside the bounds of 20-400nm. Another notable difference between the two sources of segmentation data relates to pore size composition. In the large OM segmentation data, the Teel has a higher percentage of macropores, while the global segmentation data shows that the Buda has a higher percentage of macropores. In other words, the Buda demonstrates a higher proportion of macropores within the observed range of 20-400nm.

3.4.3.2 Union Springs

Figure 46 depicts all pores segmented across all five USPR mosaics from both Teel and Buda. The USPR samples for both wells have relatively more large-OM (>1um2) than demonstrated by the LMARC data shown in Figure 45. More notable, is the significantly larger number of large OM (> 1um2) seen in the Teel USPR compared to the Buda USPR, which corresponds with the Teel's much higher SEM TOC% value.

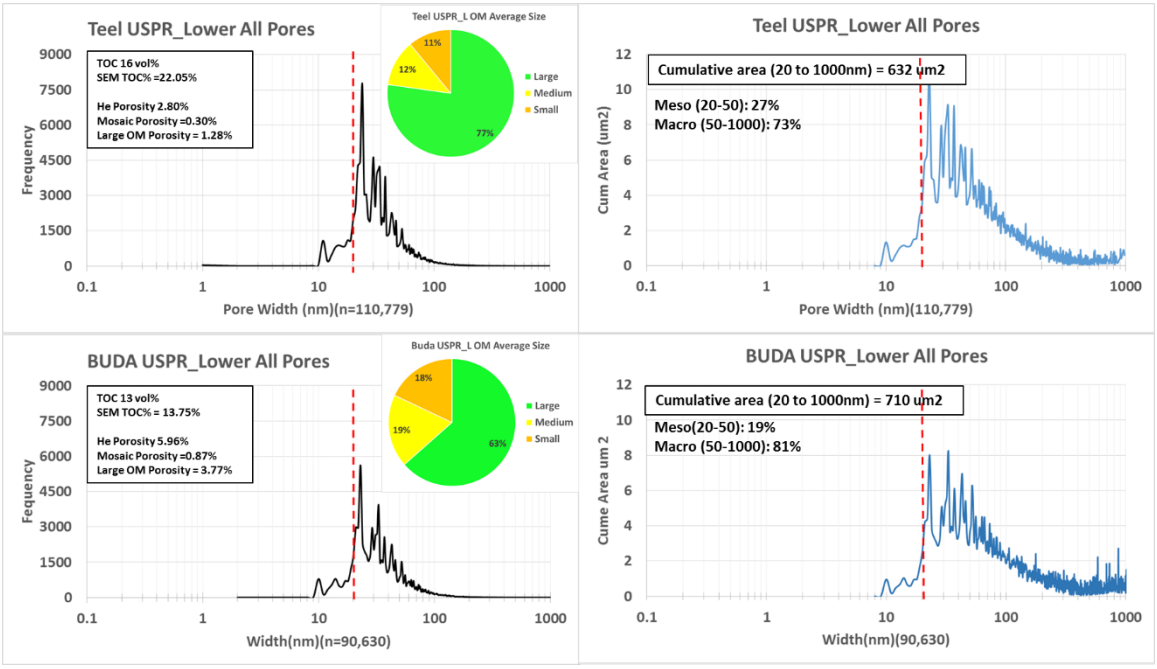

Figure 46: Averaged Global Pore Segmentation Data for Samples in the USPR.

Whereas a comparison between the large OM segmentation data and the global segmentation data for the LMASC yielded several notable differences, the USPR data between the two sources are relatively comparable. Buda has the larger cumulative pore surface area in both segmentation data sources, which corresponds with its higher He Porosity% value. The pore size contribution is also consistent between the two data

sources, with the Buda having a larger surface area contribution from macropores (i.e. on average for the given PSD of 20-400nm the Buda has more macropores).

Although the globally segmented pores allowed for a larger sample of data, it lacks data pertaining to the lower mesopores and micropores, which are a very large compartment of an organic rich mudrocks capacity to hold gas. To further investigate the difference between the two wells, the contribution of the smaller pore ranges below 20nm was examined with N_2 adsorption.

3.4.4 N_2 Adsorption

To better understand the PSDs and the different area and volumetric contributions of different pore sizes across the LOD, especially in the lower mesopore and micropore ranges, N_2 adsorption was performed on the Lower Marcellus and Union Springs intervals using the four samples described in Section 3.4.1, with two additional samples (one apiece from the Teel and the Buda) from the upper USPR.

3.4.4.1 Lower Marcellus

Figure 47 contains the incremental pore area and incremental pore volume of the LMARC_L interval for both the Teel and Buda.

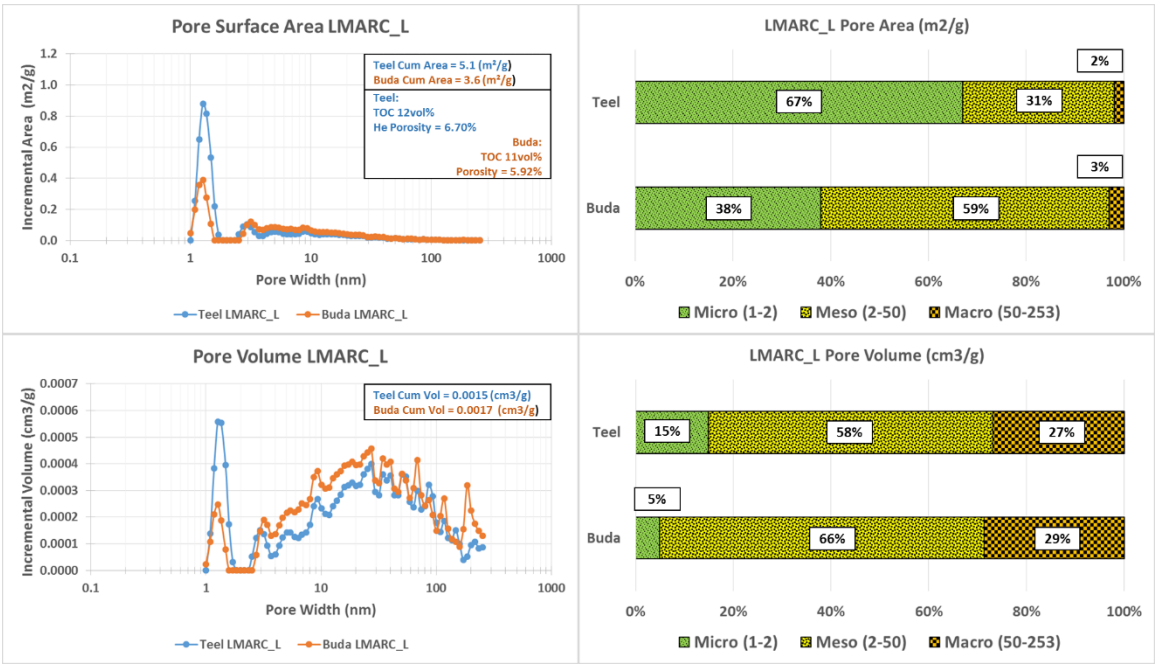

Figure 47: N_2 Absorption Pore Surface Area and Volume for Samples in the LMARC.

It is clear from the graphs in Figure 47 that the Teel has more incremental area and volume contributed from micro pore sizes 1-2nm relative to the Buda, whereas the Buda has more incremental area and volume contribution from the meso (2-50) and macro (>50) pore sizes relative to the Teel. Due to the large difference in area allotment coming from the micropore level, the Teel's cumulative pore surface area of 5.1 m3/g is 42% higher than the Buda's 3.6 m2/g cumulative pore surface area. The difference between the well's cumulative pore surface area is directionally consistent with their He Porosity% values, where the Teel has a 13% advantage. Even though the Teel has a much larger contribution from the micropore range, the Buda enjoys a slightly higher cumulative pore volume value.

3.4.4.2 Union Springs

Figure 48 contains the incremental pore area and incremental pore volume of the Upper USPR interval for both the Teel and Buda.

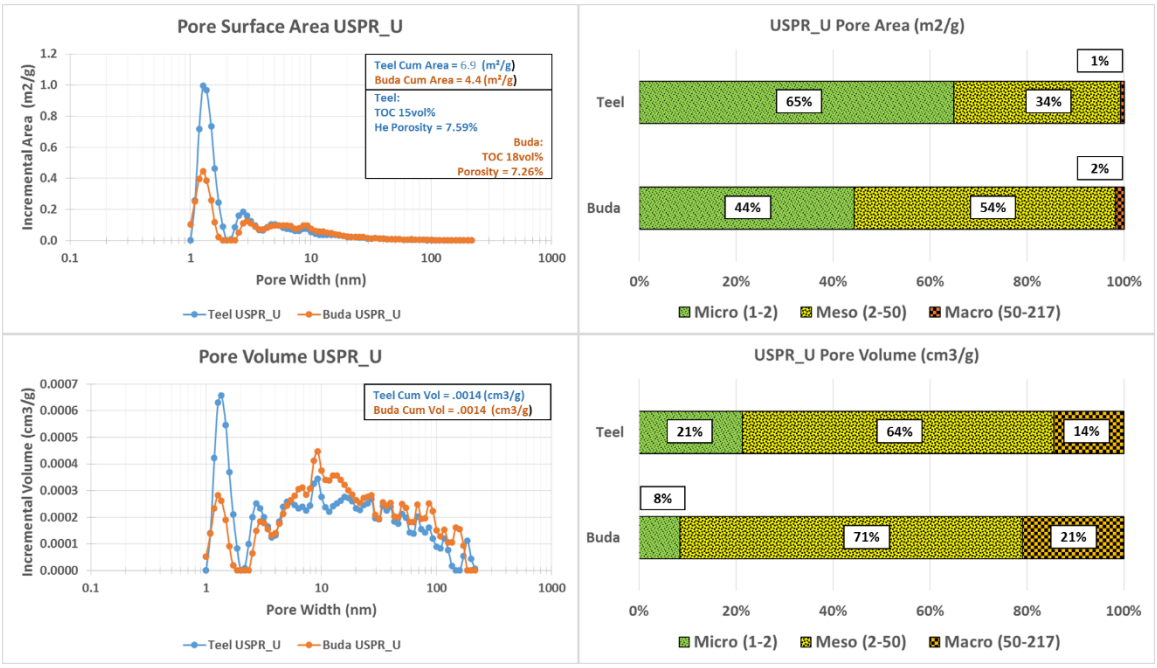

Figure 48: N_2 Adsorption Pore Surface Area and Volume for Samples in the USPR_U.

The same themes described above for the LMARC_L are basically repeated in the USPR_U. The Teel has more incremental area and volume contributed from micropore sizes 1-2 nm relative to the Buda, whereas the Buda has more incremental area and volume contribution from the meso (2-50) and macro (>50) pore sizes relative to the Teel. Thus, the takeaway continues to be that the Teel is much more impacted by micropores than the Buda and has a significantly higher cumulative pore surface area (57% higher than the Buda), while the two wells have similar He Porosity% values and cumulative volume values.

Figure 49 contains the incremental pore area and pore volumes of the Lower USPR interval for both the Teel and Buda.

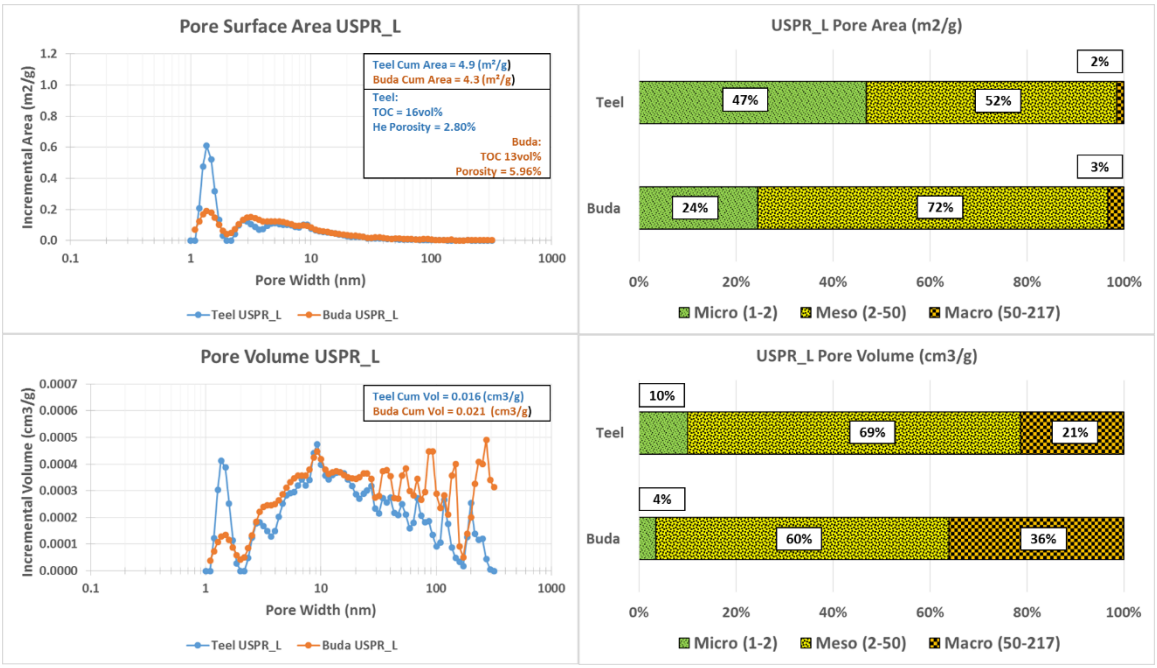

Figure 49: N_2 Adsorption Pore Surface Area and Volume for Samples in the USPR_L.

The trend seen above in the LMARC_L and USPR_U regarding pore size contribution carries forward into the USPR_L, with the Teel being much more impacted by micropores than the Buda, while the Teel continues to report a higher cumulative pore surface area (14% higher than the Buda). However, the differences between the two well's He Porosity% and cumulative pore volume values in the USPR_L are much larger than the differences in the other two intervals, with Buda's He Porosity% and cumulative pore volume values being 113% and 31% higher, respectively.

4. DISCUSSION

4.1 Resistivity Assessment

As seen from the open hole logging data in Figure 28, the Buda (a noncommercial well south of the LOD) displays exceptionally low resistivity (0.06-0.13 Ohmms), while the Teel (a commercial well north of the LOD) has normal organic mudrock resistivity values (62-101 Ohmms). This study postulates two variables, that when combined, could explain the different conductivity measurements between the north and the south side of the LOD; the first being the discovery of silver in the Buda STEM samples (see Section 3.3.1.1) and the corresponding lack of silver in the Teel STEM samples (see Section 3.3.1.2), and the second being the carbon ordering evidence provided by the Raman Spectroscopy (see Section 3.3.2) which indicates that the two wells have markedly different carbon ordering attributes with the Teel OM being classified as low-grade amorphous material while the Buda OM is classified as medium-grade transitional material.

4.1.1 Silver Discovery

Silver is the most electrically conductive metal on earth (Hammond, 2004). In fact, silver's conductivity is the measurement standard used to determine the conductive capabilities of all other elements. The conductive superiority of silver is due to its valence and crystal structure that allows its electrons to move freer than the other elements. When OM becomes more ordered, electrons begin moving freely from connected aromatic carbon rings, which in turn makes the rock hosting the OM become more conductive. Thus, the higher conductivity south of the LOD could be the result of a combination of

the rock's higher ordered structure and the fact that the rock contains an inherently conductive element.

As evidence of silver in the Marcellus had never been noted prior to this study, this study's workflow did not include procedures directly related to determining the source of the silver located in the Buda OM. However, if it is confirmed that silver does play a part in the LOD conundrum it will ultimately be very important to understand the source of that silver. In the spirit of sowing the seeds for future research, the following paragraphs will advance some thoughts regarding potential sources of the silver discovered in this research.

When initiating a thought experiment concerning the source of the silver discovered in the Buda OM, hydrothermal activity quickly comes to mind as it is a common enrichment driver for silver in surrounding strata. However, there is no evidence of Mississippi Valley type hydrothermal activity in the Marcellus. However, the exclusion of hydrothermal activity does not preclude other diagenetic processes. For example, the SEM EDS investigation in this study also identified several rare phosphate mineral inclusions (monzonite or churchite) which were interpreted via the elemental discovery of Uranium (U), Gadolinium (Gd), and Dysprosium (Dy). With that said even common minerals such as feldspars have compositions close to the fundamental K-Na-Ca plane, and cations, such as Rubidium (Rb), Caesium (Cs), Lead (Pb), Barium (Ba), Strontium (Sr), and Silver (Ag), can be substitutes for the alkali earth elements in feldspar structures. Published low-temperature (ca. 300^{o}C) ion-exchange experiments have produced pure end-member silver feldspar (AgAlSi3O8) from a natural sanidine starting material

(Clarke, 2008). As a result, diagenetic silver enrichment cannot be ruled out as the possible source of the silver in the Buda OM, especially when much of the surrounding sediments were derived from weathered igneous volcanic sources of the Acadian orogenic belt (Hosterman and Whitlow, 1981) that are known to include trace and rare earth elements (Lipin and Mckay, 1989). Thus, it is not impossible that these sediments could have acted as sources of silver mobilization in the subsurface.

Another potential explanation regarding the source of the silver contained within the Buda OM is that the silver is autochthonous in nature and was taken from the surrounding water as OM flocculated out of the water column. This mechanism is explained in the work of McKay (2008) related to the accumulation of silver in marine sediments and suggests that silver can be enriched in decaying organic particles, and that within these enriched particles anoxic microenvironments develop as the result of organic degradation leading to the formation of dissolved sulfide and the rapid precipitation of silver; most probably as Ag_2S. Further, McKay suggests that sedimentary redox conditions are not the primary controlling factor for Ag accumulation, nor do variations in the lithogenic and anthropogenic fluxes control Ag accumulation. Instead, McKay hypothesizes that the differences in sedimentary Ag accumulation are related to changes in the biogenic and/or scavenged flux to the sediment. According to McKay's theory, the trend of increasing sedimentary Ag concentrations going downslope most probably reflects the longer residence time of organic particles in the water column (i.e., more time for Ag scavenging), possibly enhanced by higher concentrations of dissolved Ag in deeper waters. Per McKay, the scavenging efficiency of Ag by organic particles appears to be

related to oxygen levels in the water column; which merely reflects the fact that settling organic particles become anoxic more rapidly when oxygen is limited, allowing more time for Ag scavenging. Accordingly, scavenging results in higher sedimentary Ag concentrations when an environment is characterized as an oxygen minimum zone (OMZ).

4.1.2 Carbon Ordering Evidence

It is widely accepted that after deposition and early diagenesis, the organic content of sedimentary rocks constitutes a heterogeneous mixture of organic compounds. During organic maturation, mainly O, H, N, and to a lesser degree C, are expelled from the organic material, changing the chemical composition and structure of the residual organic material. This process leads to an enrichment of aromatic species (Vandenbroucke and Largeau 2007) and the formation of basic structural units (BSU) of polyaromatic (4–10 cycles) layers that are either isolated or piled up by 2–3 units (Oberlin 1989). The nanometer sized BSU is described by the mean stacking height (Lc) and the mean basal plane diameter (La). During the early stages of diagenesis and catagenesis, the BSUs are randomly oriented, but start to synchronize their orientation to form molecular orientation domains (Bustin et al. 1995, Vandenbroucke and Largeau 2007). During graphitization, Lc and La progressively increase, while at the same time, the number of defects and the interplanar spacing between the graphene layers is reduced (Buseck and Huang 1985, Wopenka and Pasteris 1993). Thus, highly ordered graphitic material has few structural defects, larger La and Lc values and lower interplanar spacing. In other words, the carbon structure is highly oriented and connected, which allows for ease of electron transfer.

The Raman work, with the aid of the Lahfid and Kouketsu deconvolution methods, illustrates that the Buda is more ordered than the Teel. To relate this ordering to the graphitization process described in the previous paragraph, the Buda's OM is characterized by larger and more connected aromatic layers with fewer defects outside the plane of aromatic layers, resulting in a higher capacity for connectivity and electrical conductivity. If early graphitization is occurring in the Buda then, how would this carbon ordering be impacting OM hosted pores? Using TEM on very high maturity graphite samples Beyssac (2002b) observed that as carbon aromatic layers begin to become aligned the PSD shifts to the right with micropores coalescing into mesopores and macropores; which is precisely what this study's pore surface area and pore volume analysis found in the Buda OM samples, as documented in sections 3.4.2 and 3.4.3.

4.2 Reservoir Quality Assessment

As seen from the global pore segmentation results in section 3.4.3 and the N_2 adsorption results in section 3.4.4, there are quantifiable PSD differences between the Teel and the Buda. This section will expand on these findings and discuss their implications considering the carbon ordering discussion from section 4.1.

The global SEM pore segmentation results and the N_2 NLDFT results highlight two interesting differences between the Teel (a commercial well from the north side of the LOD) and the Buda (a noncommercial well from the south side of the LOD); the Buda has significantly less pores in the lower pore range 1-2nm than does the Teel, and the Buda has significantly more pores in the meso and macro ranges than does the Teel. This PSD shift is especially interesting when considered in the light of Raman Spectroscopy results.

The works of Beyssac (2002b), Bonijoly (1982) and De Fonton (1980) describe the effects on carbon material when subjected to temperature and pressure, and propose the existence of a new carbon phase (the macroporous phase) that is texturally and structurally macroporous and turbostratic (conductive). The macroporous phase results from the coalescence of micropores in the OM due primarily to the effects of pressure, and secondarily from temperature. More precisely, the graphitization in a macroporous phase is caused when pore walls break due to the stress and shear pressure that develop in a porous phase submitted to hydrostatic pressure. Can the Buda's strangely high conductivity and its scarcity of micropores, as compared to the Teel, be explained by a macroporous phase? The size and scope of this study precludes definitively linking the LOD phenomena to a macroporous carbon phase. However, given the dearth of other operational theories to explain the LOD it seems very reasonable to consider the findings of this study sufficient evidence to assert that a macroporous carbon phase qualifies as a working hypothesis to explain the LOD phenomena. Said differently, given the lack of another scientifically supportable theory to explain the LOD, it would be very unreasonable to ignore the findings in this study and conclude that a macroporous carbon phase does not explain the LOD phenomena.

4.3 Ramifications of This Study to Future Research

To confirm the discovery of silver south of the LOD (and the lack of silver on the north side of the LOD), and to determine the role, if any, silver plays in the very low resistivity levels south of the LOD, more core and cutting samples from areas on both sides of the LOD should be examined specifically for the existence of silver. Given that

STEM EDS is excessively time consuming, SEM EDS is likely the more appropriate method to identify silver in samples taken from a larger representative sample of NE PA Marcellus OM. To evaluate if the theories within the McKay work can be used to explain the source of the silver found in the Buda OM samples, an extensive chemo stratigraphic paleo shelf study of NE PA would be needed. It would also be useful to study Marcellus outcrops across Southern NY and Eastern PA in search of silver content.

To augment the findings in this study that the south side of the LOD exhibits characteristics of higher ordering, Raman Spectroscopy, which is inexpensive, needs to be applied to many more NE PA Marcellus wells at, or around, the LOD. There also should be attempts to visualize ordered carbon stacking and aromatic rings using darkfield TEM imaging on a rotating stage with the appropriate aperture to produce an image that displays stacked ordered rings as bright spots (Oberlin, 1980a). Such images would allow direct comparison of the rock north and south of the LOD, with the expectation being that the conductive noncommercial rock would have a higher frequency of bright spots as compared to the productive nonconductive rock.

To advance this research's findings concerning the PSD differences between the north side and the south side of the LOD, the SEM resolvable limit needs to be reduced to single digits using higher magnification SEM mosaics which would optimize the integration of the SEM segmentation data and the N_2 adsorption surface area calculations. Reductions in the SEM resolvable limit will also serve to reduce the fit degradation between global pore segmentation data and N_2 adsorption data that was experienced in this study, as illustrated in Figure 50. Extending the fit into the single digits will require

mosaics made up of 7500X or 10000X images, and segmented pore data from such mosaics should allow for a better understanding of the parameters associated with OM hosted porosity and allow for extensive research in the fine tuning of DFT models to better characterize the PSDs of organic rich mudrocks. Lastly, if the adsorption testing was conducted with CO_2 as well as N_2, a wider PSDs could be obtained that could be resolvable down to the sub nanometer pore range.

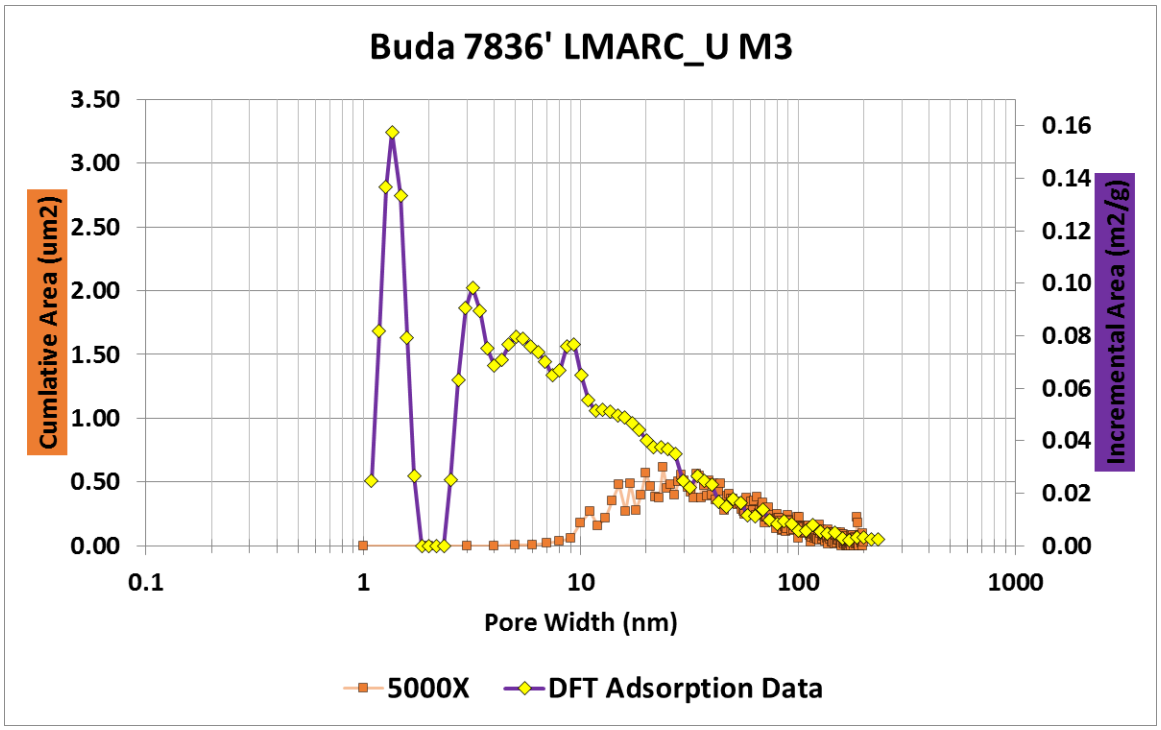

Figure 50: Buda Pore Area Comparison. Derived from globally segmented 5000X mosaic and DFT N_2 absorption data.

4.4 Ramifications of This Study to Operators in the NE PA Dry Gas Window

Whereas this study was successful in providing a legitimate working theory to explain what could be causing the noncommercial drilling outcomes that are commonly experienced as the LOD is approached from the north, this study does not provide

methodology to specifically identify the location of the LOD. As noted in section 4.3, the findings in this study suggest that more OM samples need to be subjected to SEM EDS (regarding identifying silver) and Raman Spectroscopy (regarding identifying evidence of carbon ordering). While this additional data will not be determinative in locating the exact location of the LOD, it appears reasonable that such data will be useful when added to existing data sources that are considered when evaluating acreage with proximity to the LOD.

While this study advances a theory that increased carbon ordering south of the LOD can explain the low resistivity and the porosity degradation seen south of the LOD, it is not asserting the existence of a linear relationship between resistivity and porosity that rises to the level of actionable data to be used in the evaluation of drilling locations. In fact, higher silver content within OM could cause lower resistivity values that are not solely derived from the conductive carbon alone. Said differently, if an operator is making drilling location decisions solely on resistivity levels, they may be passing over commercial well sites.

Operators in the NE PA Dry Gas Window sometimes experience higher production from laterals that approach the LOD, which on its face appears contrary to the impacts of the carbon ordering theory described and proposed by this study. However, a logical application of the carbon ordering process can be used to create a very plausible theoretical explanation; early shifts in PSD caused by the ordering process can provide short term improvements to the OM hosted porosity. As micropores coalesce due to carbon ordering, at some point an optimal PSD will exist that maintains the appropriate surface area needed

for commercial quantities of gas and large enough pore sizes to allow optimal gas flow to the wellbore. However, like everything in this world, this optimum PSD for commercial volumes of gas and ease of flow has a tipping point, after which the micropore surface area is degraded, along with the gas production.

5. CONCLUSIONS

5.1 Conclusions

The Marcellus Shale is the single largest natural gas producing resource in the U.S., both currently and for the foreseeable future, which has resulted in Pennsylvania becoming the second largest natural gas producing state in the U.S (EIA, 2017). The majority of the production in Pennsylvania comes from the Marcellus Shale Dry Gas Window comprising the six counties in NE PA (Pennsylvania Department of Reporting Services, March 2017). Despite its impressive production volume, the NE PA Dry Gas Window is plagued by the "Line of Death" (LOD); a term coined by producers to describe a misunderstood, and ever changing, line of demarcation that forms the southernmost limit of commercial production in the NE PA Dry Gas Window. Noncommercial wells on, or to the south of, the LOD are characterized by very low resistivity values (i.e. as low as 0.08 Ohmm based upon deep resistivity log curve response) and lower total porosity values (i.e. helium porosity measurements decreasing from ~7% north of LOD to ~5% south of the LOD), while other attributes such as minerology, TOC, Ro% and thickness remain very comparable between the two sides of the LOD. Previous research aimed at developing a plausible explanation of the precise nature and cause of the LOD have been inconclusive.

This study's Resistivity Assessment and Reservoir Quality Assessment together articulate a plausible explanation of the LOD phenomenon. The Resistivity Assessment presents arguments of two possible sources of the unusually high conductivity found at, and to the south of, the LOD in NE PA; the discovery of silver in OM south of the LOD

(and lack thereof north of the LOD), and evidence of increased carbon ordering south of the LOD. The Reservoir Assessment presents arguments that the increased carbon ordering south of the LOD is also responsible for a progressive shift of the PSD, which in turn has diminished the rocks ability to hold gas.

While the discovery of silver in this study's STEM EDS workflow is interesting, this study does not conclude that its presence alone is determinative in regard to the source of the low resistivity south of the LOD. Instead, this study argues that the primary source of the low resistivity south of the LOD relates to its higher carbon ordering, which was observed by this study's Raman Spectroscopy workflow, and that it is the combined impact of a highly conductive element within a higher ordered material that is responsible for the exceptionally low resistivity values recorded south of the LOD.

This study was predicated upon a hypothesis that the source of the LOD was due to graphic pyrobitumen graphitization that could not be identified through XRD analysis. Accordingly, this study's reservoir assessment included large scale mosaic SEM imaging and N_2 adsorption which, when combined, illustrates that the PSDs between the north side and south side of the LOD are not comparable, most notably because the south side of the LOD has lost micropores and gained meso and macro sized pores.

The common thread in this study's findings regarding the low resistivity and low porosity found south of the LOD is the evidence pertaining to levels of carbon ordering across the LOD. This study argues it would be an understatement to interpret these findings as merely suggesting that the low resistivity and low porosity rock on the south side of the LOD is due to being a bit more ordered than the rock north of the LOD. Instead,

this study asserts that the south side of the LOD has entered a macroporous carbon phase that causes its OM to be characterized as transitional carbon material whereas the OM on the north side of the LOD remains amorphous material. The south's higher ordered carbon phase is not only more turbostratic, but is texturally and structurally macroporous due to coalescence of micropores in the material caused by the effects of temperature and pressure (below graphite grade metamorphism). As a result of this macroporous phase, the OM south of the LOD has drastically decreased pore surface area, which translates into the noncommercial outcomes experienced by operators as they approach the LOD.

Whereas this study has succeeded in developing a plausible working hypothesis for the high conductivity and lack of commercial production south of the LOD, more research is required. Just as the Weatherford Laboratories Work (section 1.3.2.2) opened the door for this study, the thought processes advanced in this study have opened the door to more research on various fronts (see section 4.3). Whereas this study provided evidence for silver, it does not provide operators a silver bullet to identify precisely how far to the south they can drill before experiencing noncommercial outcomes. However, this study does provide operators with some targeted testing techniques (see section 4.3) that, if systematically applied to a larger population of OM samples, will illuminate the extent and effects of the carbon ordering process, which should be helpful to operators as they rationalize future exploitation and development activities on acreage with proximity to the LOD.

REFERENCE LIST

AMMRF, (2017): Qualitative EDS X-ray microanalysis using SEM and TEM. Australian Microscopy & Microanalysis Research Facility.

Asahina, S., (2012): High-Resolution low-voltage scanning electron microscope study of nanostructured materials. Microscopy and Microanalysis

Beny-Bassez C., Rouzaud J.N., (1985): Characterization of carbonaceous materials by correlated electron and optical microscopy and Raman microspectroscopy. Scanning Electron Microscopy 119-1132

Bustin M., Rouzaud J.N., Ross J.V., (1995): Natural graphitization of anthracite: experimental considerations. Carbon 33(5): 679-691

Beyssac, O., Goffe, B., Chopin, C., Rouzaud, J.N., (2002a): Raman spectrum of carbonaceous material in metasediments: a new geothermometer. Journal of Metamorphic Geology, 20, 859-871

Beyssac O., Rouzaud, J.N., Goffe, B., Brunet, F., Chopin, C., (2002b): Graphitization in high pressure, low temperature metamorphic gradient: a HRTEM and Raman microspectroscopy study. Contributions to Minerology and Petrology, 143, 19-31

Beyssac, O., Goffe, B., Petitet, G.P., Froigneux, E., Moreau, M., Rouzaud, J.N., (2003a): On the characterization of disordered and heterogeneous carbonaceous materials using Raman spectroscopy. Spectrochimica Acta Part A, 59, 2267-2276

Bonijoly M., Oberlin M., Oberlin A., (1982): A possible mechanism for natural graphite formation. International Journal of Coal Geology 1:283-312

Buseck P.R., Huang B.J., (1985): Conversion of carbonaceous material to graphite during metamorphism. Geochimica et Cosmochimica Acta 49:2003-2016

Clarke D.B., (2008): Silver-bearing alkali feldspars in experiment- and in nature? Atlantic Geology Volume 44 2008

Clarke, A. R., (2002) Microscopy techniques for materials science. CRC Press

Chipera, S. J. & Bish, D. L., (2002): Fullpat: A full pattern quantitative analysis program for X-ray powder diffraction using measured and calculated patterns. Journal of Applied Crystallogrpahy 35, 744-749.

Cooper, G. A., (1930): Stratigraphy of the Hamilton Group of New York. American Journal of Science, 5th series, v. 19, p. 116–134, 214-236.

Cuesta A., Dhamelincourt P., Laureyns J., Martínez-Alonso A. & Tascón J.M.D., (1994): Raman microprobe studies on carbon materials. Carbon 32, 1523–32.

Chung, D.D.L., (2002): Review Graphite. Journal of Materials Science 37 (2002) 1-15

Department of Reporting Services PA US, Oil and Gas, Accessed March 2017

De Fonton S., Oberlin A., Inagaki M., (1980): Characterization by electron microscopy of carbon phases (intermediate turbostratic phase and graphite) in hard carbons when head treated under pressure. Journal of Material Science 15:909-917

De Witt Jr., W., J.B., Roen and L.G., Wallace (1993): Stratigraphy of Devonian black shales and associated rocks in the Appalachian basin, in Roen, J. B. and R. C. Kepferle, 1993, Petroleum geology of the Devonian and Mississippian black shale of eastern North America: U.S. Geological Survey Bulletin 1909B, p. B1-B57

Dippel B., Jander H. & Heintzenberg J., (1999): Soot. Physical Chemistry Chemical Physics 1, 4707–12.

Egerton, R.F., (2005): Physical principles of electron microscopy: an introduction to TEM, SEM, and AEM. Springer, 202.

EIA, (2017): Marcellus Shale Play: Geology Review

EIA, (2016): U.S. Crude Oil and Natural Gas Proved Reserves Year-end 2015.

EIA, (2017): Drilling Productivity Report, for key tight oil and shale gas regions.

Emmanuel, O.O., & Sonnenberg, S.A., (2013a): Geologic Characterization and the Depositional Environment of the Middle Devonian Marcellus Shale, Appalachian Basin, NE USA. Unconventional Resources Technology Conference, August 12.

Emmanuel, O.O., & Sonnenberg, S.A., (2013b): Concepts and Methods for the Recognition of Cyclicity in the Marcellus Shale of the Appalachian Basin, NE USA. Unconventional Resources Technology Conference, August 12.

Escribano R., Sloan J.J., Siddique N., Sze N. & Dudev T., (2001): Raman spectroscopy of carbon containing particles. Vibrational Spectroscopy 26, 179–86.

Ettensohn, F.R., (2008): Chapter 4 The Appalachian Foreland Basin in Eastern United States, Editor(s): Andrew D. Miall, In Sedimentary Basins of the World, Elsevier, Volume 5, Pages 105-179

Ettensohn, F. R., (1992): Controls on the origin of the Devonian-Mississippi oil and gas shales, east-central United States: Fuel, v. 71, p. 1487-1492

Ettensohn, F. R., (1985): Controls on development of the Catskill Delta Complex, In: Woodrow, D. L., and Sevon, W.D., (Eds.), The Catskill Delta, Geological Society of America Special Paper 201, p. 65-74

Faill, R.T., (1997): A geologic history of the north-central Appalachians; Part 1, Orogenesis from the Mesoproterozoic through the Taconic Orogeny. American Journal of Science, v. 297, p. 551-619.

Ferralis N., Matys, E.D., Knoll, A.H. Hallmann C., Summons, R.E., (2016): Rapid, direct and non-destructive assessment of fossil organic matter via microRaman spectroscopy. Carbon Volume 108, November 2016, pages 440-449

Giannuzzi L.A., (2012): EXpressLO for fast and Versatile FIB Specimen Prep. Microscopy and Microanalysis

Goldstein, G.I., Newbury, D.E., Echlin, P., Joy, D.C., Fiori, C., Lifshin, E., (1981): Scanning electron microscopy and x-ray microanalysis. New York: Plenum Press.

Gor, G.Y., Thommes, M., Cychosz, K.A., Neimark, A.V., (2012): Quenched solid density functional theory method for characterization of mesoporous carbons by nitrogen adsorption. Carbon 50 1583–1590.

Hammond, C. R., (2004): The Elements, in Handbook of Chemistry and Physics (81st ed.). CRC press.

Harrison, M., (2004): The Lackawanna Synclinorium, Pennsylvania: A salt-collapse structure, partially modified by thin-skinned folding. GSA Bulletin. v. 116. no. 11/12. pp. 1499-1514.

Hall, J., (1839): Third annual report of the Fourth Geological District of the State of New York. Geological Survey of New York Annual Report, v. 3, p. 287–339.

Hosterman, J.W., Whitlow, S., (1981): Open File Report (US); (United States). Clay minerology of Devonian Shales in the Appalachian Basin. Geologically survey Volume 81, 585 pages.

Jawhari T., Roid A. & Casado J., (1995): Raman spectroscopic characterization of some commercially available carbon black materials. Carbon 33, 1561–65.

Jiang, S., (2012): Clay Minerals from the Perspective of Oil and Gas Exploration: Clay Minerals in Nature – Their Characterization, Modification, and Application. Chapter 2. INTECH

Johnson, J.G., Klapper G., and Sandberg, C.A., (1985): Devonian eustatic fluctuations in Euramerica. Geological Society of America Bulletin, v. 96, p. 567–587

Katagiri G., Ishida H., and Ishitani A., (1988): Raman spectra of graphite edge planes. Carbon, 26, 565–571

Klapper, G., (1971): Sequence within the conodont genus Polygnathus in the New York lower Middle Devonian. Geologica et Palaeontologica 5, 59–72.

Kouketsu Y., Mizukami T., Mori H., Endo S., Aoya M., Hara H., Nakamura D. and Wallis S., (2014): A new approach to develop the Raman carbonaceous material geothermometer for low-grade metamorphism using peak width. Island Arc, 23, 33–50.

Lahfid A., Beyssac O., Deville E., Negro F., Chopinc. & Goffé B., (2010): Evolution of the Raman spectrum of carbonaceous material in low-grade metasediments of the Glarus Alps (Switzerland). Terra Nova 22, 354–60.

Landers, J., Gor, G., Neimark, A.V., (2013): Density Functional theory methods for characterization of porous materials. Colloids and Surfaces A: Physicochem. Eng. Aspects 437 (2013) 3– 32

Lash G.G. and Engelder T., (2011): Thickness trends and sequence stratigraphy of the Middle Devonian Marcellus Formation, Appalachian Basin: Implications for Acadian foreland basin evolution. AAPG Bulletin, v. 95, NO.1 (January), PP. 61-103

Laughrey, C., (2011): Black Shale Diagenesis: Insights from Integrated High-Definition Analyses of Post-Mature Marcellus Formation Rocks, Northeastern Pennsylvania. AAPG Search and Discovery Article #110150

Lespade, P., André Marchand, Michel Couzi, Francis Cruege, (1984): Caracterisation de materiaux carbones par microspectrometrie Raman. Carbon, Volume 22, Issues 4–5, 1984, Pages 375-385

Lipin, B.R., Mckay, G.A., (1989): Geochemistry and mineralogy of rare earth elements. Reviews in Minerology and Geochemistry 21 (8), 45-77

Lunsdorf N.K., Dunkl I., Schmidt B.C., Rantitsch G. and von Eynatten H., (2014a): Towards a higher comparability of geothermometric data obtained by Raman spectroscopy of carbonaceous material. Part 1: Evaluation of biasing factors. Geostandards and Geoanalytical Research, 38, 73–94.

Lunsdorf N.K., Dunkl I., Schmidt B.C., Rantitsch G. and von Eynatten H., (2014b): Towards a higher comparability of geothermometric data obtained by Raman spectroscopy of carbonaceous material. Part 2: A Revised Geothermometer. Geostandards and Geoanalytical Research, 38, 73–94.

Matthews M.J., Pimenta M.A., Dresselhaus G., Dresselhaus M.S. and Endo M., (1999): Origin of dispersive effects of the Raman D band in carbon materials. Physical Review B, 59, R6585–R6588.

Mckay J.L., Pedersen, T.F., (2008): The accumulation of silver in marine sediments: A link to biogenic Ba and Marine productivity. Global biogeochemical cycles, Vol. 22, GB4010

Milliken, K., (2013): Organic matter–hosted pore system, Marcellus Formation (Devonian), Pennsylvania. AAPG Bulletin, V 97, NO. 2 PP 177-200

Mroczkowska, M., (2015): The analysis of pore space parameters of shale gas formations rocks within the range of 50 to 2 nm. Nafta-Gaz. 71. 983-991. 10.18668/NG2015.12.06.

Neimark AV, Lin Y, Ravikovitch PI, Thommes M., (2009): Quenched solid density functional theory and pore size analysis of micro–mesoporous carbons. Carbon 2009; 47:1617–28.

Oberlin, A., (1989): High resolution TEM studies of carbonization and graphitization. In Chemistry and Physics of carbons, Vol. 22, Thrower, P.A., ed., pp 143

Oberlin, A., Boulmier, J.L. and Villey, M., (1980a): Electron microscopic study of kerogen microtexture. Selected criteria for determining the evolution path and evolution stage of kerogen. In: B. Durand (Editor), Kerogens. Technip, Paris, pp. 191--241.

Olivier, J.P., (1998): Improving the models used for calculating the size distribution of micropore volume of activated carbons from adsorption data. Carbon 36, 1469–1472 (1998)

Passey Q.R., Bohacs, K.M., Esch, W.L., Klimentidis, R., Sinha, S., (2010): From oil-prone source rock to gas- producing shale reservoir – geologic and petrophysical characterization of unconventional shale-gas reservoirs. SPE 131350. International oil and gas conference and exhibition in China

Rast, N., and Skehan, J. W., (1993): Mid-Paleozoic orogenesis in the North Atlantic: The Acadian orogeny, in D. C. Roy and S. J. Skehan, eds., The Acadian orogeny. Geological Society of America Special Paper 275, p. 1–25

Ravikovitch, P.I., Vishnyakov, A., Russo, R., Neimark, A.V., (2000): Unified approach to pore size characterization of microporous carbonaceous materials from N2, Ar, and CO2 adsorption isotherms. Langmuir 16, 2311–2320 (2000)

Ravikovitch, P.I., Jagiello, J., Tolles, D., Neimark, A.V., (2001): Improved DFT methods for micropore size characterization of activated carbons: role of pore wall heterogeneity. Extended abstracts, Carbon'01 conference, American Carbon Society, Lexington (Kentucky, USA), 2001.

Repetski, (2008): Thermal Maturity Patterns (CAI and %Ro) in Upper Ordovician and Devonian Rocks of the Appalachian Basin: A Major Revision of USGS Map I–917–E Using New Subsurface Collections, U.S. Geological Survey Scientific Investigations Map 3006

Robertson J., (1986): Amorphous Carbon. Advances in Physics, Volume 35 issue 4

Sadezky A., Muckenhuber H., Grothe H., Niessner R. and P€oschl U., (2005): Raman microspectroscopy of soot and related carbonaceous materials: Spectral analysis and structural information. Carbon, 43, 1731–1742.

Sato K., Saito R., Oyama Y., Jiang J., Cancado L.G., Pimenta M.A., Jorio A., Samsonidze G.G., Dresselhaus G. and Dresselhaus M.S., (2006): D-band Raman intensity of graphitic materials as a function of laser energy and crystallite size. Chemical Physics Letters, 427, 117–121.

Schumacher, Brian A., (2002): Methods for the Determination of Total Organic Carbon (TOC) in Soils and Sediments. Ecological Risk Assessment Support Center

Seaton, N.A., Walton, J.P.R.B., Quirke, N., (1989): A new analysis method for the determination of the pore size distribution of porous carbons from nitrogen adsorption measurements. Carbon 27, 853–861 (1989)

Shula, E., (2014): Thermal Maturity of the Marcellus Shale and the "Line of Death": NE Pennsylvania. The American Institute of Professional Geologists 6th Annual Conference

Sing, K.S.W., Everett, D.H., Haul, R.A.W., Moscou, L., Pierotti, R.A., Rouquerol, J., Siemieniewska, T., (1985): Reporting physisorption data for gas/solid systems with special reference to the determination of surface area and porosity. Pure Appl. Chem. 57, 603–619 (1985)

Sing, K.S.W., (2001): The use of nitrogen adsorption for the characterization of porous materials. Colloids and surfaces Physicochemical and engineering aspects 187-188 (2001) 3-9

Smith, L.B., and Leone, J., (2010): Integrated Characterization of Utica and Marcellus Black Shale Gas Plays, New York State. AAPG, Search and Discovery Article #50289.

Tsu R., Gonzalez, H. & Hernandez, I., (1978): Observation of splitting of the E2g mode and two photon spectrum in graphites. Solid State Communications, 27, 507-510

Tuinstra F. and Koenig J. L., (1970): Raman spectrum of graphite. J. Chem. Phys., 1970, 53, 1126–1130

Tyson, R.V. and T.H. Pearson, (1991): Modern and ancient continental shelf anoxia: an overview. Geological Society Special Publication No 58, pp 1-24

United States Geological Survey (2011): Assessment of undiscovered oil and gas resources of the Devonian Marcellus shale of the Appalachian basin province. National Assessment of Oil and Gas

Vandenbroucke M. and Largeau C., (2007): Kerogen origin, evolution and structure. Organic Geochemistry, 38, 719–833.

Walters, C., (2014): Influence of turbostratic nanostructures on electrical conductivity in shale. International Journal of Coal Geology. v. 122 pp. 105-109.

Wang Y., Alsmeyer D. C. & McCreery R. L., (1990): Raman spectroscopy of carbon materials: Structural basis of observed spectra. Chemistry of Materials 2, 557–63.

Williams, H., and R. D. Hatcher, Jr., (1982): Suspect terranes and accretionary history of the Appalachian orogeny. Geology, v. 10, p. 530-536.

Wopenka, B. & Pasteris, J.D., (1993): Structural characterization of kerogens to granulite-facies graphite, Applicability of Raman microprobe spectroscopy. American Mineralogist, 78, 533-557

Yang, A., Heidari, Z., (2016): An experimental approach to quantifying the impact of kerogen maturity on its chemical aromaticity and electrical conductivity. Society of Petrophysicts and Well-Log Analysts

Supplemental Sources Consulted

Alfred, D., and Vernik, L., (2013): A new petrophysical model for organic shales. Petrophysics, (3), 240-247.

Ambrose, R.J., Hartman, R.C. Diaz-Campos, M., Akkutlu, Y., and Sondergeld, C.H., (2010): New pore-scale considerations for shale gas in place calculations Paper SPE-

131772, presented at the 2010 SPE Unconventional Gas Conference, Pittsburgh, Pennsylvania, USA, 23–25 February

Aoya M., Kouketsu Y., Endo S. et al., (2010): Extending the applicability of the Raman carbonaceous material geothermometer using data from contact metamorphic rocks. Journal of Metamorphic Geology 28, 895–914.

Archie, G.E., (1942): The Electrical Resistivity Log as an Aid in Determining Some Reservoir Characteristics. Paper SPE- 942054-G, Petroleum Transactions, AIME, 146, 54–62.

Barrett E.P., Joyner, L.G. Halenda, P.P., (1951): The determination of pore volume and area distributions in porous substances. I. Computations from nitrogen isotherms. Journal of the American Chemical Society 73 (1951) 373–380.

Brunauer, S., Emmett, P.H., Teller, E., (1938): Adsorption of gases in multi-molecular Layers. Journal of the American Chemical Society 60 (1938) 309–319.

Beyssac O., Rouzaud JN, Brunet F, Petitet JP, Geoffe B., (2000): Pressure effects on graphitization: experimental constraints. Journal of Conference Abstracts 5:13

Beyssac O., Brunet F., Petitet J., Goffé B. & Rouzaud J.N., (2003b): Experimental study of the microtextural and structural transformations of carbonaceous materials under pressure and temperature. European Journal of Mineralogy 15, 937–51.

Beyssac O. and Lazzeri M., (2012): Application of Raman spectroscopy to the study of graphitic carbons in earth sciences. In: Dubessy J., Caumon M.-C. and Rull F. (eds), Raman spectroscopy applied to Earth sciences and cultural heritage. European Mineralogical Union and Mineralogical Society of Great Britain and Ireland (London), 415–454.

Buseck P.R., Huang B.J., Miner B., (1998): Structural order and disorder in Precambrian kerogens. Organic Geochemistry 12:221-234

Chen, H., Firdaus, G., Heidari, Z., (2014): Impact of anisotropic nature of organic rich source rocks on electrical resistivity measurements. SPWLA 55th Annual Logging Symposium, Abu Dhabi, United Arab Emirates, May 18-22, 2014

Chen, H., Chi, Lu., Kethireddy, N., Heidari, Z., (2013): Impact of Spatial Distribution of kerogen network on electrical resistivity of organic rich source rocks. SPE 168923 / URTeC 1619806, Denver Colorado, USA August 12-14, 2013

Cooper, G. A., (1933): Stratigraphy of the Hamilton Group of eastern New York, part 1. American Journal of Science, v. 26, p. 537–551.

Cooper, G. A., (1934): Stratigraphy of the Hamilton Group of eastern New York, part 2. American Journal of Science, v. 27, p. 1–12.

Curtis M.E., Sondergeld C.H., Ambrose R.J., Rai C.S., (2012) Microstructural investigation of gas shales in two and three dimensions using nanometer-scale resolution imaging. American Association of Petroleum Geologists Bull 96:665–677A

Egerton R.F., (2014): Choice of operating voltage for a transmission electron microscope. Ultramicroscopy

Ferralis N., (2010) Probing mechanical properties of graphene with Raman spectroscopy. Journal of Material Science 45:5135–5149

Ferrari A.C. & Robertson J., (2000): Interpretation of Raman spectra of disordered and amorphous carbon. Physical Review B 61, 95–107.

Ferrari, A.C., Robertson, J., (2001): Resonant Raman spectroscopy of disordered, amorphous, and diamond like carbon. Phys. Rev. B 64 (7) (2001) 075414.

Giannuzzi L.A., Stevie F.A., (2005): "Introduction to Focused Ion Beams, Instrumentation, Theory, Techniques, Practice". Springer Publications

Heath J.E., Dewers T.A., McPherson BJOL, Petrusak R., Chidsey T.C., Rinehart A.J., Mozley P.S., (2011): Pore networks in continental and marine mudstones: Characteristics and controls on sealing behavior. Geosphere 7:429–454

Heidari, Z., (2010): Quantitative method for estimating total organic carbon and porosity, and for diagnosing mineral constituents from well logs in shale-gas formations. Society of Petrophysicists and Well-Log Analysts, SPWLA 52nd Annual Logging Symposium, 14-18 May, Colorado Springs, Colorado

Heidari, Z., Torres-Verdin, C., and Pregg, W. E., (2011): Quantitative method for estimating total organic carbon and porosity, and for diagnosing mineral constituents from well logs in shale-gas formations. Transactions of the SPWLA 52nd Annual Logging Symposium, Colorado Springs, Colorado, May 14-18.

Huang J., Cavanaugh T., Nur B., (2013): An introduction to SEM operational principles and geologic applications for shale hydrocarbon reservoirs. American Association of Petroleum Geology Mem 102:1–6

Jagiello, J., Olivier, J.P., (2009): A simple two-dimensional NLDFT model of gas adsorption in finite carbon pores. Application to pore structure analysis. J. Phys. Chem. C113 (2009) 19382–19385.

Jagiello, J., Kenvin, J., Olivier, A., Lupini, C., Contescu, (2011): Using a new finite slit pore model for NLDFT analysis of carbon pore structure. Adsorpt. Sci. Technol. 29 (2011) 769–780.

Kethireddy, N., Heidari, Z., and Chen, H., (2013): Quantifying the effect of kerogen on electrical Resistivity measurement in organic-rich source rocks. SPWLA 54th Annual Logging Symposium, New Orleans, Louisiana, USA, June 22–26.

Klimentidis R., Lazar O.R., Bohacs K.M., Esch W.L., Pededrsen P., (2010) Integrated petrography of mudstones. AAPG Ann Conv New Orleans, April 11–14

Landis C.A., (1971): Graphitization of dispersed carbonaceous material in metamorphic rocks. Contributions to Mineralogy and Petrology 30, 34–45.

Lastoskie, C., Gubbins, K.E., Quirke, N., (1993): Pore size distribution analysis of microporous carbons: a density functional theory approach. J. Phys. Chem. 97, 4786–4796 (1993)

Lawrence, R. and Jiang, Y., (2017): Porosity, pore size distribution, micro-structure. In Amziane, S. and Collet, F., eds. Bio-aggregates Based Building Materials. Netherlands: Springer International Publishing, pp. 39-71. (RILEM State- of-the-Art-Reports; 23)

Lespade, P., Al-Jishi, R., M.S., Dresselhaus, M.S., (1982): Model for Raman scattering from incompletely graphitized carbons. In Carbon, Volume 20, Issue 5, 1982, Pages 427-431

Levine, J., and Eggleston, J., (1992): The Anthracite Basins of Eastern Pennsylvania. Joint Meeting of the International Committee for Coal and Organic Petrology & The Society for Organic Petrology. U.S. G.S Open-Rile Report #92-568

Loucks RG, Reed RM, Ruppel SC, Jarvie DM (2009): Morphology, genesis, and distribution of nanometerscale pores in siliceous mudstones of the Mississippian Barnett Shale. J Sed Res 79:848–861

Lucille A Giannuzzi, (2012): Routine Backside Milling with EXpressLO, ISTFA 2012

Lunsdorf N.K., (2016): Raman spectroscopy of dispersed vitrinite – Methodical aspects and correlation with reflectance. International Journal of Coal Geology, 153, 75–86.

Lunsdorf N.K. and Lunsdorf J.O., (2016): Evaluating Raman spectra of carbonaceous matter by automated, iterative curve-fitting. International Journal of Coal Geology, 160–161, 51–62.

Nguyen, T.X., Bhatia, S.K., (2004): Characterization of pore wall heterogeneity in nanoporous carbons using adsorption: the slit pore model revisited. J. Phys. Chem. B108 (2004) 14032–14042.

Nguyen, T.X., Bhatia, S.K., (2004): Probing the pore wall structure of nanoporous carbons using adsorption. Langmuir 20 (2004) 3532–3535.

Oberlin, A., Oberlin, M., (1983): Graphitizabilty of Carbonaceous materials as studied by TEM and X-ray diffraction. Journal of Microscopy, Vol 132 Issue 3 pages 353-363, December

Oberlin, A., Villey, M., and Combaz, A., (1980b): Influence of elemental composition on
carbonization (Pyrolysis of kerosene shale and kuckersite). Carbon, 18: 347--353.

Oberlin, A., Oberlin, M. and Monthioux, M., (1980c): Carbon structures and microtextures. Carbon 80, Baden-Baden, Preprints, pp. 453--456.

Olivier, J.P., Conklin, W.B., Szombathely, M.V., (1994): Determination of pore size distribution from density functional theory: a comparison of nitrogen and argon results. Stud. Surf. Sci. Catal. 87 (1994) 81–89.

Olivier, J.P., (1995): Modeling physical adsorption on porous and nonporous solids using density functional theory. J. Porous Mater. 2 (1995) 217.

Passey, Q.R., Moretti F.J., Kulla J.B, Creaney, S.J., Stroud, J.D., (1990): A Practical Model for Organic Richness from Porosity and Resistivity Logs. AAPG Bulletin - AAPG BULL. 74. 1777-1794.

Passey, Q.R., Bohacs, K.M., Esch, W.L., Klimentidis, R., Sinha, S., (2012): My Source Rock is Now My Reservior – Geologic and Petrophysical Characterization of Shale Gas Reservoirs. AAPG Search and Discovery Article #80231

Pasteris, J.D., (1989): In situ analysis in geological thin-sections by Laser Raman microbe microspectroscopy: A cautionary note. Applied Spectroscopy. 43, 567-570

Pasteris J. D. and Wopenka B., (2003): Necessary, but Not Sufficient: Raman Identification of Disordered Carbon as a Signature of Ancient Life. Astrobiology, 2003, 3, 727–738

Paul Ansell, (2017): Why STEM Not TEM, Hitachi Scientific Instruments

Ravikovitch, P.I., Neimark, A.V., (2006a): Density functional theory model of adsorption on amorphous and microporous silica materials. Langmuir 22 (2006) 11171–11179.

Ravikovitch, P.I., Neimark, A.V., (2006b): Density functional theory model of adsorption on amorphous and microporous solids. Stud. Surf. Sci. Catal. 160 (2006) 9–16.

Reimer, L. (1998): Scanning electron microscopy: physics of image formation and microanalysis. Springer, 527 p.

Ruppert, L., et al., (2014): Thermal maturity patterns in Pennsylvanian coal-bearing rocks in Alabama, Tennessee, Kentucky, Virginia, West Virginia, Ohio, Maryland, and Pennsylvania, chap. F.2 of Coal and petroleum resources in the Appalachian basin; Distribution, geologic framework, and geochemical character. USGS Professional Paper 1708, 13 p.

Ruppert, L., (2010): Geologic Controls on Thermal Maturity Patterns in Pennsylvania coal- bearing rocks in the Appalachian Basin. International Journal of Coal Geology. v. 81. pp. 169-181.

Sing, K.S.W., (2008): Overview of Physical Adsorption by Carbons, in: E.J. Bottani, J.M.D. Tascón (Eds.), Adsorption by Carbons, Elsevier, Oxford, 2008.

Sondergeld, C.H., Newsham, K.K., Comisky, J.T., Rice, M.C., and Rai, C.S., (2010): Petrophysical Considerations in Evaluating and Producing Shale Gas Resources. SPE-131768, presented at the 2010 SPE Unconventional Gas Conference, Pittsburg, Pennsylvania, USA, 23-25 February.

Staub, J., (2015): The Growth of U.S. Natural Gas: An Uncertain Outlook for U.S. and World Supply. 2015 EIA Energy Conference USGS, Assessment of Undiscovered Oil and Gas Resources of the Devonian Marcellus Shale of the Appalachian Basin Province, 2011; National Assessment of Oil and Gas

Stokes, D.J., (2008): Principles and Practice of Variable Pressure Environmental Scanning Electron Microscopy (VP-ESEM). Chichester: John Wiley & Sons.

Suzuki, E., (2002): "High-resolution scanning electron microscopy of immunogold-labelled cells by the use of thin plasma coating of osmium". Journal of Microscopy. 208 (3): 153–157.

Wang, A., Dhamelincourt P, Dubessy J, Guerard D, Landais P, Lelaurian M., (1989): Characterization of graphite alteration in an uranium deposit by micro Raman spectroscopy,

X-ray diffraction, transmission electron microscopy and scanning electron microscopy. Carbon 27(2):209-218

Yui T.F., Huang E. & Xu J., (1996): Raman spectrum of carbonaceous material: A possible metamorphic grade indicator for low-grade metamorphic rocks. Journal of Metamorphic Geology 14, 115–24.